EFFECTS OF MORPHING ON AEROELASTIC BEHAVIOR OF UNMANNED AERIAL VEHICLE WINGS

A THESIS SUBMITTED TO
THE GRADUATE SCHOOL OF NATURAL AND APPLIED SCIENCES
OF
MIDDLE EAST TECHNICAL UNIVERSITY

BY

LEVENT ÜNLÜSOY

IN PARTIAL FULFILLMENT OF THE REQUIREMENTS
FOR
THE DEGREE OF DOCTOR OF PHILOSOPHY
IN
AEROSPACE ENGINEERING

FEBRUARY 2014

Approval of the thesis:

EFFECTS OF MORPHING ON AEROELASTIC BEHAVIOR OF UNMANNED AERIAL VEHICLE WINGS

submitted by **LEVENT ÜNLÜSOY** in partial fulfillment of the requirements for the degree of **Doctor of Philosophy in Aerospace Engineering Department, Middle East Technical University** by,

Prof. Dr. Canan Özgen _______________________
Dean, Graduate School of **Natural and Applied Sciences**

Prof. Dr. Ozan Tekinalp _______________________
Head of Department, **Aerospace Engineering**

Prof. Dr. Yavuz Yaman _______________________
Supervisor, **Aerospace Engineering Dept., METU**

Examining Committee Members:

Prof. Dr. Serkan Özgen _______________________
Aerospace Engineering Dept., METU

Prof. Dr. Yavuz Yaman _______________________
Aerospace Engineering Dept., METU

Assoc. Prof. Dr. Melin Şahin _______________________
Aerospace Engineering Dept., METU

Assoc. Prof. Dr. Ender Ciğeroğlu _______________________
Mechanical Engineering Dept., METU

Assoc. Prof. Dr. Erdem Acar _______________________
Mechanical Engineering Dept., TOBB ETU

Date: 07.02.2014

I hereby declare that all the information in this document has been obtained and presented in accordance with academic rules and ethical conduct. I also declare that, as required by these rules and conduct, I have fully cited and referenced all material and results that are not original to this work.

Name, Last Name:

Signature:

ABSTRACT

EFFECTS OF MORPHING ON AEROELASTIC BEHAVIOR OF UNMANNED AERIAL VEHICLE WINGS

Ünlüsoy, Levent
Ph.D., Department of Aerospace Engineering
Supervisor : Prof. Dr. Yavuz Yaman

February 2014, 175 pages

Morphing aircraft technologies became the center of attention in aviation industry through the last decade. Although the intended optimization of the aircraft in terms of aerodynamics and/ or flight performance resulted in advantages like reduction in carbon dioxide emission and noise levels; that also brought some structural borne problems such as the possibly deteriorating change in the aeroelastic behavior of the structure. These structural problems should be clearly identified and attempted to be eliminated even at the conceptual design stages.

This study intends to provide a broad view for the effects of morphing especially on the linear aeroelastic behavior of unmanned aerial vehicle wings. The study considered four different flight phases, namely take-off, climb, cruise, and loiter. An unmanned aerial vehicle wing, which was considered to be used in these four phases, was assumed to undergo chord, span, sweep and camber change with the help of certain morphing mechanisms such as the leading and the trailing edge mechanisms and the telescopic ribs and spars. Four different wing geometries were then obtained by considering the aircraft design requirements, aircraft performance requirements and aircraft structural requirements. Those four different wing shapes so obtained, which satisfy the minimum requirements for design, performance and structure and by no means optimum for any of those requirements, were studied for linear aeroelastic instability problems. An in-house computer program was developed and used for the prediction of the flutter and divergence speeds at different stages of the flight, in which the planform of the wings were changing.

Aeroelastic models of morphing wings at different flight phases were developed as reduced order models having two-degrees-of-freedom and three-degrees-of-freedom. Theodorsen theory was used to represent the unsteady aerodynamics. Structural properties of the wings were obtained by conducting a series of finite element analyses on the developed equivalent plate models representing the planform of each morphing wing shapes. Two different classical solution methods were used during the aeroelastic analysis; k-method and pk-method. Aeroelastic analyses conducted showed that the flutter and divergence speeds drastically changes up to 58 percent and 75 percent respectively among different wing configurations, when compared to the highest flutter and divergence speeds achieved.

A series of analyses were conducted throughout this study, in order to identify the structural problems which arise due to the inclusion of the morphing phenomenon in aircraft design. It was realized that, the aeroelastic tailoring due to the morphing should be an essential part of the structural design procedure.

Keywords: Aeroelastic Analyses, Flutter Prediction, Morphing Wing Design, Reduced Order Aeroelastic Modeling

ÖZ

ŞEKİL DEĞİŞTİREBİLMENİN İNSANSIZ HAVA ARACI KANATLARININ AEROELASTİK DAVRANIŞINA ETKİLERİ

Ünlüsoy, Levent
Doktora, Havacılık ve Uzay Mühendisliği Bölümü
Tez Yöneticisi : Prof. Dr. Yavuz Yaman

Şubat 2014, 175 sayfa

Şekil değiştirebilen uçak teknolojileri geçtiğimiz on yılda havacılık sanayisinde ilgi odağı haline gelmiştir. Uçağın aerodinamik ve/ veya uçuş performansı açısından amaçlanan en iyileştirmesi, karbondioksit salınımının ve gürültü düzeylerinin azalması gibi faydalarının yanı sıra, aeroelastik davranışın olumsuz yönde etkilenmesi gibi yapısal kaynaklı sorunların da ortaya çıkmasına sebep olmaktadır. Bu yapısal problemler dikkatlice belirlenmeli ve kavramsal tasarım aşamasından başlayarak giderilmeye çalışılmalıdır.

Bu çalışmanın hedefi, başta insansız hava aracı kanatlarının doğrusal aeroelastik davranışı olmak üzere, şekil değiştirebilmenin olası etkileri hakkında kapsamlı bir bakış açısı sağlamaktır. Çalışmada kalkış, tırmanış, seyir ve avare uçuş olmak üzere dört farklı uçuş evresi incelenmiştir. Bu dört evrede kullanılması düşünülen insansız hava aracı kanadının hücum ve firar kenarı mekanizmaları, teleskopik kaburga ve kiriş mekanizmaları gibi bazı şekil değiştirme mekanizmaları yardımıyla veter, kanat açıklığı, süpürme açısı ve kambur değişimine uğradığı varsayılmıştır. Dört farklı kanat geometrisi elde edilirken; uçak tasarım

gereksinimleri, uçak performans gereksinimleri, uçak yapısı gereksinimleri göz önünde bulundurulmuştur. Gereksinimler açısından asgari değerleri sağlayan ancak bu gereksinimler açısından hiçbir şekilde en iyileştirilme süreçleri uygulanmayan bu dört kanat şekli, doğrusal aeroelastik kararlılık açısından incelenmiştir. Kanat kuşbakışı görüntüsünün değişime uğradığı, bu dört farklı uçuş evrelerindeki çırpma ve ayrılma hızları tez sürecinde geliştirilen özgün bir bilgisayar programı yardımıyla belirlenmiştir.

Şekil değiştirebilen kanatların farklı uçuş evrelerindeki aeroelastik modelleri, iki-serbestlik-dereceli ve üç-serbestlik-dereceli düşük mertebe modeller olarak geliştirilmiştir. Değişken aerodinamik yükler Theodorsen teorisi kullanılarak gösterilmiştir. Kanatların yapısal özellikleri, farklı uçuş rejimlerindeki kanatlar için geliştirilen eşdeğer plak modelleri üzerinde yapılan bir dizi sonlu elemanlar analizi ile elde edilmiştir. Aeroelastik analizlerde iki farklı klasik çözüm yöntemi olan k-yöntemi ve pk-yöntemi kullanılmıştır. Farklı uçuş rejimlerine ait yapılandırmalar için yapılan aeroelastik analizler, hesaplanan en yüksek çırpma ve ayrılma hızlarıyla kıyaslandığı takdirde çırpma ve ayrılma hızlarında sırasıyla yüzde 58 ve yüzde 75'e varan oranlarda değişimler olduğunu göstermiştir.

Bu çalışmada, şekil değiştirebilme olayından kaynaklanan yapısal sorunların belirlenmesi için analizler yapılmıştır. Çalışma sonucunda, şekil değiştirebilen kanat tasarımında aeroelastik iyileştirmenin yapısal tasarım sürecinin son derece önemli bir parçası olduğu gösterilmiştir.

Anahtar Kelimeler: Aeroelastik Analizler, Çırpmanın Öngörümü, Şekil Değiştirebilen Kanatların Tasarımı, Basitleştirilmiş Aeroelastik Modelleme

to

my parents, sister

and wife

for their love, care and support

and

to

my late grandpas

ACKNOWLEDGEMENTS

I would like to express my deepest gratitude to my supervisor and whom I believed to be my mentor, Prof. Dr. Yavuz Yaman for his patient guidance, encouragements, insight and support in this study.

I would like to thank my thesis committee members Assoc. Prof. Dr. Melin Şahin and Assoc. Prof. Dr. Ender Ciğeroğlu for their advices on the scope of this thesis, which improved the quality of this work.

I would like to show my sincere respects to the other jury members, Prof. Dr. Serkan Özgen and Assoc. Prof. Dr. Erdem Acar for their afford in order to evaluate and enhance this study.

The licensed software used in this thesis in between February 2010 and February 2012 was properties of Middle East Technical University where the author was formerly employed. The licensed software used in between February 2012 and February 2014 was properties of University of Turkish Aeronautical Association, where the author is employed on the time this study was published. The opportunity given on the usage of the software was appreciated.

I would like to thank my parents and my sister for their love, care and support.

Finally, I would like to thank my beloved wife, who always makes me felt loved and each day of my life delightful.

TABLE OF CONTENTS

LIST OF TABLES

TABLES

LIST OF FIGURES

FIGURES

LIST OF SYMBOLS

A	Aspect ratio
a	Non-dimensional distance between the mid-chord and the elastic axis of the wing
b	Half of the chord length
b	Full span
c	Non-dimensional distance from the mid-chord to the control surface hinge line
$C_{D,0}$	Zero lift drag coefficient
$C_{f,e}$	Skin friction coefficient
$C_{L,to}$	Corrected take-off lift coefficient
$C_{L,max}$	Maximum three-dimensional lift coefficient
$C_{l,max}$	Maximum sectional lift coefficient
c_r	Root chord length
c_t	Tip chord length
D	Drag force
e	Oswald span efficiency factor
E	Young's Modulus
g	Artificial damping
h	Generalized coordinate for the plunge degree-of-freedom
H	Aerodynamic moment about the hinge line
I	Second moment of area
I_α	Mass moment of inertia of the typical section model about the elastic axis
I_β	Mass moment of inertia of the control surface about the hinge line
k	Reduced frequency
K	Drag due to lift coefficient
k_h	Equivalent spring constant associated to the plunge degree-of-freedom

k_α	Equivalent spring constant associated to the pitch degree-of-freedom
k_β	Equivalent spring constant associated to the control surface rotational degree-of-freedom
L	Lifting force
M_{EA}	Aerodynamic pitching moment about the elastic axis
m	Total mass of the wing
m_β	Mass of the control surface without the actuator
n	aerodynamic load factor
p	Eigenvalue parameter
r_α	Non-dimensional radius of gyration of the typical section model about the elastic axis
r_β	Non-dimensional radius of gyration of the control surface about the hinge line
R	Turn radius
R_T	Taper ratio
S	Planform area of the wings
S_α	Static mass unbalance of the typical section model about the elastic axis
S_β	Static mass unbalance of the control surface about the hinge line
S_{ref}	Reference area
S_{wet}	Wetted surface area
T	Thrust force
U	Freestream velocity
V_{stall}	Stall speed
V_v	Vertical speed of the aircraft during climb
W	Gross weight of the aircraft
w	Transverse displacement
x_α	Non-dimensional distance between the center of mass and the elastic axis
x_β	Non-dimensional distance between the center of mass of the control surface and the hinge line
α	Generalized coordinate for the pitch degree-of-freedom

α	Angle of attack
β	Generalized coordinate for the control surface rotational degree-of-freedom
γ	Transient decay parameter
θ	Angle of climb
κ_{DL}	Induced drag
λ	Taper ratio
$\Lambda_{c/4}$	Sweep angle at the quarter chord location
Λ_{LE}	Sweep angle at the leading edge
ρ	Density of air
σ	Bending stress
ω	Harmonic frequency

LIST OF ABBREVIATIONS

bhp	Brake horse power
CAD	Computer aided design
CG	Center of gravity
CS	Control surface
DAPRA	Defense Advanced Research Projects Agency
EA	Elastic axis
FE	Finite element
FEA	Finite element analyses
FEM	Finite element method
GF	Glass fiber
GSA	Guide-slide assembly
HSP	High-strain shape-memory polymer
SDS	Selectively deformable structure
METU	Middle East Technical University
NACA	National Advisory Committee of Aeronautics
PA	Polyamide
TUBITAK	The Scientific and Technological Research Council of Turkey
UAV	Unmanned aerial vehicle
QC	Quarter chord location

CHAPTER 1

INTRODUCTION

1.1 Background to the Study

Over the last decade, aviation industry has focused on the possibilities of reduction in noise levels and carbon dioxide emissions caused by the aerial vehicles. One of the most effective ways to establish these goals was believed to be the employment of the morphing technologies on the aircraft structures. Although morphing technologies could be applied on any kind of structure, in most of the cases wings became the subject of the studies.

Morphing wings were also classified into many categories with different capabilities such as; camber change, twist change, span change and so forth. Some of the morphing technologies may completely change the wing planform between mission phases, which were referred to as fully morphing wings.

Fully morphing wings showed great prospect for reduction in carbon dioxide emission, since they may have been optimized for every phase of the mission of the aircraft. For instance, at take-off it is required to have the highest lift possible, whereas during climb the lift to drag ratio should be maximum. Both of these conditions could not be satisfied at the same time without the presence of a morphing mechanism. Each flight stage has its own criteria on the geometric configuration of the wing, therefore; fully morphing wing technologies became more sufficient.

While fully morphing wings were highly efficient in terms of aerodynamics, some structural issues resulting from morphing mechanism are to be clarified and treated accordingly. One of these problems was considered to be the possible adverse effects of morphing on the aeroelastic behavior of the wings. This thesis study was devoted to the identification of the aeroelastic characteristics of morphing wings at each stage of the flight, and detection of the structural deficiencies caused by the morphing phenomena.

1.2 Scope of the Study

The Identification of the aeroelastic behavior of the morphing wings was regarded as the main scope of this thesis. In order to conduct a series of aeroelastic analyses to detect possible negative impacts of morphing on the aeroelastic characteristics, an in-house computer program was developed by using MATLAB® programming language. There were two classical solution algorithms used for the treatment of the flutter problem, which were k-method and pk-method. By using the developed program, flutter and divergence prediction of the morphing wings were performed.

In order to fulfill the scope of the thesis, the conceptual design of morphing wings at four different flight phases was conducted. No formal optimization of the wing shapes was done. In addition to this, no formal mechanism synthesis was performed within the design. The structural models of the designed wing geometries were developed in order to examine the structural behavior of the morphing wings. The structural models were used to construct the aeroelastic models of the morphing wing at different wing geometries.

To sum up, the scope of this thesis was to develop a computer code that can predict the aeroelastic behavior of the morphing wing design and the deviation of this behavior between the stages of the flight. In order to fulfill the scope of the thesis, some aiding analyses were conducted and also a suggested morphing wing was conceptually designed without bringing any obligation on the scope of the study.

1.3 Review of Literature

The review of the literature was divided into two sections. One of the sections was devoted to the conceptual morphing designs in the literature. A short review of the progress in the selected morphing technologies was given.

1.3.1 Conceptual Morphing Designs

There are several different approaches in the development of morphing wings. The differences among these approaches are mostly due to the actuation techniques and the type of the shape change. Most of the systems are based on two main types of actuation. These are electro-mechanical actuation and smart material actuation. On the other hand, shape change mechanisms can also be categorized into four as; camber change, twist change, planform area change and sweep change.

According to those classifications, scientists study the morphing possibility of the aircraft structures. Some of the ideas involved in morphing technologies were regarded as useful. In this section the critical review of the useful literature is given in order to show the state of art related to the concept suggested within the thesis.

In METU Department of Aerospace Engineering a TUBITAK project called "Aeroservoelastic Analysis of the Effects of Camber and Twist on Tactical UAV Mission-adaptive Wings" was successfully completed, in which the design of a mission-adaptive UAV wing was handled. In this design the camber and twist of the wing is controlled by a guiding slide mechanism and a servo actuator. The control surfaces of the morphing concept are designed as open surface structures in order to eliminate high skin stresses [1][2]. The conceptual design of the mechanism was shown in Figure 1 and the placement of the morphing mechanism on the wing structure is shown in Figure 2 [3].

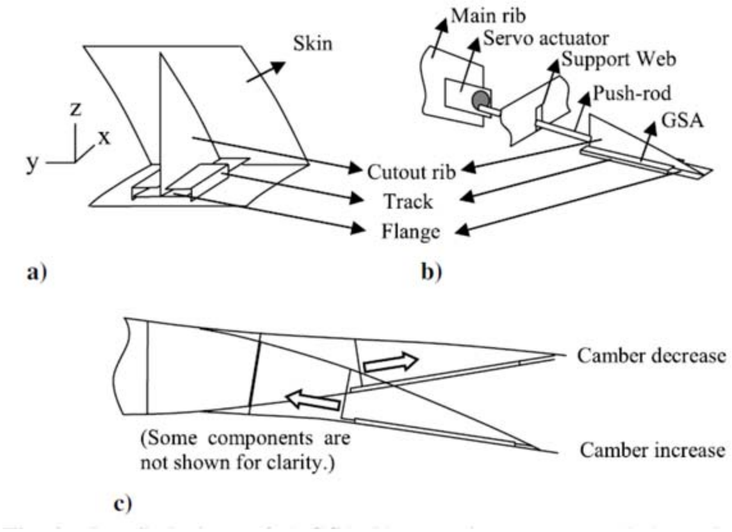

Figure 1: The Adaptive Camber Concept Developed by METU Researchers [3]

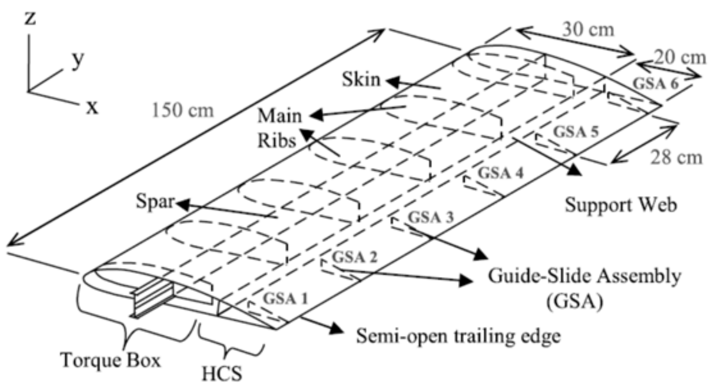

Figure 2: Placement of the Adaptive Camber Guide-Slide Assembly on the Trailing Edge of the Wing Structure

The guide slide mechanism introduced in the concept was found useful for some of the applications within this thesis study. The system used in the skin was inspired by this concept developed in METU.

One of the pioneer concepts of morphing wing technologies is considered as the telescopic rib concept developed by Gamboa P., et. al. The main mechanism of this morphing concept is based on retraction and contraction of the specially designed rib segments. By the movement of the rib segments the planform area of the wing is effectively changed. In addition to chord extension with rib retraction/contraction, this concept can also extend the spars to increase the aspect ratio and planform area. The telescopic rib mechanism is shown in Figure 3 and spar extension mechanism in Figure 4 [4].

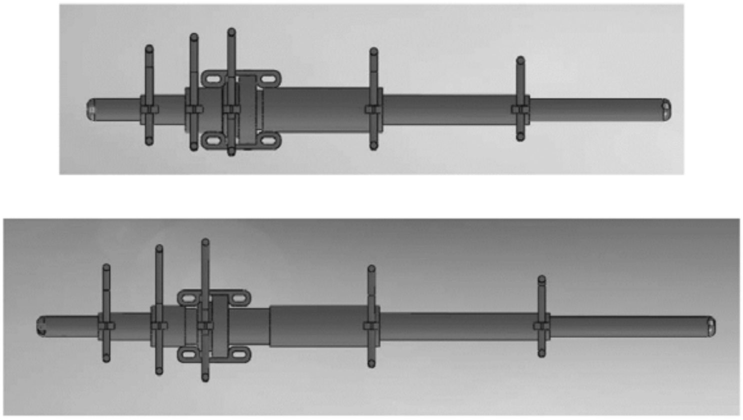

Figure 3: Telescopic Rib Mechanism [4]

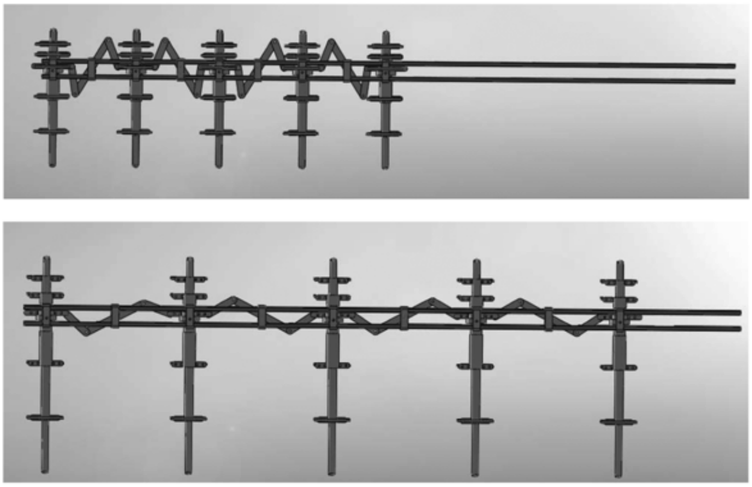

Figure 4: Spar Extension Mechanism [4]

The telescopic rib mechanism was used as a starting point for the development of the chord extension concept suggested in this thesis. Moreover, the span extension mechanism developed in this thesis was also inspired by the spar extension mechanism in [4] up to some extent.

Another effective camber change mechanism was developed by researchers of Central Aerohydrodynamic Institute of Russia. In this concept the leading and trailing edges rotate up and down due to the selectively deformable structure (SDS) used in the skin. Finite element model of the SDS structure is shown in Figure 5. These structures are actuated with hydraulic actuators and they add flexibility to the skin. The morphing leading edge design with SDS is shown in Figure 6 [5].

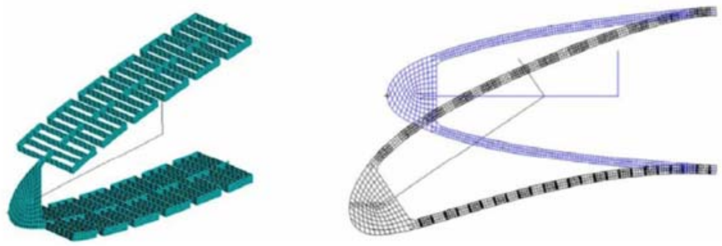

Figure 5: Finite Element Model of Selectively Deformable Structure [5]

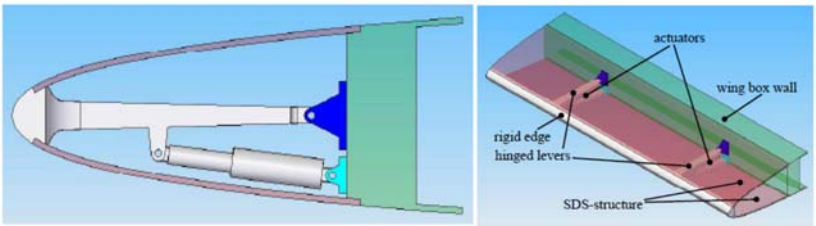

Figure 6: Morphing Leading Edge with SDS [5]

SDS structures were found inspirational for the skin concept developed within this thesis study.

In summary, the aforementioned morphing concepts were considered as inspirational designs for the concept suggested within this thesis. There were other concepts in the literature which were either not found applicable or easily producible.

CHAPTER 2

METHODOLOGY

2.1 Introduction

This chapter is devoted to the detailed explanation of the key methodology involved within this thesis work. The key methods explained in this chapter are directly related to the aeroelastic modeling and the flutter solution algorithms used within the scope of the thesis. The methods used to fulfill the scope of the thesis will not be involved within this chapter; however, those methods will be discussed under the sections devoted to those aiding analyses.

The most of the script in this chapter would be devoted to the explanation of the linear aeroelastic analyses methods involved within and the reduced order structural modeling of the wings for flutter and divergence prediction.

Most of the remaining methods were based on "Finite Element Method (FEM)". Those instances FEM was used had an aim of aiding the main scope of this thesis, which indeed was identification of the effects of shape change on the flutter characteristics of the morphing wings of unmanned aerial vehicles. Instead of focusing on the FEM, the purpose of its usage will be explained in this chapter.

2.2 Aeroelastic Modeling

Aeroelastic model used in this thesis study was based on typical section model. Typical section model is a reduced order model developed based on the idea that; a rigid wing section, taken from 75 percent of the span of the wing completely represents both the aerodynamic and the structural properties of the three dimensional wing [6] [7] [8] [9].

The advantages of using the reduced order model could be classified as follows;

- Easy to employ.
- Availability of various solution methods.
- Transformability into state-space forms.
- Compatibility with small harmonic oscillations assumption.
- Programmability.

Considering all of the advantages involved within, the reduced order model was adopted from [10] as shown in Figure 7.

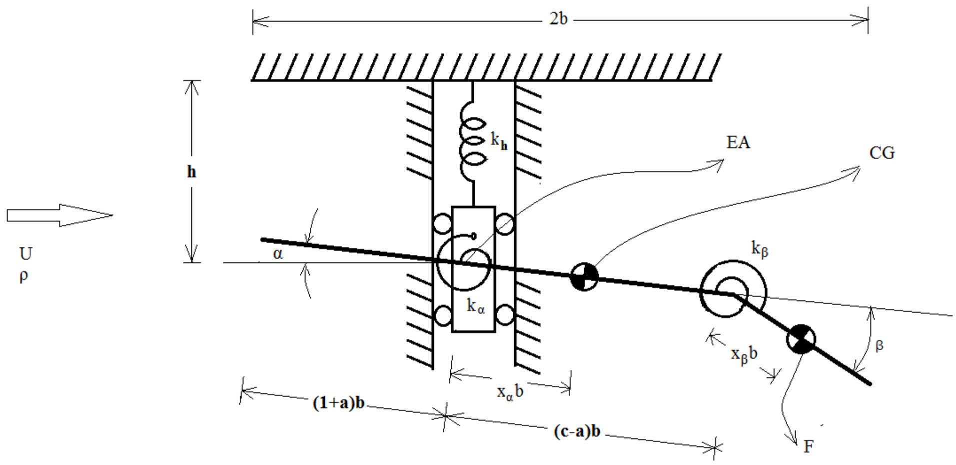

Figure 7: Three-degrees-of-freedom Typical Section Model

By direct application of the Newton's second law of motion, the governing equations of motion would be found as follows [11];

$$m\ddot{h} + S_\alpha\ddot{\alpha} + S_\beta\ddot{\beta} + k_h h = -L \tag{2.1}$$

$$S_\alpha\ddot{h} + I_\alpha\ddot{\alpha} + [I_\beta + b(c-a)S_\beta]\ddot{\beta} + k_\alpha\alpha = M_{EA} \tag{2.2}$$

$$S_\beta\ddot{h} + [I_\beta + b(c-a)S_\beta]\ddot{\alpha} + I_\beta\ddot{\beta} + k_\beta\beta = H \tag{2.3}$$

The terms in Equations 2.1-2.3 corresponds to the overall structure. These terms are defined as follows [11];

h, α and β are the generalized coordinates corresponding to plunge, pitch and control surface rotation degrees-of-freedom, respectively.

m is the total mass of the wing including all the structural and non-structural masses.

m_β is the mass of the control surface without the actuator.

k_h, k_α and k_β are the equivalent spring constants of the wing corresponding to the plunge, pitch and control surface rotation degrees-of-freedom, respectively

b is the half chord length of the typical section model

c is the distance from the mid-chord to the control surface hinge line normalized with respect to the half chord length

a is the distance between the mid-chord and the elastic axis of the wing normalized with respect to the half chord length

x_α is the distance between the center of mass and the elastic axis normalized with respect to the half chord length

x_β is the distance between the center of mass of the control surface and the hinge line normalized with respect to the half chord length

r_α is the non-dimensional radius of gyration of the typical section model about the elastic axis

r_β is the non-dimensional radius of gyration of the control surface about the hinge line

S_α is the static mass unbalance of the wing about the elastic axis

S_β is the static mass unbalance of the control surface about the hinge line

I_α is the mass moment of inertia of the wing calculated about the elastic axis

I_β is the mass moment of inertia of the control surface calculated about the hinge line

L is the aerodynamic lifting force

M_{EA} is the aerodynamic pitching moment calculated about the elastic axis

H is the aerodynamic moment due to the aerodynamic forces on the control surface calculated about the hinge line

The given three-degrees-of-freedom can be reduced into a two-degrees-of-freedom model by omitting the control surface degree-of-freedom. When reduced into two-degrees-of-freedom a pure bending-torsion coupling can be investigated in the solution. The equations of motion in the case of a two-degrees-of-freedom is given in Equations 2.4 and 2.5.

$$m\ddot{h} + S_\alpha \ddot{\alpha} + k_h h = -L \tag{2.4}$$

$$S_\alpha \ddot{h} + I_\alpha \ddot{\alpha} + k_\alpha \alpha = M_{EA} \tag{2.5}$$

The reduced order model described in this section was the bases of the flutter analyses conducted on the morphing wings. The aerodynamic terms in the system of equations are unsteady terms. The unsteady aerodynamic model, which was used to determine these aerodynamic terms, will be given in Section 5.3.

2.3 Solution of the Aeroelasticity Problem

The system of equations of the typical section model can be rewritten in the matrix form as follows [11];

$$[M]\{\ddot{q}\} + [K]\{q\} - q_\infty[Q(k)]\{q\} = \{0\} \tag{2.6}$$

Here, [M], [K] and [Q(k)] are the mass, stiffness and aerodynamic influence matrices respectively. {q} is the vector representing the generalized coordinates of the system. q_∞ is the dynamic pressure and k is the reduced frequency which is defined as [11];

$$k = \frac{\omega b}{V} \tag{2.7}$$

Where ω is the harmonic frequency, V is the freestream velocity and b is the half chord length of the typical section model.

The matrices in Equation 2.6 are defined as [11];

$$[M] = \begin{bmatrix} mb & S_\alpha & S_\beta \\ S_\alpha & \frac{I_\alpha}{b} & \frac{I_\beta + b(c-a)S_\beta}{b} \\ S_\beta & \frac{I_\beta + b(c-a)S_\beta}{b} & \frac{I_\beta}{b} \end{bmatrix} \tag{2.8}$$

$$[K] = \begin{bmatrix} k_h b & 0 & 0 \\ 0 & \frac{k_\alpha}{b} & 0 \\ 0 & 0 & \frac{k_\beta}{b} \end{bmatrix} \tag{2.9}$$

$$[Q(k)] = 2\pi b k^2 \begin{bmatrix} l_h & l_\alpha & l_\beta \\ m_h & m_\alpha & m_\beta \\ h_h & h_\alpha & h_\beta \end{bmatrix} \tag{2.10}$$

$$\{q\} = \begin{Bmatrix} \frac{h}{b} \\ \alpha \\ \beta \end{Bmatrix} \tag{2.11}$$

This system can be solved by two special methods called k- method and p-k method. These two methods will be explained extensively in two parts.

2.3.1 The k-Method

In this method, an artificial damping term was introduced into the system of equations given in Equation 2.6. This damping terms acts as structural damping in the system and when its value converges to zero, at the corresponding speed, the flutter should be predicted. When this term, g was introduced into Equation 2.6 following system of equations would be obtained.

$$[M]\{\ddot{q}\} + (1 + ig)[K]\{q\} - q_\infty[Q(k)]\{q\} = \{0\} \qquad (2.12)$$

For the solution of the system of equations given in Equation 2.12 an eigenvalue parameter was defined as given in Equation 2.13. By inserting the eigenvalue parameter into Equation 2.12, the system of equations could be expressed as given in Equation 2.14.

$$\lambda = \frac{1 + ig}{\omega^2} \qquad (2.13)$$

$$\left\{[M] + \frac{\rho}{2}\left(\frac{b}{k}\right)^2 [Q(k)] - \lambda[K]\right\}\{\bar{q}\} = \{0\} \qquad (2.14)$$

In k-method based flutter solutions, the following steps are applied [11]:

The selection of the reduced frequency values according to the mission requirements would be the first step of the solution. It would be convenient if it was noted that k-method does not permit the use of zero reduced frequency due to the singularity in the system of equations, thus a low nonzero value such as k=0.001 should be the low boundary of the analysis domain.

The second step is the evaluation of the aerodynamic influence matrix for each value of the reduced stiffness. Then the eigenvalue problem given in Equation 2.14 should be solved. The eigenvalues evaluated are the values of the complex eigenvalues defined by the Equation 2.13. From that equation the frequency and the artificial damping terms could be evaluated by using Equations 2.15 and 2.16. The corresponding flight speed could be determined by Equation 2.17.

$$\omega_i = \frac{1}{\sqrt{Re(\lambda_i)}} \tag{2.15}$$

$$g_i = \frac{\sqrt{Im(\lambda_i)}}{\sqrt{Re(\lambda_i)}} \tag{2.16}$$

$$V_i = \frac{\omega_i b}{k} \tag{2.17}$$

When the described steps were repeated for different reduced frequency values the value corresponds to g=0 gives the flutter speed of the system.

2.3.2 The pk-Method

The p-k method is also referred to as the frequency matching method in the literature. It is known as the primary tool of the flutter estimation by the aeroelasticians. In this method the system of equations are rewritten by adding an aerodynamic damping term as follows [11];

$$\left\{[M]p^2 + [K] - q_\infty[Q^R(k)] - \frac{\rho_\infty b V_\infty}{2k}[Q^I(k)]p\right\}\{\bar{q}\} = \{0\} \tag{2.18}$$

In Equation 2.18, the eigenvalue parameter, p is a special parameter which is defined in terms of the system vibration frequency and the transient decay of the aerodynamic damping as follows;

$$p = \sigma + i\omega = \omega(\gamma + i) \tag{2.19}$$

$[Q^R(k)]$ and $[Q^I(k)]$ are the real and imaginary parts of the aerodynamic influence coefficient matrix, respectively.

The state-space form of the system can be written as shown in Equation 2.20 [12];

$$\{[A] - [I]p\}\begin{Bmatrix} q \\ \cdots \\ \dot{q} \end{Bmatrix} = \{0\} \tag{2.20}$$

where

$$[A] = \begin{bmatrix} [0] & \vdots & [\mathrm{I}] \\ \cdots & & \cdots \\ -[\mathrm{M}]^{-1}\{[\mathrm{K}] - q_\infty[Q^R(k)]\} & \vdots & [\mathrm{M}]^{-1}\dfrac{\rho_\infty \mathrm{b} \mathrm{V}_\infty}{2\mathrm{k}}[Q^I(k)] \end{bmatrix} \tag{2.21}$$

This model through {q} represents both the modal amplitudes and the velocities. The eigenvalues of the matrix [A] are turned out as either real (can be different or equal) or complex conjugate pairs. If the eigenvalues are real, this state indicates a convergence of divergence as it was experienced in the cases of rigid body modes or a structural divergence mode such as control surface reversal. The rigid body modes and the divergence solutions can be found by setting the reduced frequency k to zero.

In general perspective, for most of the cases the eigenvalues are complex conjugate pairs if the reduced frequency is non-zero. These complex conjugate roots are denoted as given in Equation 2.19. In that equation, ω is the damped system frequency and γ is the transient decay parameter which is equal to 2g. The oscillatory solutions of the system require an iterative solution with the following steps [11];

The flight region in terms of the speed has to be defined. The speed region can be selected according to the stall and maximum speeds of the aircraft of interest.

A step size for velocities should be selected and for each velocity among the domain, the following steps should be followed;

The solution of the eigenvalue problem involves First the aerodynamic influence matrix, Q(k) should be evaluated. As a first estimate for the reduced frequency, one may use the converged reduced frequency values from the previous step or the ones calculated from the natural frequencies of the structure. The iteration should be done on each aeroelastic mode properly.

After evaluating the aerodynamic influence matrix, the eigenvalue problem given by Equation 2.18 should be solved. By solving the eigenvalue problem the new value of the eigenvalue parameters would be determined as real or complex conjugate pairs. These conjugate pairs carry the information about the aerodynamic damping and the frequencies of the aeroelastic modes at the specified speed.

For each step of the evaluation of the eigenvalue problem a convergence criterion should be check, i.e. an error function defined by the user as shown in Equation 2.22.

$$\left|k_{n+1}^{j} - k_{n}^{j}\right| < \text{error function defined by user} \tag{2.22}$$

If the convergence criterion is satisfied then the iterations should be terminated. If not, the steps should be repeated by using a new value of reduced frequency, until the solution converges,

ω vs. V and g vs. V plots would give a prediction for the flutter speed of the aircraft of interest. When the value of g equals to zero, the corresponding value of the speed is defined as the flutter speed.

The method described here was referred in literature as the p-k method. It is known as one of the most effective tools in aeroelastic analyses, since it can both detect the flutter and divergence phenomena at the same time.

CHAPTER 3

CONCEPTUAL DESIGN OF THE WINGS

3.1 Introduction

In this thesis, the effects of morphing on the structural (i.e. aeroelastic) behavior of the UAV wings were studied rather the detailed design of the morphing wings.

The limits of the shape changes may vary depending on the application. Therefore, no exact restrictions were present in the literature. However, one of the pioneer organizations considered during the aircraft design, DARPA, defined fully morphing aircraft wings as *"namely, a "morphing wing" is an aircraft wing able to drastically change planform shape during flight – perhaps a 200% change in aspect ratio, 50% change in wing area, and a 20 degree change in wing sweep."* [13] [14]. Within this thesis work, in order to be more precise, the limits defined by DARPA were adopted.

In terms of the shape change, the planform area, sweep and twist angles, camber, chord length and span of the wings became the major variables. Only variable that has an effect on the structural behavior of the morphing wing, which can be considered as unchanged is the total weight that the wings should carry during the mission.

In this study, the platform for the implementation of the morphing technologies was selected to be a multi-purpose civil UAV having a take-off gross weight of 30 (kg). Depending on the desired mission configuration, the dominant design terms would be the wing loading and the power to weight ratio for the fixed wing aircraft. However, for a morphing aircraft, if the weight was assumed to be constant for all missions, the wing loading constraints for conceptual design of the wing geometries would implicitly affect the required power for the flight.

The following parts of this chapter are devoted to the conceptual sizing of the wings depending on the desired portions of the mission profile.

3.2 Flight Envelope of the Unmanned Aerial Vehicle with Morphing wings

The general mission profile of the multi-purpose civil UAV involves the combination of the following;

a. Take-off in a short distance
b. Climb to operation altitude/ descent to land
c. Cruise until the desired destination is reached
d. Loiter to collect data
e. Land in a short distance

For all the instants of the occurrence of these mission segments, the UAV was assumed to be successively changing the wing shape to the corresponding geometrical configuration. The analyses and discussions involved in this thesis are based on this assumption. In addition to this, the landing and take-off configurations are considered to be similar, so that landing configuration was not studied.

3.3 Mission Efficient Geometrical Sizing of the Wings

It is a well-known fact that, each mission of an aircraft requires a different optimum wing configuration. In this thesis, since it was the most dominant term in geometrical settings, the wing loading was selected as the primary parameter for the conceptual design of the morphing wings.

Within this section and the following subsections, necessary geometrical constraints would be given for the four fight phases to be considered. In addition to those, the basic flight variables such as speed, angle of attack and altitude information would also be given.

3.3.1 Wing Loading Analysis of the Unmanned Aerial Vehicle

The wing loading of an aircraft is one of the most essential parameters affecting the overall performance. At the conceptual design phase of an aircraft, by using the desired performance constraints, the wing loading should be calculated. The wing loading formulation for each phase or mission of an aircraft was different. Although, each mission possessed a different wing loading formulation, the results of those should be double checked with the wing loading constraint derived from the stall criteria of the aircraft at each mission configuration.

Stall speed of the aircrafts depend on the planform area, airfoil shape and the density of the air. In actual physics, density is a thermal property; however, the design phase was only conceptual; thus the thermal dependence of air was omitted in this study. For this reason, throughout this thesis the temperature of the air was assumed to be steady at any specified altitude. The standard values for air properties were considered in calculations. The values for standard atmosphere were taken from the corresponding tables given in [15].

The airfoil for the whole design was chosen to be a moderate camber [16] NACA 4412 airfoil. All the data for this airfoil was experimentally tested, and the lift capability of the airfoil is considered to be high enough to allow the morphing action during the mission transitions.

It was given that with no flaps or other high lift devices deployed NACA 4412 airfoil could produce a section lift coefficient of 1.5 [17]. When the three dimensional flow effects was considered, the decrement in the wing lift coefficient could be approximated by a factor of section lift coefficient as shown in Equation 3.1 [18].

$$C_{L_{max}} \cong 0.9 \times C_{l_{max}} = 1.35 \tag{3.1}$$

The wing loading expression for the stall scenario was derived from the steady-level flight conditions, for which the acceleration should be zero and the altitude would not change [15]. Thus, total lifting force acting on the aircraft in steady, level flight conditions was equal to the weight of the aircraft. In addition to this, if the lift was assumed to be generated solely by the wings, then the wing loading for stall conditions is given by Equation 3.2.

$$\frac{W}{S} \leq \frac{1}{2}\rho_{\infty}V_{stall}^{2}C_{L_{max}} \tag{3.2}$$

The stall speed for the morphing UAV at sea level standard atmosphere was desired to be 50 [km/h]. If the desired stall speed and the density and the wing maximum lift coefficients are inserted into the Equation 3.2 the wing loading will be obtained as;

$$\frac{W}{S} \leq \frac{1}{2}\left(0.0023769\left(\frac{\text{slugs}}{ft^3}\right)\right) \times \left(45.567\left(\frac{ft}{s}\right)\right)^2 \times (1.35) \tag{3.3}$$

$$\frac{W}{S} \leq 3.33\left(\frac{lb}{ft^2}\right) \tag{3.4}$$

The stall wing loading given in Equation 3.4 is representing the minimum stall speed conditions. As it was mentioned before each flight phase for a morphing wing has different stall conditions since the planform of the wing varies. Equations 3.2 – 3.4 show a generic way for the stall calculations. The wing loading, with the stall speed consideration will be calculated for take-off, climb, cruise and loiter cases in order to complete geometrical sizing of the wing.

3.3.1.1 The Wing Loading Calculation at the Take-off Configuration

The take-off phase has been the one at which the aircraft has the lowest speed. During the take-off run the lift generated by the wings slowly increases until it balances the weight of the aircraft. Most of the fixed wing aircraft did not have wings designed for the take-off phase of the flight, since take-off has covered a very short period of the total flight time. On the contrary, morphing wings can also be designed to perform efficiently at take-off phase.

When the wing design had not been optimized for take-off condition, the take-off distances had increased as well as the fuel consumed during take-off. This is due to the fact that aircrafts had usually been optimized for cruise conditions, which resulted in small wing planform areas. For the morphing wings though, the wings could change their planform area to increase efficiency at the desired mission including the take-off.

During the design, the ground roll, which is known as the portion of the take-off that the landing gears were attached to the ground, was fixed to 250 (ft). The design constraint was defined as, the take-off parameter, according to an historical but efficient data [18]. For 250 (ft) ground roll, the corresponding value of the take-off parameter is 40 as it can be seen in Figure 8.

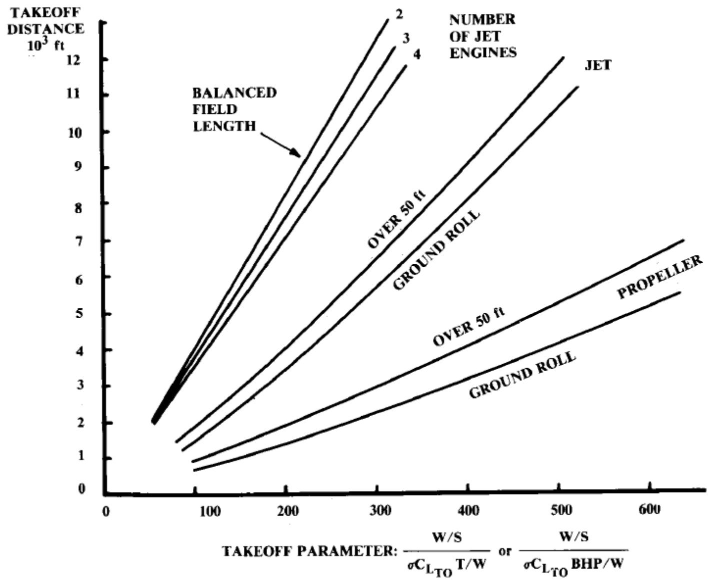

Figure 8: Take-off Distance vs. Take-off Parameter [18]

The relation between the take-off parameter and the wing loading is given by the Equation 3.5. Parameter σ in the relation is defined as the density ratio, which denotes the ratio of the air density at the take-off altitude to the sea level standard value of the air density (0.0023769 (slug/ft^3)). In addition to this, $C_{L,to,}$ is the corrected take-off lift coefficient. This correction is due to the fact that, an aircraft should take-off at a speed, the least 10% higher than the stall speed. In order to include this correction in the take-off distance calculations, the maximum lift coefficient should be divided by 1.21, because the lift coefficient is inversely proportional to the freestream velocity [15] [18].

$$Take-off\ Parameter = \frac{W/S}{\sigma C_{L_{to}}\left(bhp/W\right)} \tag{3.5}$$

The ratio given as bhp/W is a specially defined power to weight ratio. This ratio denotes the amount of weight of the aerial vehicle per unit brake horse power. For a small, homebuilt composite UAV it should have a value between 1/8 and 1/10 [18]. According to this, by taking the average of the limits defined, the power to weight ratio in terms of brake horse power was selected as 1/9. If the known parameters were substituted into Equation 3.5, the wing loading of the morphing UAV at take-off phase can be estimated as given in Equation 3.7;

$$40 = \frac{W/S}{(1)(1.1157)\left(1/9\right)} \tag{3.6}$$

$$\frac{W}{S} = 4.96\ \left[\frac{lb}{ft^2}\right] \tag{3.7}$$

If the stall condition for the take-off speed was calculated as it was previously demonstrated, the value of the wing loading was found to be lower than the value found from the ground roll relation. The lowest value from the analyses should be accounted as the wing loading setting for the take-off configuration of the morphing wings. The wing loading from stall condition is given in Equation 3.8.

$$\left.\frac{W}{S}\right)_{take-off} = \left.\frac{W}{S}\right)_{stall} = 4.01\left(\frac{lb}{ft^2}\right) \tag{3.8}$$

From 3.8 the wing planform area was found as 16.5 (ft^2) knowing that the weight of the morphing aircraft was set to 66.14 (lb). Better performance is not only dependent on the planform are of the wings but also on the shape of the planform itself. All of the aircrafts take-off at a very close speed to their stall speed. For this reason all of them are in low subsonic region. At low subsonic speeds, based on the Prandtl's lifting line theory, it can be said that the wings should have high aspect ratio (A>4) straight wings, in order to generate high lift [15].

In accordance with these, the aspect ratio of the wing was selected to be 6 with a rectangular planform for the take-off phase of the morphing wings. The geometrical properties of the take-off wing configuration are summarized in Table 1 and the planform view is given in Figure 9. All of the Computer Aided Design (CAD) features of this thesis were developed by using commercial software CATIA V5R22 [19] unless specified otherwise.

Table 1: The Geometrical Properties of the Planform of the Morphing Wings at the Take-off Configuration

Wing Loading, W/S	4.01 (lb/ft^2)
Planform Area, S	16.5 (ft^2)
Planform Shape	Rectangular
Aspect Ratio, A	6
Full Span, b	9.95 (ft)
Root Chord Length, c_r	1.66 (ft)
Tip Chord Length, c_t	1.66 (ft)

Figure 9: The Planform of the Morphing Wings at the Take-off Configuration (ft)

3.3.1.2 The Wing Loading Calculation at the Climb Configuration

It has always been desired that an aircraft should reach to the operation altitude as quick as possible. In order to accomplish this, the wings should be optimized for climb performance. In that case, the important variables, in addition to the wing loading, are the specified rate of climb, thrust to weight ratio and the drag polar.

The maximum rate of climb parameter was a design goal which was set by the designer. In this thesis, it was chosen to be 1680 (ft/min) and to maintain the best angle criteria given in [18]. Furthermore, the aircraft speed during the climb at sea level was selected as 100 (ft/s). By using these constraints, the following calculations led to the optimum value of the wing loading for the climb phase of the flight.

$$R/_C = 1680 \left(\frac{ft}{min}\right) \tag{3.9}$$

By using this value, a vertical speed given in Equation 3.10 was calculated.

$$V_V = 28 \left(\frac{ft}{s}\right) \tag{3.10}$$

The parameter G, which equals to the tangent of the angle of climb, was then found as;

$$G = \frac{V_V}{V} = \frac{28\left(\frac{ft}{s}\right)}{96\left(\frac{ft}{s}\right)} = 0.4167 \tag{3.11}$$

The thrust to weight ratio could be calculated by using the flight and engine parameters previously set;

$$T/_W = \frac{550 \times 2}{V}\left(\frac{bhp}{W}\right) = \frac{550 \times 0.8}{100\left(\frac{ft}{s}\right)} \times \frac{1}{9} = 0.4889 \tag{3.12}$$

As it was mentioned before the variables in the drag polar equation has great influence on the rate of climb calculations, which directly affect the wing loading of the aircraft. For instance, the zero lift drag, C_{D0} could be estimated by the skin friction coefficient, $C_{f,e}$ as follows [18];

$$C_{D_0} = C_{f_e}\frac{S_{wet}}{S_{ref}} \tag{3.13}$$

In Equation 3.13, the ratio of the wetted (or exposed) area, S_{wet} to the total aircraft and the wing planform area, S_{ref} was used. For the aircraft conceptually designed in this thesis, it was estimated to be 3.5. This assumed value was reached by considering that the fuselage and empennage of the aircraft is designed such that their total planform area will be half of the wing planform area. Hence the total planform area of the aircraft will be 1.5 times the wing planform area. When upper surface and lover surface and the tree-dimensional correction of 15 percent for the wing surface are and a 20 percent correction for the fuselage and empennage area are considered, a ratio of 3.5 between the wetted and planform areas will be obtained. In addition to this, the skin friction coefficient for a light single engine aircraft could be approximated as 0.0055 [18]. Therefore,

$$C_{D_0} = 0.0055 \times 3.5 = 0.02 \tag{3.14}$$

The wing loading for the climb case was derived from the rate of climb equation and given as [15];

$$\frac{W}{S} = \frac{\left[\left({}^{T}\!/_{W}\right) - G\right] \pm \sqrt{\left[\left({}^{T}\!/_{W}\right) - G\right]^2 - \frac{4C_{D_0}}{\pi A e}}}{\left({}^{2}\!/_{q\pi A e}\right)} \tag{3.15}$$

Where the discriminant should be greater than zero;

$$\left[\frac{T}{W} - G\right]^2 \geq \frac{4C_{D_0}}{\pi A e} \tag{3.16}$$

From Equation 3.16 the aspect ratio of the wings at the climb phase can be determined. The required Oswald span efficiency factor was assumed to be 0.8 [18].

$$A \geq \frac{4C_{D_0}}{\pi e \left[\frac{T}{W} - G\right]^2} \tag{3.17}$$

$$A \geq \frac{4 \times 0.02}{\pi \times 0.8 \times [0.4889 - 0.4167]^2} \tag{3.18}$$

$$A \geq 6.10 \tag{3.19}$$

If the value for the aspect ratio and the other variables were substituted into the wing loading relation given in Equation 3.15, the optimum wing loading for the preferred rate of climb settings could be found as;

$$\frac{W}{S} = \frac{[0.4889 - 0.4167] \pm \sqrt{[0.4889 - 0.4167]^2 - \frac{4 \times 0.02}{\pi \times 6.106 \times 0.8}}}{2 \Big/ \left(\frac{1}{2}\right)\left(0.0023769\left(\frac{slugs}{ft^3}\right)\right)\left(100\left(\frac{ft}{s}\right)\right)^2 \pi(6.106)(0.8)} \tag{3.20}$$

$$\frac{W}{S} = 6.58\left(\frac{lb}{ft^2}\right) \tag{3.21}$$

In order to verify the required wing loading for the stall condition given in Equation 3.2 was used. The wing loading for the stall at the climb phase was calculated to be;

$$\left.\frac{W}{S}\right)_{stall} = 16.04\left(\frac{lb}{ft^2}\right) \tag{3.22}$$

The lower value found and given in Equation 3.21 was the appropriate value for the climb condition of the morphing wings. Up to this point, the aspect ratio and the wing loading values were found. The value for the taper ratio and the sweep angle should also be determined.

The taper ratio influences the washout of the wing, which eventually is related to the total induced drag. For an elliptic wing planform, total washout is zero, which resulted in the least possible induced drag. However, both manufacturability and compatibility with morphing technologies was considered to be poor for elliptic planform geometries. Hence, tapered wings are inevitable to counterfeit the elliptical planform. The optimum taper ratio depends on the aspect ratio of the wing. Figure 10 shows a chart to predict the optimum taper ratio by using a nonlinear washout model for various aspect ratios. The optimum value of the taper ratio coincides with the minimum value of induced drag given shown as the vertical axis [20].

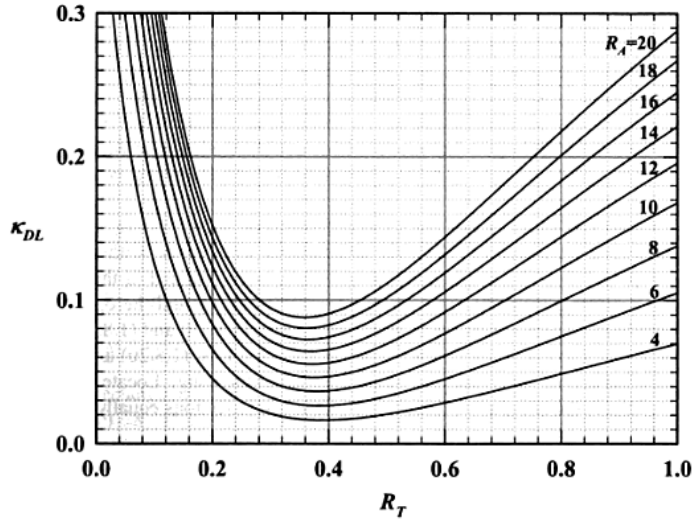

Figure 10: Chart to Predict the Optimum Taper Ratio [20]

From the chart shown in Figure 10 it can be seen that the optimum taper ratio is approximately 0.38. Therefore, the taper ratio of the morphing wing at climb phase was chosen to be 0.38.

The sweep angle of the wing at cruise condition was selected from the historical data. The chart given in Figure 11 shows an empirical curve fitted on the data collected from high climb performance aircrafts. By using that chart, for a taper ratio value of 0.38, the sweep angle at quarter chord location was chosen as 10° [21]. For this value the sweep angle at the leading edge should be 14°, in order to obey the geometry due to the taper of the wing.

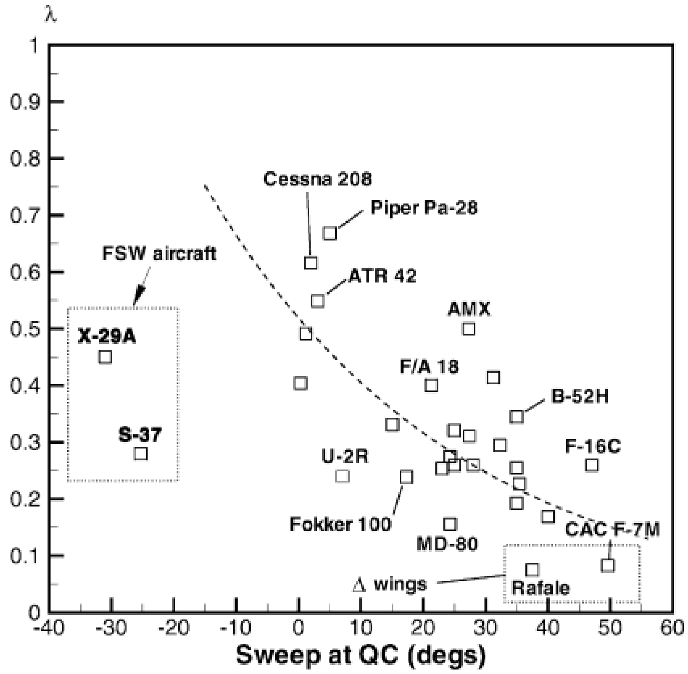

Figure 11: Chart to Approximate the Sweep Angle at Quarter Chord According to the Taper Ratio of the Wings [21]

The summary of the properties of the morphing wing planform at the climb phase of the mission envelope is given in Table 2. Moreover, basic dimensions of the determined wing planform for the climb phase are given in Figure 12.

Table 2: The Geometrical Properties of the Planform of the Morphing Wings at the Climb Configuration

Wing Loading, W/S	6.58 (lb/ft^2)
Planform Area, S	10.05 (ft^2)
Planform Shape	Swept Tetragonal
Aspect Ratio, A	6.1
Full Span, b	7.83 (ft)
Root Chord Length, c_r	1.86 (ft)
Tip Chord Length, c_t	0.71 (ft)
Sweep Angle at Quarter Chordline, $\Lambda_{c/4}$	10°
Sweep Angle at Leading Edge, Λ_{LE}	14°

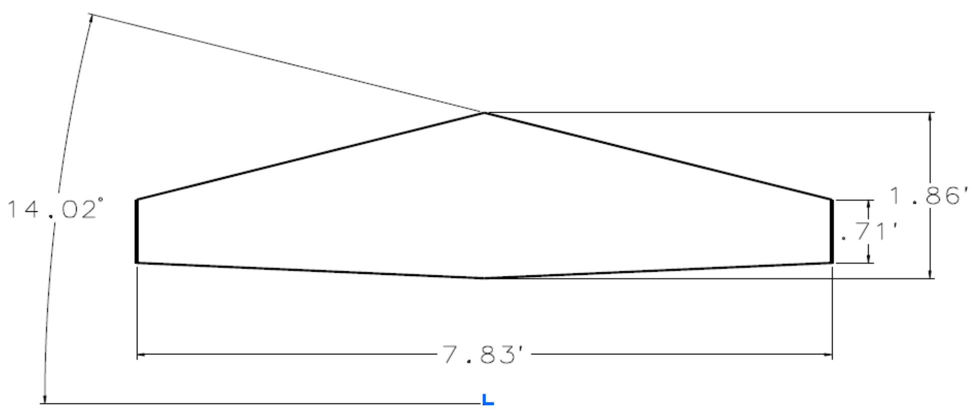

Figure 12: The Planform of the Morphing Wings at the Climb Configuration (ft)

3.3.1.3 The Wing Loading Calculation at the Cruise Configuration

The cruise altitude for the morphing aircraft was chosen to be 5000 (ft). At the cruise conditions the aircrafts are assumed to be at steady level flight. In other words, no rigid body acceleration except the gravitational acceleration was present in the motion of the aircraft. Assuming that the thrust vector has the same line of action as the velocity vector of the aircraft during cruise, it can be said that the total weight equals to total lift force. The installed power was electrical, hence; the weight of the aircraft will not change at any phase of the mission due to the consumed fuel. Knowing this, the wing loading relation for the cruise condition could be derived as follows;

$$L = qSC_L \tag{3.23}$$

$$C_D = C_{D_0} + KC_L{}^2 \tag{3.24}$$

$$\mathrm{K} = \frac{1}{\pi Ae} \tag{3.25}$$

From the basic lift equation given in Equation 3.23 and drag polar in Equation 3.24, knowing that drag due to lift, KC_L^2 and zero lift drag, C_{D0} should be equal for maximum range condition required for an optimum cruise phase [15], it could be written by using Equation 3.25 that;

$$C_L = \sqrt{\pi AeC_{D_0}} \tag{3.26}$$

At the cruise conditions, lift is equal to the total weight of the aircraft. Therefore, if Equation 3.26 was substituted into Equation 3.23, the wing loading criteria for the cruise phase of the flight could be determined as given in Equation 3.27.

$$\frac{W}{S} = q\sqrt{\pi A e C_{D_0}} \tag{3.27}$$

The speed term in the dynamic pressure, q should be defined before calculations. The maximum rate of climb is achieved when the excess power is a maximum. For a propeller driven airplane the available power from the brushless DC motor is constant with velocity which led to the fact that rate of climb will be a maximum when the required power is a minimum. And finally, the required power will be a minimum when the lift to drag ratio is a maximum [15].

Once the speed for a maximum lift to drag ratio was set, which is the rate of climb speed discussed at Section 3.3.1.2 to 100 (ft/s), the speed for the cruise can be calculated by using the relation given in 3.28 as 132 (ft/s) [15].

$$V_{cruise} = 1.32 \times V_{climb} \tag{3.28}$$

Evaluating Equation 3.27 at 5000 [ft.] cruise altitude and for the defined cruise velocity, the wing loading could be found as;

$$\frac{W}{S} = \frac{1}{2}\left(0.0020482\left(\frac{slugs}{ft^3}\right)\right)\left(132\left(\frac{ft}{s}\right)\right)^2 \sqrt{\pi(4)(0.8)(0.02)} \tag{3.29}$$

$$\frac{W}{S} = 8.00\left(\frac{lb}{ft^2}\right) \tag{3.30}$$

Once again the wing loading obtained from the stall condition for the cruise mission was compared with the result given in Equation 3.30. By evaluating Equation 3.2 the wing loading at stall condition will be found as;

$$\left.\frac{W}{S}\right)_{stall} = 24.09\left(\frac{lb}{ft^2}\right) \tag{3.31}$$

The lowest value calculated is the value for the wing loading at cruise conditions. After determining the wing loading the aspect ratio should be defined. In order to estimate the aspect ratio, a value for the maximum lift to drag ratio for the aircraft had to be assumed. The lift to drag ratio can be assumed by using historical data. It was given at the reference [18] as the average value for light weight subsonic aircraft as 14. This value was adopted for the aircraft of interest. By using the value of the maximum lift to drag ratio in the Equation 3.32, the value of drag due to lift coefficient, K could be found as shown in Equation 3.33 [15];

$$\left(\frac{L}{D}\right)_{max} = \sqrt{\frac{1}{4C_{D.0}K}} \tag{3.32}$$

$$\mathrm{K} = \frac{1}{4C_{D,0}(L/D)_{max}{}^{2}} = \frac{1}{4 \times 0.02 \times 14^{2}} = 0.0638 \tag{3.33}$$

By using the value of K obtained from Equation 3.33, the aspect ratio can be calculated as given in Equation 3.34, which in fact was derived from drag polar relation given in Equation 3.24. In Equation 3.34 the parameter e_0 is the overall Oswald span efficiency and it was assumed to be 0.7 for high wing configuration [15].

$$A = \frac{1}{\pi e_0 K} = \frac{1}{\pi \times 0.7 \times 0.0638} = 7.13 \tag{3.34}$$

The same procedure for the selection of the taper ratio and the sweep angle, which was used in Section 3.3.1.2 was repeated. The results with the other geometrical dimensions and properties are tabulated in Table 3. The planform is given in Figure 13.

Table 3: The Geometrical Properties of the Planform of the Morphing Wings at the Cruise Configuration

Wing Loading, W/S	8.00 (lb/ft^2)
Planform Area, S	8.27 (ft^2)
Planform Shape	Swept Tetragonal
Aspect Ratio, A	7.13
Full Span, b	7.68 (ft)
Root Chord Length, c_r	1.56 (ft)
Tip Chord Length, c_t	0.59 (ft)
Sweep Angle at Quarter Chordline, $\Lambda c/4$	10°
Sweep Angle at Leading Edge, Λ_{LE}	13.45°

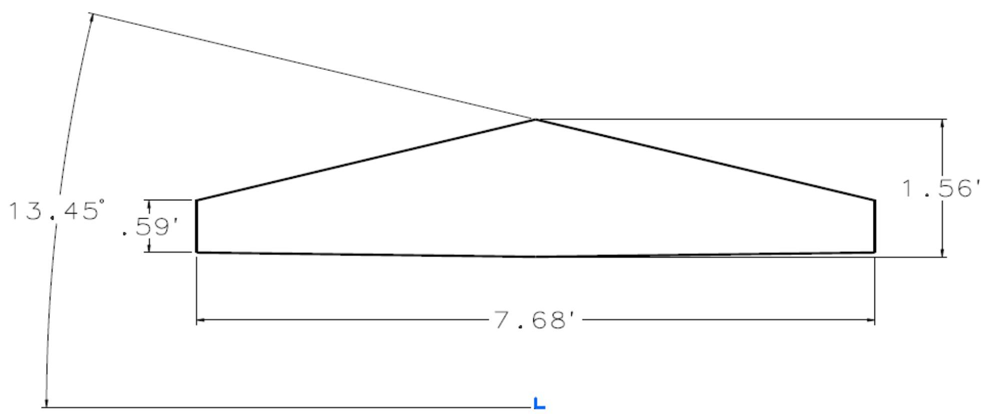

Figure 13: The Planform of the Morphing Wings at the Cruise Configuration (ft)

3.3.1.4 The Wing Loading Calculation at the Loiter Configuration

The last configuration of the morphing wings was an endurance efficient one. For a UAV, the endurance phase, in which the primary purpose is considered to be surveillance, has the wing loading relation based on the power requirements for a maximum endurance. The wing loading relation was given as shown in Equation 3.36 has a similar derivation as the one derived for the cruise. However, this time for maximum endurance, it was known that the zero lift drag was one third of the drag due to lift as given in Equation 3.35 [18].

$$C_{D_0} = K{C_L}^2 \tag{3.35}$$

$$\frac{W}{S} = q\sqrt{3\pi AeC_{D_0}} \tag{3.36}$$

The speed term in dynamic pressure, q is defined for the maximum endurance in terms of the climb speed (or speed corresponds to the maximum excess power) by the relation given in Equation 3.37. From that relation the optimum speed for loiter could be found as 76 (ft/s).

$$V_{loiter} = 0.76 \times V_{climb} \tag{3.37}$$

The conceptual design of the loiter configuration was highly dependent on the structural considerations. The aspect ratio of the wing should be as high as possible to have the best endurance performance [4]. However, for the morphing wings there were some structural limitations present. One of the constraints was the selected material's strain capacity. The second one was the need for a space for the morphing mechanisms inside the wings. Considering these limitations the aspect ratio of the wing was selected as 10.

Similarly due to the structural limitations, in order to minimize the chord length to have a high aspect ratio, the taper ratio was chosen to be 1 and no sweep will be used during loiter. If these parameters were not selected, if would not be possible to morph the structure into the selected loiter configuration. Therefore, it can be stated here that the loiter configuration chosen is not the best alternative when the performance criteria were considered.

The loiter altitude of the vehicle was chosen to be 2000 (ft). When the Equation 3.36 was evaluated for the chosen variables, the wing loading was calculated as;

$$\frac{W}{S} = \frac{1}{2}\left(0.0022409\left(\frac{slugs}{ft^3}\right)\right)\left(76\left(\frac{ft}{s}\right)\right)^2 \sqrt{3\pi(10)(0.8)(0.02)} \quad (3.38)$$

$$\frac{W}{S} = 7.95\left(\frac{lb}{ft^2}\right) \quad (3.39)$$

The wing loading according to the stall speed criteria given in Equation 3.2 at loiter condition was computed as given in Equation 3.40. Since, the first value of wing loading given in Equation 3.39 was lower, it was used for the geometrical identification of the morphing wing at loiter.

$$\left.\frac{W}{S}\right)_{stall} = 8.74\left(\frac{lb}{ft^2}\right) \quad (3.40)$$

The summary of the dominant geometrical properties of the morphing wings at loiter settings is tabulated in Table 4, and the planform of the wing with the necessary dimensions is shown in Figure 14.

Table 4: The Geometrical Properties of the Morphing Wings at the Loiter Configuration

Wing Loading, W/S	7,95 (lb/ft^2)
Planform Area, S	8.32 (ft^2)
Planform Shape	Rectangular
Aspect Ratio, A	10
Full Span, b	9.12 (ft)
Root Chord Length, cr	0.91 (ft)
Tip Chord Length, ct	0.91 (ft)

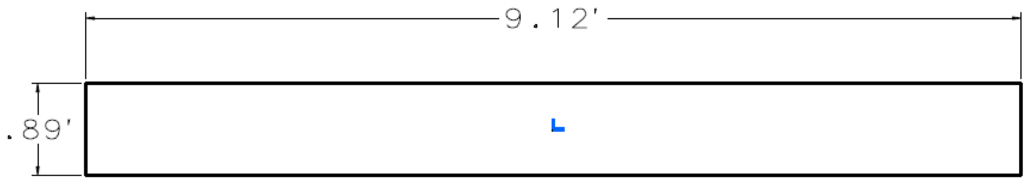

Figure 14: The Planform of the Morphing Wings at the Loiter Configuration (ft)

3.3.2 Angle of Attack Analyses of the Unmanned Aerial Vehicle

In order to complete the mission for the chosen or calculated performance input, the aircraft has to fly at a specific angle of attack. The pressure distribution for each angle of attack is different, for this reason it was essential to compute the corresponding angles of attack at take-off, climb, cruise and endurance in order to obtain the precise pressure distribution which will be used in structural analyses.

The properties of the NACA 4412 were taken from the NACA report No. 563. The experimental values of the pressure distribution for different angles of attack were given in that report [17].

The angle of attack values were calculated assuming steady level flight for climb and cruise phases and level turn maneuver for the loiter phase.

3.3.2.1 The Angle of Attack Calculation at the Take-off Configuration

Take-off phase of the aircraft requires the highest possible lift coefficient. The highest angle of attack referred to the highest stall angle of attack of the airfoil profile. The stall occurs at 16° as it can be seen in Figure 15 showing the variation of the section lift coefficient with respect to the effective angle of attack [17].

$$\alpha_{take-off} = \alpha_{C_{L,MAX}} = 16^{\circ} \tag{3.41}$$

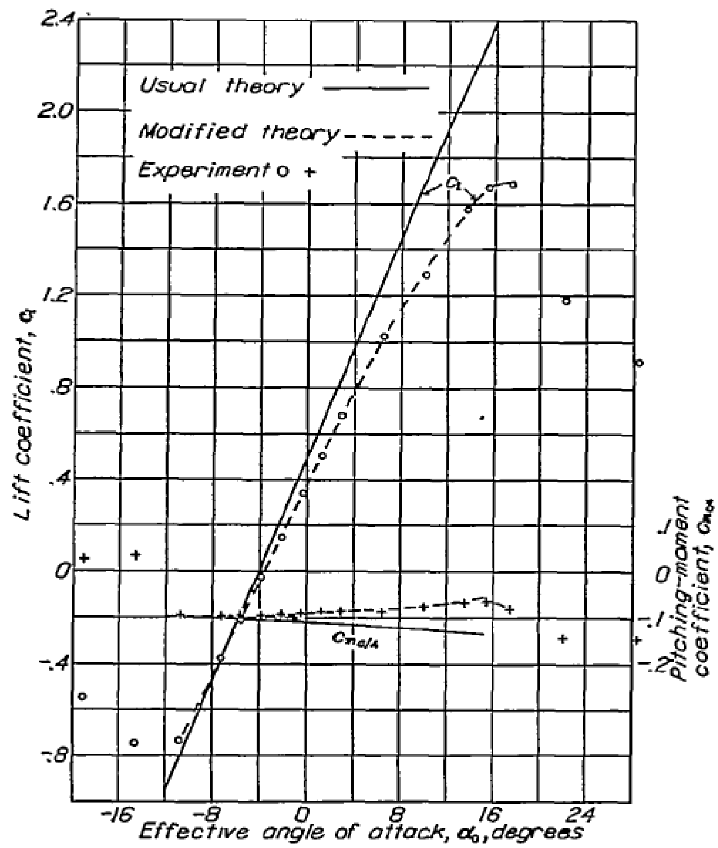

Figure 15: The Lift Curve of NACA 4412 Airfoil Profile [17]

3.3.2.2 The Angle of attack Calculation at the Climb Configuration

The ratio between vertical speed and the horizontal speed for the maximum rate of climb condition was identified previously in Section 3.3.1.2 as;

$$G = \frac{V_V}{V} = 0.4167 \tag{3.42}$$

This means that the climb angle could be determined as;

$$\theta = tan^{-1}(G) = tan^{-1}(0.4167) = 22.62° \tag{3.43}$$

Assuming steady level flight along the path defined by the climb angle the four forces of flight can be collected together at the center of gravity location of the aircraft by using the principle of transmissibility as shown in the Figure 16.

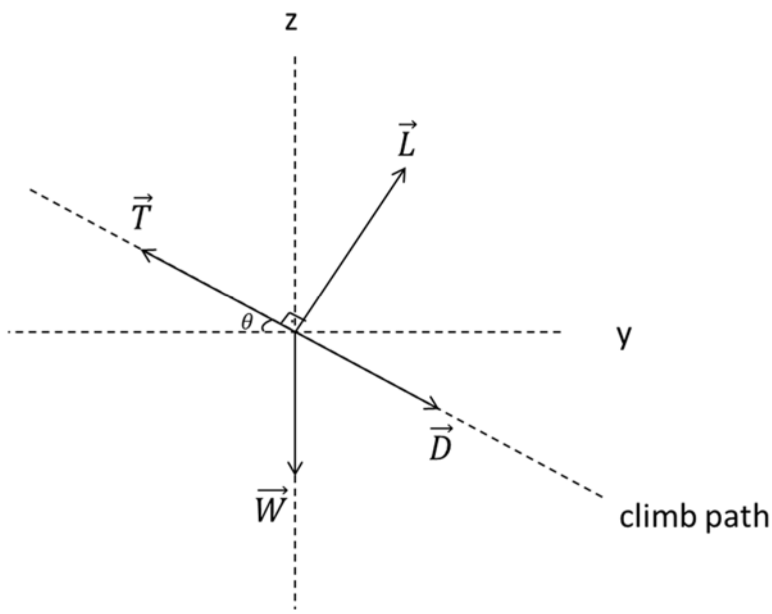

Figure 16: Four Forces of Flight at Steady Level Climb along the Climb Path

If the Newton's 1st Law of Motion was applied on the free body diagram shown in Figure 16 it could be written that;

$(+\uparrow)\sum F_Z = 0$: (3.44)

$$Lcos\theta + Tsin\theta = W + Dsin\theta \quad (3.45)$$

Thrust to weight ratio was previously found as 0.4889, which would eventually led to;

$$L(cos22.62°) + 0.4889W(sin22.62°) = W + D(sin22.62°) \quad (3.46)$$

$$0.923L - 0.385D = 0.812 \quad (3.47)$$

Knowing that the weight of the aircraft was chosen as a design constraint and set to the value of;

$$W = 66.14\ lb \quad (3.48)$$

Substituting the weight into relation 3.42 the first equation of motion would be determined as;

$$0.323L - 0.385D = 53.7lb \quad (3.49)$$

From free body diagram it can be written in the longitudinal axis of the flight;

$\left(\overset{+}{\rightarrow}\right)\sum F_y = 0$: (3.50)

$$Tcos\theta = Lsin\theta + Dcos\theta \quad (3.51)$$

Substituting the known values into Equation 3.51 and evaluating would lead to;

$$(0.4889W)(cos22.62°) = L(sin22.62°) + D(cos22.62°) \tag{3.52}$$

$$0.4513W = 0.385L + 0.923D \tag{3.53}$$

$$0.385L + 0.923D = 29.85\ lb \tag{3.54}$$

Equation 3.54 is the second equation of motion for steady level climb. Simultaneous solution of 3.45 and 3.49 yielded;

$$L = \frac{(0.923)\big(53.7(lb)\big) + (0.385)\big(29.851(lb)\big)}{(0.323)^2 + (0.385)^2} \tag{3.55}$$

$$L = 61.06\ (lb) \tag{3.56}$$

By using the well-known lift relation given in Equation 3.57, the lift coefficient of the climb phase could be determined as;

$$\mathrm{L} = \frac{1}{2}\rho_\infty {V_\infty}^2 S C_L \tag{3.57}$$

$$C_L = \frac{2 \times 61.06\ (lb)}{\left(0.0023769\left(\frac{slugs}{ft^3}\right)\right)\left(100\left(\frac{ft}{s}\right)\right)^2\left(10.05(ft^2)\right)} = 0.511 \tag{3.58}$$

From the chart shown in Figure 15, the corresponding angle of attack at climb phase can be found as follows;

$$\alpha_{Climb} \cong 2° \tag{3.59}$$

3.3.2.3 The Angle of Attack Calculation at the Cruise Configuration

For steady level flight at 5000 (ft), the angle of attack was simply calculated by assuming that thrust vector has the same line of action with the flight path, which would eventually led to the equality of lift force and the weight.

$$L = W \tag{3.60}$$

$$C_L = \frac{2W}{\rho_\infty {V_\infty}^2 S} = \frac{2 \times 66.139\ lb}{\left(0.0020482\ {}^{slug}/_{ft^3}\right)\left(132\ {}^{ft}/_{s}\right)^2 (7.12ft^2)} \tag{3.61}$$

$$C_L = 0.52 \tag{3.62}$$

$$\alpha_{Cruise} \approx 2° \tag{3.63}$$

3.3.2.4 The Angle of Attack Calculation at the Loiter Configuration

Loitering mission was previously defined to occur at 2000 (ft) and at that altitude it was assumed that the aircraft completes circular paths having radius of 1000 (ft). The acceleration relation for the level turn was given as shown in Equation 3.64 [15].

$$R = \frac{{V_\infty}^2}{g\sqrt{n^2 - 1}} \tag{3.64}$$

From Equation 3.64 the expression of the load factor can be isolated as;

$$n = \sqrt{\left(\frac{V_\infty{}^2}{Rg}\right)^2 + 1} \tag{3.65}$$

Evaluating 3.65 led to a load factor of 1.016 as follows;

$$n = \sqrt{\left[\frac{\left(76 \, {}^{ft}/_{s}\right)^2}{1000ft \times 32.2 \, {}^{ft}/_{s^2}}\right]^2 + 1} \tag{3.66}$$

$$n = 1.016 = \frac{L}{W} \tag{3.67}$$

From Equation 3.67 the value of the lift coefficient for the loitering could be evaluated to find the corresponding angle of attack.

$$C_L = \frac{2nW}{\rho_\infty V_\infty{}^2 S} = \frac{2 \times 1.016 \times 66.139(lb)}{\left(0.0024092\left(\frac{slugs}{ft^3}\right)\right)\left(76\left(\frac{ft}{s}\right)\right)^2 \left(7.85(ft^2)\right)} \tag{3.68}$$

$$C_L = 1.23 \tag{3.69}$$

$$\alpha = 12° \tag{3.70}$$

The summary of the results of the angles of attack for the four selected flight phases; take-off, climb, cruise and loiter are tabulated in Table 5.

Table 5: The Calculated Angle of Attack Values of the Particular Mission Phases

Take-Off	16°
Climb	2°
Cruise	2°
Loiter	12°

CHAPTER 4

STRUCTURAL DESIGN AND MATERIAL SELECTION OF THE MORPHING WINGS

4.1 Introduction

In this chapter; the identification and sizing of the main structural members is discussed, and the appropriate selection of the materials is presented.

The identification and sizing of the main structural elements involves the decision of the number of the spars and the ribs. The geometrical positioning of the ribs and the spars, in order to achieve the four different wing configurations, which were conceptually designed in Chapter 3, was also decided in this chapter.

The selection of the materials depends on the morphing mechanism. The properties of the material such as elongation at break, yield strain and total strain energy have great influence on the selection of materials. In addition to that, the manufacturability of the system was considered at the materials selection phase.

There were two essential issues through the structural design of the morphing wings. The first one is the internal structure that changes orientation with respect to the structural form of the other phase among the four mission phases. A conceptual solution to this issue has been presented. The second issue was the deflection requirement of the skin material. Due to the shape change large deformations are present on the skin structure. An appropriate choice of the material was required for the resolution of this issue.

In this chapter, the conceptual structural design of the morphing wings will be presented; in addition to that, the assigned materials and suggested production techniques will be described.

4.2 Material Selection and Proposed Manufacturing Technique

In general, the morphing wing structures are heavier than the conventional wing structures, due to the shape changing mechanisms and their actuators installed. If they are not designed carefully, their expected advantage of better performance may turn into a disadvantage since the amount of power required to carry a heavier object is more than a lighter object. This also requires that the overall weight of the morphing wing has to be as light as possible.

In addition to the expected lightness of the structure, there is a more serious issue, which is involved in the selection of the skin material. The skin material requires having the capability of large elastic deformations. Recent metals or fiber reinforced composite materials are not appropriate to be compliant skin structures, since their elastic strain capacities are very low. Therefore, in this study the materials used in the skin structure were selected from the polymers available in the literature.

The manufacturability is another issue in the material selection. For the production of the designed morphing wing, the rapid prototyping method based on selective laser sintering (SLS) with polymeric powder material, was selected as the manufacturing technique to be followed. As a result, the materials were selected from the available ones for the SLS. The materials available were some variants of polyamides. Polyamides are one of the earliest engineering polymers, which were used to replace the metals [22].

The selection of suitable material for the internal structure and the skin was different. High strain was only desired in the skin material. The internal structure was believed to sustain the aerodynamic loads and therefore, had to be stronger. Hence, the material for the internal structure was selected as PA-3200GF, which is a variant of polyamide reinforced with chopped glass fibers. This material is synthesized based on Nylon 12. The material properties of PA-3200GF are given in Table 6. It would be better to note here that the direction denoted by Z, in the material properties refers to the direction perpendicular to the produced layers. For this reason, the modulus and strength in that direction are low compared to the other directions. This holds for the other materials, which were selected from the range of materials available in SLS.

Table 6: Material Properties of PA-3200GF [23]

Tensile Modulus, X Direction	3200 (MPa)
Tensile Modulus, Y Direction	3200 (MPa)
Tensile Modulus, Z Direction	2500 (MPa)
Tensile Strength, X Direction	51 (MPa)
Tensile Strength, Y Direction	51 (MPa)
Tensile Strength, Z Direction	47 (MPa)
Flexural Strength, X Direction	73 (MPa)
Poison’s Ratio, All directions	0.3
Strain at Break, X Direction	9 %
Strain at Break, Y Direction	9 %
Strain at Break, Z Direction	5.5 %
Density	1220 (kg/m^3)

For the skin, the selected material was a high strain capacity variant of engineering polyamide, PA-1101. This material is synthesized based on Nylon 11. The material properties of PA-1101 are given in Table 7.

Table 7: Material Properties of PA-1101 [24]

Tensile Modulus, X Direction	1600 (MPa)
Tensile Modulus, Y Direction	1600 (MPa)
Tensile Modulus, Z Direction	1600 (MPa)
Tensile Strength, X Direction	48 (MPa)
Tensile Strength, Y Direction	48 (MPa)
Tensile Strength, Z Direction	48 (MPa)
Poison's Ratio, All directions	0.3
Strain at Break, X Direction	45 %
Strain at Break, Y Direction	45 %
Strain at Break, Z Direction	30 %
Density	1220 (kg/m^3)

The selected materials are not as strong as the engineering metals and fiber reinforced composites, however; compared to those, they have superiority in the sense that, they can be manufactured in every shape continuously without any unnecessary joints and connections. By this way, the weight of some of the connectors and fasteners were also eliminated from the overall weight of the.

4.3 The Morphing Skin Structure

The skin shell structure was considered to be the most challenging member of the morphing design. Even though, the material selected has high strain capability, the elongation of the skin structure alone was not enough. The selected material had an elongation at break value of 45 percent as it was given in Table 7. However, the necessary elongation was considered to be higher than that value. Moreover, using a material with higher strain capacity was not enough to support the aerodynamic form of the wing, since they have very low Young's moduli which may lead to an outward curvature due to the suction of the low static pressure air flowing around the wing. Hence, the issue was a compromise between strength and flexibility. The material was considered to sustain the necessary flexibility for the span change in the structure, and would also make it possible to change the sweep of the wing.

The total strain on the skin was considered to be a very large value. For instance, maximum chord length at the tip of the wings was calculated as 1.66 (ft) occurring at take-off phase, whereas the minimum chord length was calculated as 0.59 (ft) during cruise configuration of the morphing wings was achieved. The relative elongation of the wing chord was around 181.3 percent. There are some polymers in the literature which can even exceed the computed percent elongation value; however, their transverse load carrying capacity is near null. Which indeed means that they cannot withstand the aerodynamic loads.

A successive solution for this was considered as a hybrid structure formed by the combination of PA-1101 and a high-strain shape-memory polymer (HSP) analyzed by Voit et. al. [25]. The important material property of the analyzed polymer was its elongation before yield. At a glass transition temperature of 28° C the fully recoverable elongation limit was measured as 807 percent during the conducted experiments. The disadvantage of using the hyperplastic polymers is their high glass transition temperatures. In order to avoid this in the air the skin should be kept over 28° C through entire flight.

Hence, the skin shell structure was developed with multiple layers of PA-1101 which can slide on top of each other, and at the connections of these layers as the joining material, HSP-28 was used. The stretched position of the HSP is the most contracted position of the skin, which was the cruise phase. By this way, the extraction of the wing was conducted easier and faster with the help of pre-strained HSP. The working principle of the proposed skin structure is given in Figure 17.

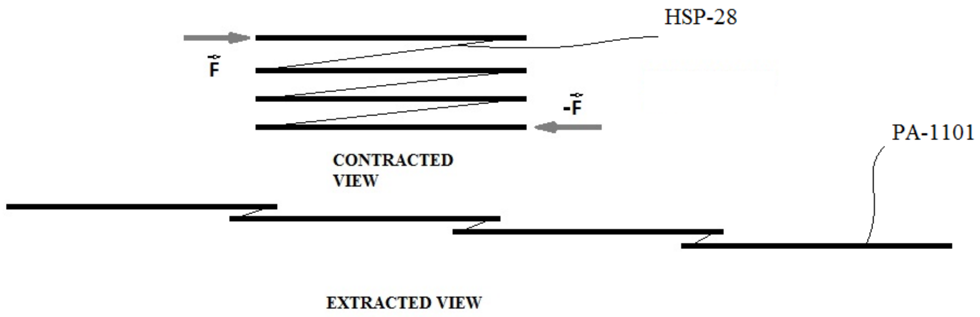

Figure 17: Folding Skin Concept used in Chord Extension

All of the portions of the skin were not designed with this concept. For instance, leading edge of a wing is the location for an airfoil to generate the largest gradient in the pressure distribution. Also, the trailing edge should be manufactured as thin as possible; therefore, the folding skin structure should not be used near the trailing edge. The smallest chord length case, which was the tip chord of the cruise configuration, was chosen to be the base. The first 20 percent of the chord length and the last 10 percent of the chord length kept unfolded through the morphing processes, which were measured as 0.118 (ft) and 0.059 (ft) respectively. The remaining 70 percent was 0.413 (ft) long, which should extract 1.27 (ft) in order to reach 1.483 (ft) in length, which was the remaining chord length of the tip chord of the take-off configuration. The expandable portion of the wing is shown in Figure 18.

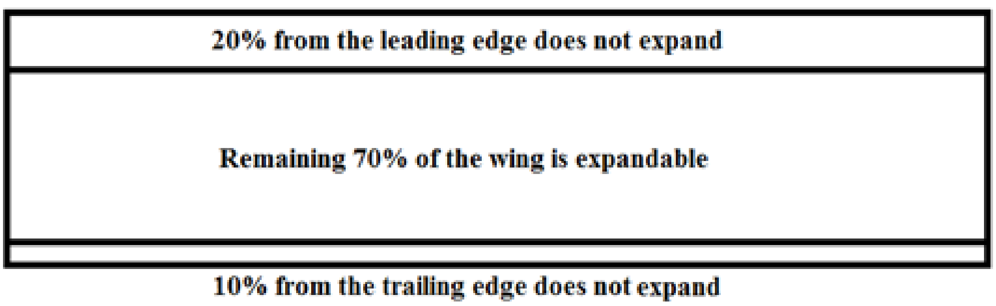

Figure 18: A Generic Representation of the Expandable Portion of the Skin

With the overlapping skin portions considered, which was preferred to be at least 20 percent of the portion length, five layers of skin portions were needed in order to achieve the desired morphing amount.

The unfolded portions of the skin structure should be 0.04 (inches) thick, and the folded skin portions should be 0.02 (inches) thick each. The width of the HSP shells, used to connect the skin portions at unscratched position should be 1 (inch) at each connection and the thickness should be 0.04 (inches). The HSP material was not considered to be structural members, since the material is extremely elastic and carries insignificant amount of load compared to the original skin material PA-1101. The skin segments were also covered with HSP from the outside with a 0.02 (inches) thick membrane to develop a closed section in terms of aerodynamics, in order to avoid the leakage of air from inside of the wing.

The shape of the skin was held together by the stiffeners attached to each portion, which eventually were connected to the morphing mechanisms located on the rib segments. These mechanisms on the rib segments were not only designed to sustain the integrity of the skin but also to keep the NACA 4412 profile at each discrete shape change.

To sum up, it was made possible to have a working morphing mechanism with a hybrid skin structure. The structure was formed by a combination of strong and durable and elastic polymer, PA-1101 [24] and an extremely high-strain thermoplastic HSP-28 [25]. The integrity and the shape of the hybrid skin structure should only be sustained by special morphing mechanisms.

4.4 Internal Structure

4.4.1 Overview of the Internal Structure

The internal structure of the wing was designed to consist of the spars, the stiffeners, the ribs and the shape changing mechanism. No kinematic synthesis about the shape changing mechanism was attempted in this thesis. It was believed that, the common structural properties for all of the flight configurations were the number of spars, stiffeners and ribs. After the number of the structural members were chosen; it could be assumed that the morphing mechanism is capable of changing the shape of the internal structure and keeping the integrity of structure unchanged under each and every circumstance.

The geometrical sizing of the internal structure had to be conducted by considering the maximum elongation at the skin shell structure. The motion of the internal structure had to maintain the uniform stress and strain distribution on the skin at in-vacuo conditions. The aerodynamic loading was excluded from this criterion, since the pressure distribution on a wing is not constant. The way to achieve a uniform stress distribution was explained in Section 4.3.

Internal structure of the wings was regarded as the primary load carrying parts. There should be especially no compression or any other type of stress applied on the internal structure at in-vacuo condition for the most contracted shape. Similarly, the most extracted position of the internal structure should not result in especially tensile or any other type of stress. The continuous shape change among the most extracted and contracted positions of the structure should be sustained by a rigid body motion.

Morphing concept should also be developed considering the weight constraints. The number of the actuators was found to be influential on this problem. The morphing mechanism as a part of the internal structure should provide the desired motion with a minimum possible number of actuators in order to reduce the weight.

4.4.2 Spars

4.4.2.1 General Overview of the Spars

Internal structure should contain at least one spar, regarded as the main spar. However, single spar structures are weak in terms of flutter characteristics, since the torsional stiffness decreases in the absence of the rear spar [26]. Reduction in the torsional stiffness might lead to a classical bending-torsion coupling, because of the decrement in the ratio of plunge and pitch stiffness. In addition to the aeroelastic considerations, the stability of the morphing can be maintained if a second spar is present, since the proposed folding skin design needed at least two chordwise supports to glide on. For these reasons, a two-spar structure was cogitated to be used in the internal structure of the wing.

The spars were designed as the least morphable elements of the internal structure. To provide this, the spars were indigenously designed and developed. The sole motion that the main spar undergo was supposed to be the sweep change, which could be sustained by a pure rotation around transverse axis about the root locations. The rotational motion could be actuated by a step motor located at the root section of the wing. In addition to the described rotational motion the rear spar could translate relative to the main spar. The motion of the system could be regarded as a paddling motion as shown in Figure 19.

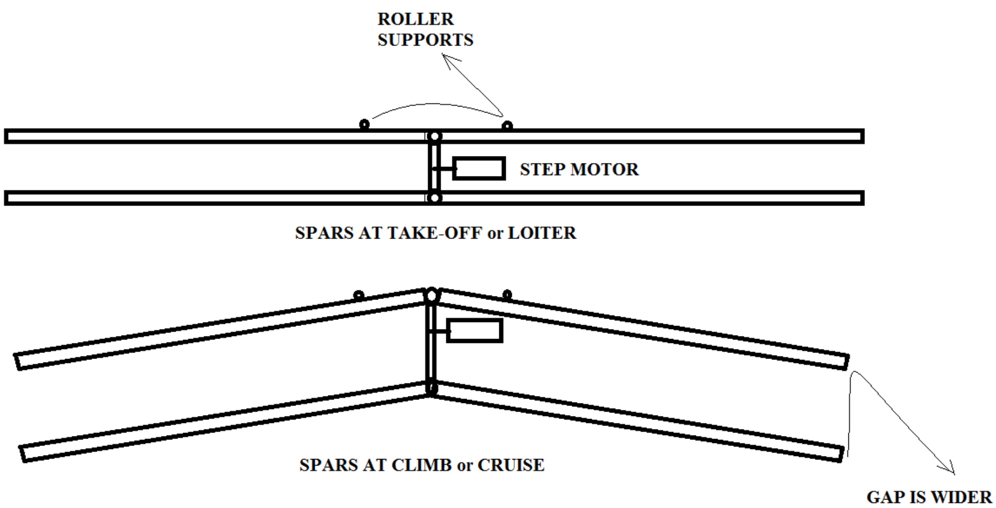

Figure 19: The Suggested Orientation Change of the Spars

It should be noted that the rear spar could also rotate relative to the main spar, provided that the taper ratio of the morphing wings calculated for the climb and cruise conditions was successively employed.

The length of the spars was designated to be the same as each other and fixed to a certain value. Due to the leakage of the air from bottom surface of the wings (high pressure side) to upper surface of the wings (low pressure side) the lift at the tips of the wings are lower than the sections which are closer to the root. For this reason the total amount of the load acting on the tip sections of the wings could be carried by the rods of the tip extension mechanism, which were designed as a component of the rib cluster.

The total spar web height was a variable among the mission configurations, since the thickness of an airfoil is a function of the chord length and the web height of the spar depends on the thickness of the airfoil. Since it would inevitably increase the weight as well as the complexity of the structure, it was not considered to include a height change capability of the spars webs.

The web height was also a function of spanwise direction. It is larger near root, since, the minimum chord length at the root section was 0.91 (ft) (at loiter), whereas, the minimum chord length at tip section was 0.59 (ft) (at cruise). While the web height decreases from root to tip section, the spar cap thickness would be adjusted to have the same second moment of area at all cross-sections of the spars. This was made in order to maintain the same strength in order to maintain a uniform support for the ribs.

The cross-section of the spars was chosen as regular I-Sections.

For a two spar wing, the location of the front spar should be between 12 and 17 percent of the chord length and the location of the rear spar should be between 55 and 60 percent of the chord length [26]. In order to be precise the locations were chosen to be the same as those suggested, the location of the main spar was chosen to be 15 % and the location of the rear spar was chosen as 60 % in this study.

The rear spar should have the flexural rigidity, which should be 50 percent of the flexural rigidity of the main spar. The reason for this was that the aerodynamic pressure distribution generates a larger pressure gradient at the leading edge and about two third of the lift is generated at the first half of the chord. For a basic Euler-Bernoulli Beam assumption, the flexural rigidity has been defined as EI. Since the material used in both spars was the same the second moment of area of the main spar should double the rear spar. After the spar web heights were decided, by using this criteria, the spar cap size for each spar was determined.

4.4.2.2 Geometrical Sizing the Spars

As it was mentioned in Section 4.4.2.1 the main spar was located at 15 percent of the chord. The thickness of the airfoil at the 15 percent of the chord is 10.6 percent of the chord length. Similarly, the rear spar was located at the 60 percent of the chord and at that location the thickness of the airfoil is 9.1 percent of the chord length. These percentages were considered to be the limiting values for the spar web heights.

At the root section minimum possible chord length was achieved at loitering phase as 0.91 (ft.). Therefore, by using the percentages described at the previous paragraph, the height of the main spar web at root section was chosen to be 1.1 (inches) with manufacturing tolerance and spar cap clearance of 5 percent. Similarly, at the root section of the rear spar, the web height was chosen as 0.95 (inches).

At the tip section the minimum chord length was calculated as 0.59 (ft.). If the same procedure used for the main spar was repeated for the rear spar; for the given value of the chord length the web heights of the main and rear spar were calculated as 0.7 (inches) and 0.6 (inches) respectively.

For a general aviation aircraft wing, 80 % to 90 % of the transverse load is carried by the spars. The initial sizing of the spars could be conducted by a simple theory, such as the classical beam theory, if there is no acceleration in the system the governing equation for the displacement field should be given as shown in Equation 4.1.

$$\frac{d^4w(x)}{dx^4} - \frac{q(x)}{EI} = 0 \tag{4.1}$$

In equation 4.1, transverse displacement, spanwise lift distribution, and flexural rigidity were defined by the parameters w(x), q(x) and EI respectively. It would be convenient to add that, the weight of the wing was neglected in these calculations. For the solution of the equation 4.1 the model given in Figure 20 was used.

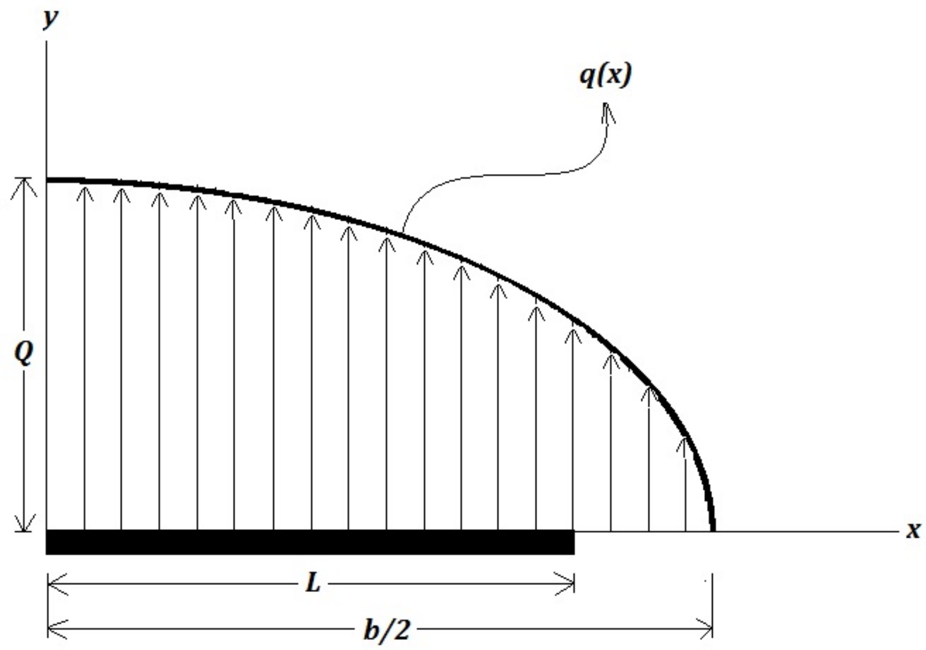

Figure 20: Classical Beam Model Used for the Sizing of the Spars

As it could be understood from the Figure 20, the spanwise lift distribution was assumed to be elliptical. As it was described in Section 4.4.2.1, the length of the spars was limited to the shortest wing span configuration. When extracted, the extension rods, on which the rib clusters were attached, carry the transverse loading on the extracted portion of the span, and transmit that loading to the spars at the spar tips. Therefore, the portion of the loading after the spar length L was implemented on the model as boundary conditions at x=L. The lift distribution was assumed to be steady and the case studied during the spar sizing was the ultimate load factor case. The ultimate load factor is defined as follows;

$$n_{ultimate} = 1.5 \times n_{maximum} \tag{4.2}$$

The maximum load factor was a design constraint and it was chosen to be 3g. Maximum load factor was selected according to the purpose of the UAV. Since the UAV in this thesis was a civil purpose UAV, it was not necessary to have a large load factor.

For the sizing of the spars an ultimate load of 4.5g was considered by using Equation 4.2. The major radius of the ellipse was half span, b/2, whereas the minor radius, Q, was found by equating the area under the curve for 4.5g ultimate loading case to 4.5 times the weight of the vehicle, as given in Equation 4.3.

$$Q = \frac{36W}{\pi b} \tag{4.3}$$

If the parameters were substituted into the general equation of an ellipse, the lift distribution for the ultimate case was determined as given in Equation 4.4.

$$\mathrm{q}(x) = \frac{b}{2}\sqrt{1 - \left(\frac{\pi b x}{36W}\right)^2} = \frac{b}{2}\sqrt{1 - Kx^2} \tag{4.4}$$

where; $$\mathrm{K} = \left(\frac{\pi b}{36W}\right)^2 \tag{4.5}$$

In order to solve the Equation 4.1, it should be integrated four times over x. The resulting relation for the transverse displacement obtained by integration is shown in equation 4.6.

$$\mathrm{w}(x) = \frac{1}{EI}\int\int\int\int q(x)dxdxdxdx + C_1x^3 + C_2x^2 + C_3x + C_4 \tag{4.6}$$

If the function q(x) is substituted into the indefinite integral and evaluated the final form of the transverse displacement relation is given in Equation 4.7.

$$w(x) = \frac{b}{2EI} \times \frac{1}{720 \times K^2}\Big[(6K^2x^4 + 83Kx^2 + 16)\sqrt{1 - Kx^2}$$
$$+ 15\sqrt{K}x(4Kx^2 + 3)\sin^{-1}\big(\sqrt{K}x\big)\Big] + C_1x^3 + C_2x^2 + C_3x + C_4 \tag{4.7}$$

The integration constants C_i should only be found for the proper boundary conditions. The beam was assumed to be fixed at the left end and free at the right end, representing the right wing of the UAV. Including the boundary conditions due to loading of the last portion between x=L and x=b/2, all four boundary conditions are given in relations 4.8-4.11.

$$BC1: \quad @x = 0, \quad w(0) = 0 \tag{4.8}$$

$$\mathrm{BC2:} \quad @\mathrm{x} = 0, \quad \left.\frac{dw(x)}{dx}\right|_{x=0} = 0 \tag{4.9}$$

$$\mathrm{BC3:} \quad @\mathrm{x} = \mathrm{L}, \quad -\mathrm{EI}\left.\frac{d^2w(x)}{dx^2}\right|_{x=L} = \int_L^{\frac{b}{2}} q(x)(x-L)dx \tag{4.10}$$

$$\mathrm{BC4:} \quad @\mathrm{x} = \mathrm{L}, \quad -\mathrm{EI}\left.\frac{d^3w(x)}{dx^3}\right|_{x=L} = \int_L^{\frac{b}{2}} q(x)dx \tag{4.11}$$

If evaluated by using the boundary conditions given in Equations 4.8-4.11, the integration constants C_i could be found as given in Equations 4.12-4.15 in the order of the indices.

$$C_1 = -\frac{b}{4EI}\left[\frac{b}{2}\sqrt{1-K\left(\frac{b}{2}\right)^2} + \frac{\sin^{-1}\left(\sqrt{K}\frac{b}{2}\right)}{\sqrt{K}}\right] \tag{4.12}$$

$$C_2 = \frac{b}{4EI}\left[\left(\frac{b^2}{6}-\frac{2}{3}\right)\sqrt{1-K\left(\frac{b}{2}\right)^2}\right] \tag{4.13}$$

$$C_3 = 0 \tag{4.14}$$

$$C_4 = \frac{b}{90EIK^2} \tag{4.15}$$

If the expressions of the integration constants were inserted into the equation 4.7, the transverse displacement of the spars would be in final form as shown in Equation 4.16.

$$w(x) = \frac{b}{2EI} \times \frac{1}{720 \times K^2}\Big[(6K^2x^4 + 83Kx^2 + 16)\sqrt{1-Kx^2}$$
$$+ 15\sqrt{K}x(4Kx^2+3)\sin^{-1}(\sqrt{K}x)\Big] - \frac{b}{4EI}\left[\frac{b}{2}\sqrt{1-K\left(\frac{b}{2}\right)^2} + \frac{\sin^{-1}\left(\sqrt{K}\frac{b}{2}\right)}{\sqrt{K}}\right]x^3$$
$$+ \frac{b}{4EI}\left[\left(\frac{b^2}{6}-\frac{2}{3}\right)\sqrt{1-K\left(\frac{b}{2}\right)^2}\right] x^2 + \frac{b}{90EIK^2} \tag{4.16}$$

Assuming that the structure is a semi-monocoque structure, and the bending (or flexural) load is carried by the spars, whereas the shear load is carried by the skin, the stress on the spars due to the given displacement field could be assumed as shown in Equation 4.17.

$$\sigma_{xx} = EI\frac{d^2w(x)}{dx^2}\frac{y}{I} \tag{4.17}$$

For Equation 4.17, which was derived by substituting the moment term into the stress relation σ=My/I, to hold, it was assumed that, the lateral displacement and w(x) did not couple with each other.

The expression for the second derivative of the transverse displacement was obtained by differentiating Equation 4.16 twice as shown in Equation 4.18.

$$\mathrm{w}''^{(x)} = \frac{b}{2EI}\frac{\sqrt{1-Kx^2}(Kx^2+2)+3\sqrt{K}x\sin^{-1}(\sqrt{K}x)}{6K}$$
$$-\frac{b}{4EI}\left[\frac{b}{2}\sqrt{1-K\left(\frac{b}{2}\right)^2}+\frac{\sin^{-1}\left(\sqrt{K}\frac{b}{2}\right)}{\sqrt{K}}\right]x+\frac{b}{4EI}\left[\left(\frac{b^2}{6}-\frac{2}{3}\right)\sqrt{1-K\left(\frac{b}{2}\right)^2}\right] \tag{4.18}$$

Therefore, the stress relation was transformed into the form as it is given in Equation 4.19, when Equation 4.18 was inserted into Equation 4.17.

$$\sigma_{xx} = \frac{by}{2I}\left\{\frac{\sqrt{1-Kx^2}(Kx^2+2)+3\sqrt{K}x\sin^{-1}(\sqrt{K}x)}{6K}\right.$$
$$\left.-\frac{1}{2}\left[\frac{b}{2}\sqrt{1-K\left(\frac{b}{2}\right)^2}+\frac{\sin^{-1}\left(\sqrt{K}\frac{b}{2}\right)}{\sqrt{K}}\right]x+\frac{1}{2}\left[\left(\frac{b^2}{6}-\frac{2}{3}\right)\sqrt{1-K\left(\frac{b}{2}\right)^2}\right]\right\} \qquad 4.19$$

The stress would be a maximum at the root of the spars for a maximum moment achieved at the root section. The value of the flexural stress should not exceed the allowable stress value of the material. If the Equation 4.19 was evaluated at the root section the relation for the flexural stress would be obtained as given in Equation 4.20.

$$\sigma_{xx}|_{x=0} = \frac{by}{4I}\left[\left(\frac{b^2}{6} - \frac{2}{3}\right)\sqrt{1 - K\left(\frac{b}{2}\right)^2}\right] \tag{4.19}$$

In order to determine the allowable stress value, the safety factor was selected as 1.25, which is a common aeronautical engineering safety factor [26]. The flexural strength of the spar material PA-3200GF was shown in Table 6 as 73 (MPa). If the safety factor is accounted on the flexural strength of the material the allowable stress becomes 58.4 (MPa).

By using the known variables, the total second moment of area of the combination of two spars could be found at the root section as given in Equation 4.20.

$$I = 1.476 \times 10^{-6}\ (ft^2) \tag{4.20}$$

Two third of the given value was the second moment of area of the main spar and the rest was the second moment of area of the rear spar. For this value of the second moment of area, the thickness of the I-section beam at the root was 0.0432 (inches) for the main spar, and 0.0336 (inches) for the rear spar. At the root the flange depth and web thickness was kept uniform for both of the spars, however in order to keep the second moment of area constant, the depth of the flanges increased from the root to the tip. Through the spar span the web thickness was kept constant, whereas the flange depth linearly increased. At the tip the flange depth for the main spar was computed as 0.1 (inches) and the depth of the flanges of the rear spar at the tip as 0.084 (inches). A generic I-Section is given in Figure 21 [27]. According to Figure 21 the section dimensions of the main spar and rear spar at the tip and the root are tabulated in Table 8.

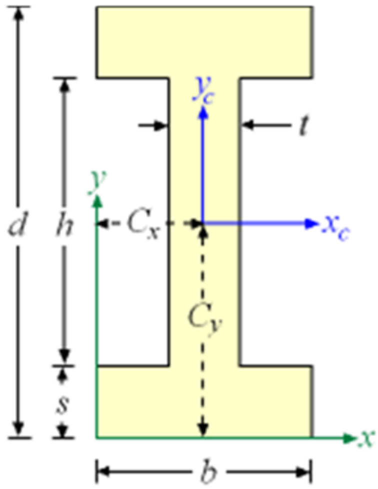

Figure 21: A Generic Square I-beam Section [27]

Table 8: Section Properties of the Spars at Wing Root and Tip in Accordance with Figure 21 (inches)

	Main Spar Root Section	Main Spar Tip Section	Rear Spar Root Section	Rear Spar Tip Section
Section Height, d	1.10	0.70	0.95	0.60
Web Height, h	1.01	0.50	0.88	0.43
Flange Thickness, b	0.55	0.55	0.48	0.48
Web Thickness, t	0.04	0.04	0.03	0.03
Flange Depth, s	0.04	0.10	0.03	0.08

This concludes the geometrical sizing of the spars of the morphing wings. The geometry of the spars was always the same for each phase of the morphing.

4.4.3 Ribs

In this study, apart from their classical purpose of increasing the in-plane rigidity of the wings, the ribs located in between the main and rear spar were also made responsible for the morphing of the wings. There are rib clusters at each wing. The rib structures were designed as telescopic mechanisms. They could extract to increase the chord length of the wing or they can perform the opposite. They could extract or contract gradually to morph between a tapered wing and a rectangular wing. Even they have a gradual motion, all the ribs in the cluster were made co-dependent and could not move individually, except the last rib, which was connected to the end of the spars with a telescopic extension rod in order to extend the span of the wings.

The telescopic ribs were designed as rectangular box structures. The actuation of the ribs in both chordwise and spanwise directions would be governed by piezoelectric inchworm motors. The working principle of a generic piezoelectric inchworm motor is demonstrated in Figure 22. It is essential to notice the initial and final positions of the middle rod in the figure.

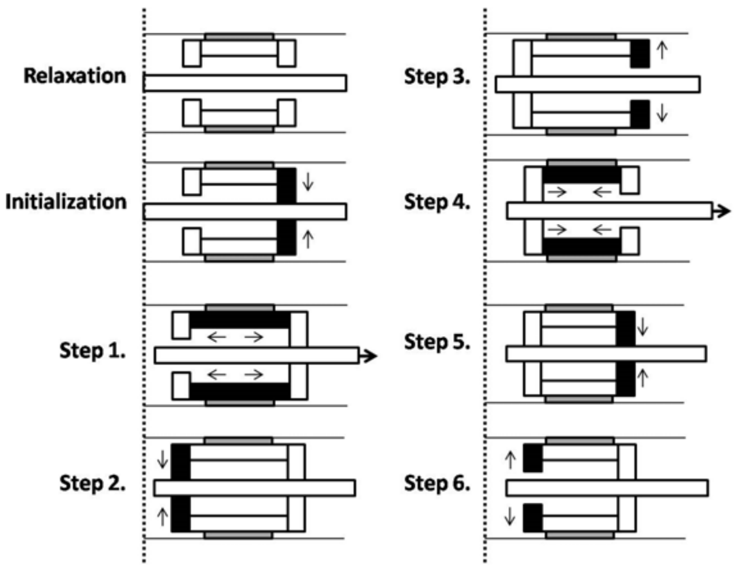

Figure 22: Six Step Actuation Process of an Inchworm Motor [28]

The number of ribs was determined to be 10 for each wing. This number was chosen to avoid large skin panels in the morphing area. For a 10 rib configuration the largest skin panel would have a panel size of 0.84×0.5 (ft). For a rectangular plate, which is simply supported at four ends, the first mode would be 72.3 (Hz) if the classical plate theory was employed [29]. A value this high would not interfere with the first global mode of the wing which was predicted to be below 20 (Hz).

Although there were multiple ribs in the initial structure, these ribs were actuated by inchworm motors located at the root and the tip sections of each wing. The other ribs were designed to be driven by the ribs at the root and the tip sections. The spanwise constant distribution of the ribs was maintained by the hinge arm mechanism devised. The hinge arm was considered to be moving in a guide slide. The guide slides were only employed on the even numbered ribs starting from the wing root. Finally, the mechanism at the last rib section was attached to an inchworm motor for actuation. In order to avoid any free-play, the inchworm motors have the ability to clamp the rod they move on and lock the position of the rib segments at the intended locations. A sketch of the spanwise extension mechanism is given in Figure 23. It should be noted that this mechanism was placed on the ribs at the midway between upper and lower skins. The folding skin would be prevented from interfering with the rib extension mechanism.

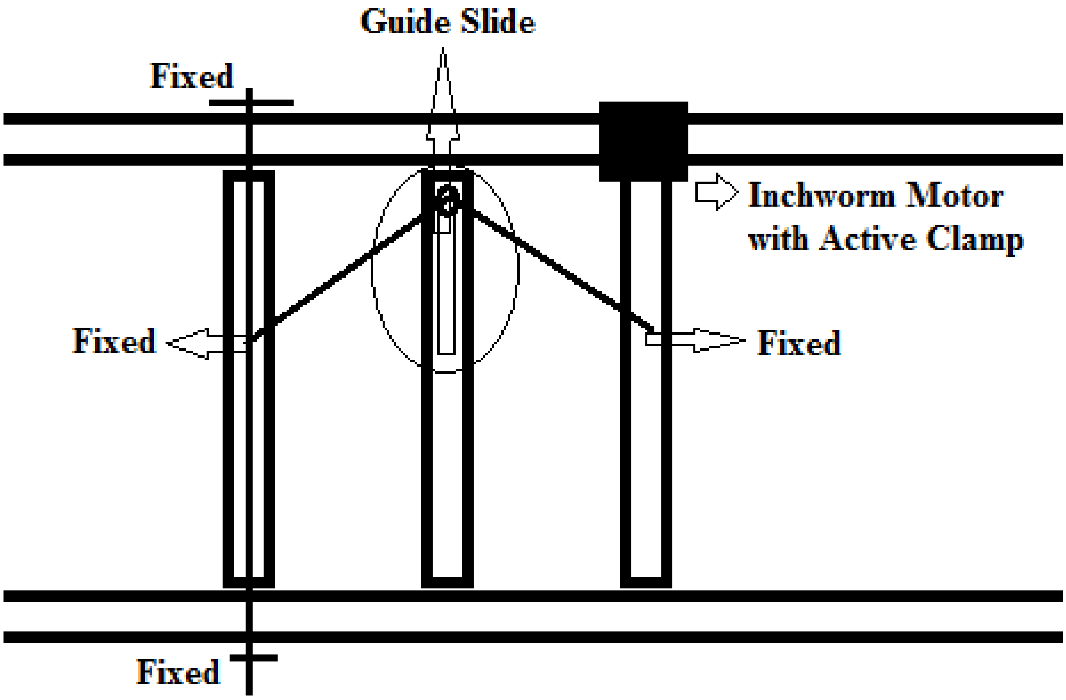

Figure 23: Demonstration of the Suggested Mechanism to Orient the Ribs in Spanwise Direction

The chord extension was employed by two inchworm motors inside the first rib from the root and the second rib from the tip. All the action was supported by the main spar, and the follower ribs were connected through two stiffener rods. The mechanism shown in Figure 24 demonstrates the devised rib extension concept.

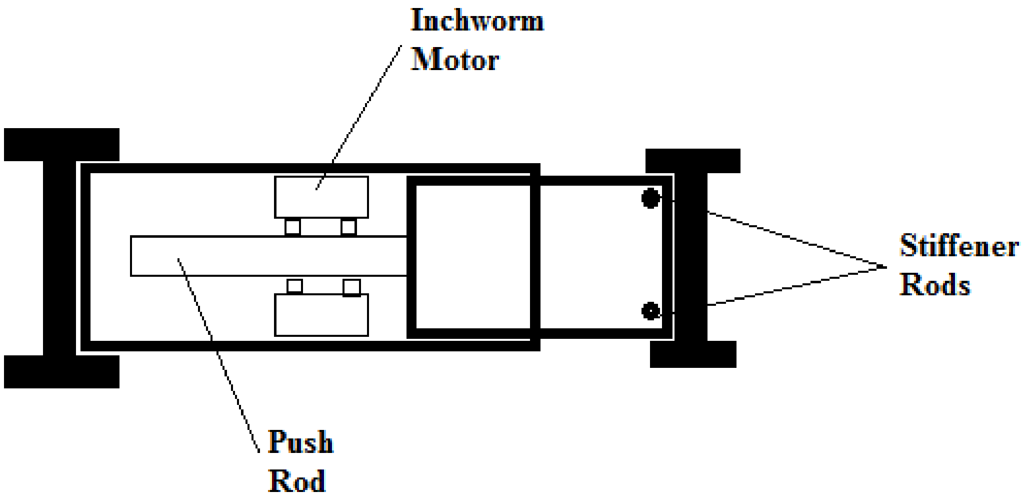

Figure 24: Rib Extension Mechanism with Inchworm Motor Actuation

The appropriate positioning of the ribs effectively change the planform shape of the wing with the help of the paddling spar. The ribs change their chordwise and spanwise positions during different mission configurations. The conceptual drawing of the positions of the ribs at four flight phases are given in Figure 25 - Figure 28.

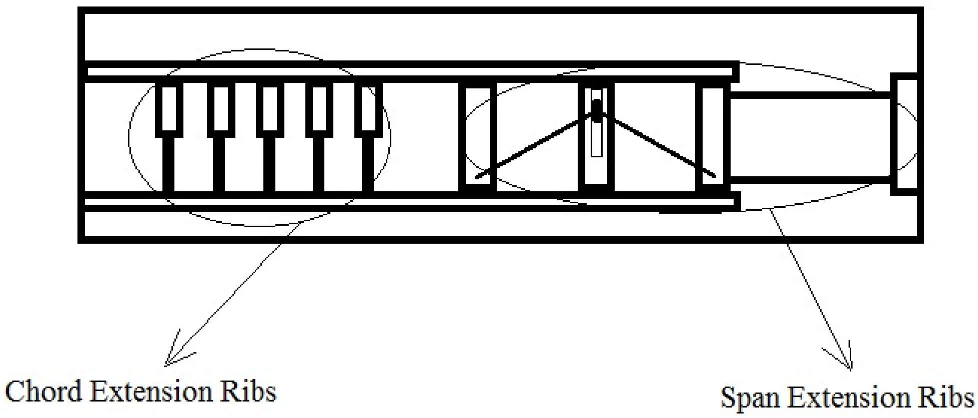

Figure 25: Conceptual Drawing of the Suggested Positions of the Rib Clusters at the Take-off Configuration

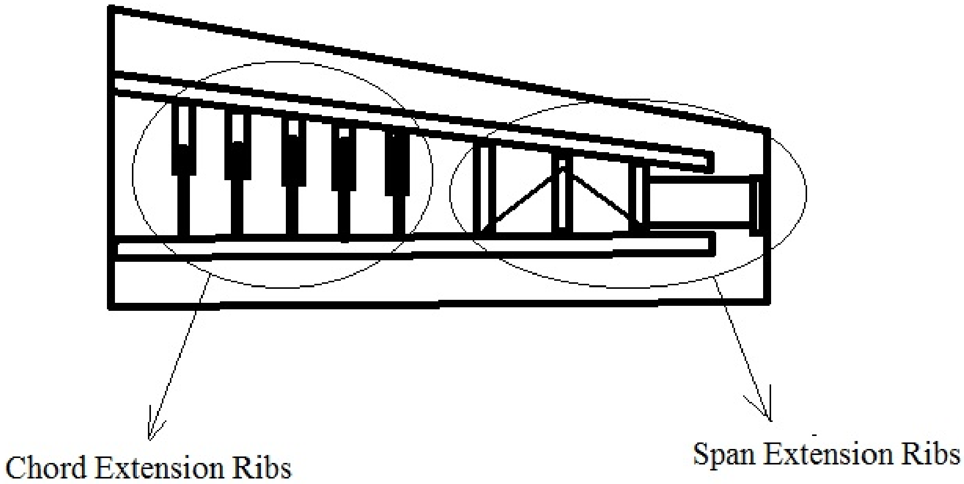

Figure 26: Conceptual Drawing of the Suggested Positions of the Rib Clusters at the Climb Configuration

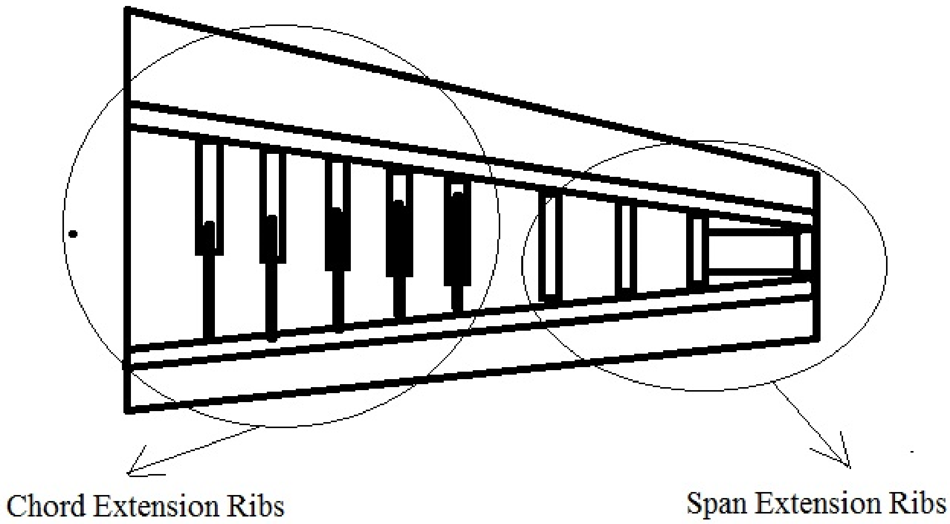

Figure 27: Conceptual Drawing of the Suggested Positions of the Rib Clusters at the Cruise Configuration

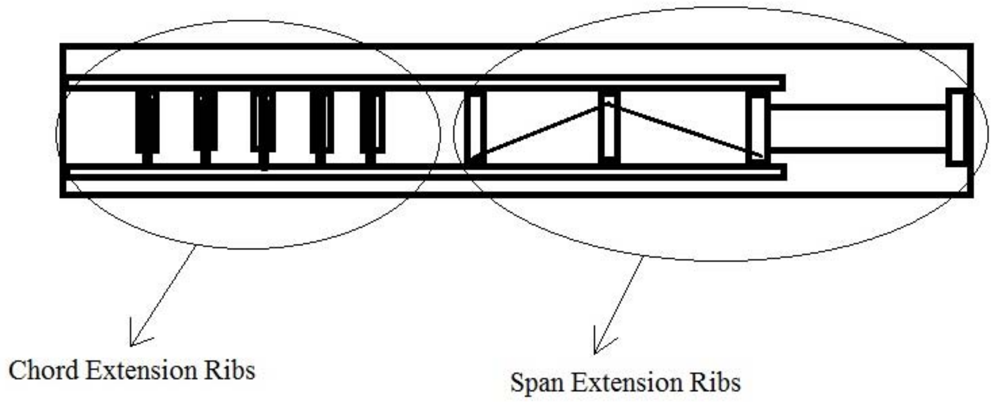

Figure 28: Conceptual Drawing of the Suggested Positions of the Rib Clusters at the Loiter Configuration

The shape of the NACA 4412 profile was preserved by the stiffener rods connected to the upper and lower skin and actuated with separate actuators. The actuators used for this were also piezoelectric inchworm motors. For each wing and each station at least 2 actuators were calculated to be required. The number of the stiffener stations was a compromise between weight and aerodynamic shape. If the aerodynamic gain would not be as sufficient as the additional weight of the actuators, then using too many stations would not be practical. There should be more stations at the leading edge since the first half of the airfoil generates higher pressure gradients. A sample location description of the stiffeners on a generic airfoil is demonstrated in Figure 29. The stiffeners should be supported at the root and the tip section by the inchworm motors and driven by them.

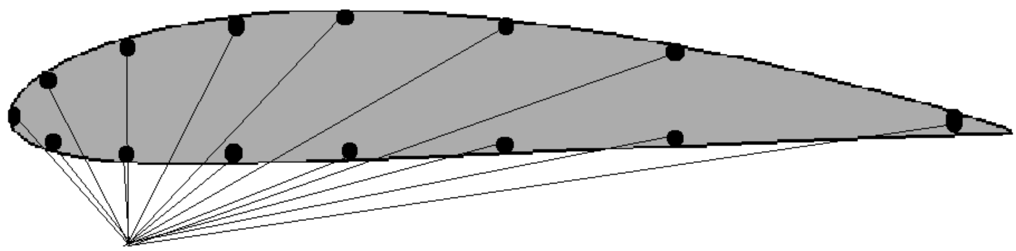

Figure 29: Skin Shape Guiding Stiffeners

4.5 Final Discussion on the Morphing Concept

The Morphing mechanisms suggested in this chapter was assumed to properly work. A series of morphing was sustained by chord extension, span extension, and sweep change mechanisms, which were devised in this thesis study. These mechanisms were not subjected to a formal mechanism synthesis. Neither the complete design of the morphing mechanism nor the morphing wing itself are considered within the scope of this thesis. The main purpose of this chapter was to suggest a possible combination of systems which may lead to the desired wing shapes. The main goal of the thesis is to demonstrate the structural effects of the morphing, providing that a morphing concept, such as the one introduced in this chapter, successfully works.

The morphing mechanisms suggested in this chapter were limited to the structural and material constraints. To illustrate, the taper ratio necessary for the loiter wing configuration could not be provided, since the wing chord through the tip becomes too short if the taper ratio is applied. When the chord is too short, the mechanisms cannot be installed properly to the internal morphing structure. In addition to this, the necessary strain on the skin materials exceeds the reasonable limits when a tapered wing configuration was used at the loiter phase.

To summarize, the conceptual design of the morphing wings were conducted in a realistic manner. All the structural and material limitations were taken into account beforehand. Although the production of a prototype was not planned within the study, the manufacturability was considered along the development of the morphing mechanisms for future referral of this thesis. The wing configurations were designed to perform better but not the best in order to make the manufacturability possible. All these concepts was introduced in this chapter to show that the four wing configurations are somehow achievable.

CHAPTER 5

AERODYNAMIC MODELS OF THE MORPHING WINGS

5.1 Introduction

Aerodynamic analysis of the morphing wings was not considered within the scope of this thesis study. However, for accurate structural analysis acceptable aerodynamic models should be used.

Throughout this thesis, two simple aerodynamic models were used depending on the application. A very simple steady aerodynamic model was used for static linear elastic analysis of the morphing wings considering the flight conditions and the practical usage of the UAV. The second model was based on the unsteady aerodynamics of Theodore Theodorsen [30]. Theodorsen aerodynamics was used in the flutter prediction of the morphing wings.

This chapter was devoted to the summary of the aerodynamic models applied on the morphing wing in order to conduct a series of structural analyses.

5.2 Steady Aerodynamic Model for Linear Elastic Analysis of the Morphing Wings

The steady aerodynamic model was used for the linear elastic analysis of the morphing wings. The pressure distribution described in this section was applied on the structural model for the static stress, strain and deformation analyses conducted on the morphing wings.

The selected airfoil of the wings was NACA 4412 airfoil. The aerodynamic model was developed by using the experimental pressure data given in NACA report No.563 [17]. The pressure data is available for various angles of attack and was used according to the angle of attack setting of the corresponding flight phase, for which the calculations were given in Section 3.3.2.

The chordwise data was obtained from the NACA report, and the spanwise lift distribution was also adopted from a basic approximation method developed by O. Schrenk [31]. The principle of prediction was based on the lifting line theory, which states that the lift distribution over an elliptic wing planform is also elliptic [32]. Schrenk claims that the spanwise lift distribution over a wing should be approximated as the arithmetic mean of the planform shape and an ellipse having major radius equals to the half span of the wing and minor radius set such that, the area under the ellipse equals to L/2c, where c being the mean chord length of the wing and L being the total lifting force.

By setting the constraints for chordwise and spanwise lift distributions; the basic steady aerodynamic model was formed to be used within the linear elastic analysis. Using these spanwise and chordwise distributions, the pressure field around the wing would be developed by using spatial field cards in MSC/Patran®. The pressure distribution for each flight phase will be given in the corresponding subsection.

5.2.1 The Steady Pressure Distribution over the Morphing Wings at the Take-off Configuration

It was previously given in Section 3.3.2.1 that the angle of attack at the take-off phase was considered as 16°. The pressure coefficient of NACA 4412 airfoil at that angle of attack was tabulated for the repeatable experiments done in [17]. The values given were used to obtain the graphical representation of the nondimensional chordwise pressure distribution over the airfoil at 16° angle of attack as shown in Figure 30.

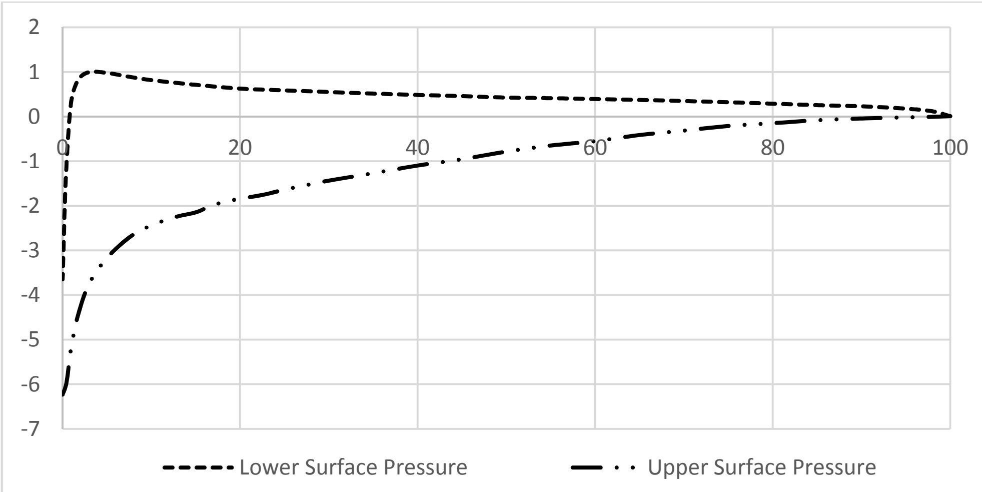

Figure 30: The Chordwise Pressure Distribution over the Morphing Wings at the Take-off Configuration

For the spanwise distribution of the steady aerodynamic pressure, Schrenk method was adopted. The Schrenk distribution was the arithmetic mean of the elliptic distribution with the planform shape of the wing. While taking the average of these two distributions, the area under the curves has to be the same. According to this method, the elliptic, planform shape and Schrenk distributions for the take-off phase of the flight are given in Figure 31.

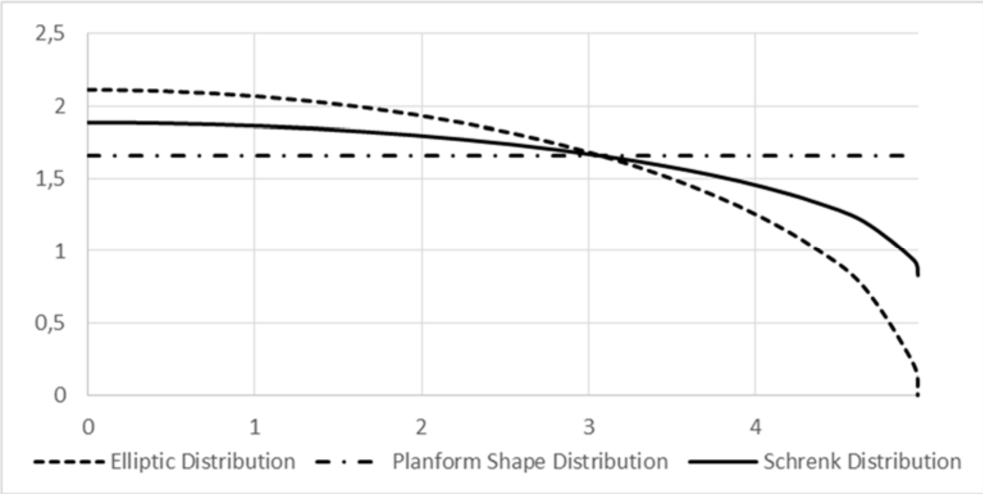

Figure 31: The Spanwise Pressure Distribution over the Morphing Wings at the Take-off Configuration

5.2.2 The Steady Pressure Distribution over the Morphing Wings at the Climb Configuration

The angle of attack at the climb case, with the maximum rate of climb was achieved, was calculated as 2° in Section 3.3.2.2. For the specified angle of attack value, the experimental data from [17] was used to generate the plot of the nondimensional chordwise pressure distribution over the morphing wing at the climb phase. The generated plot is given in Figure 32.

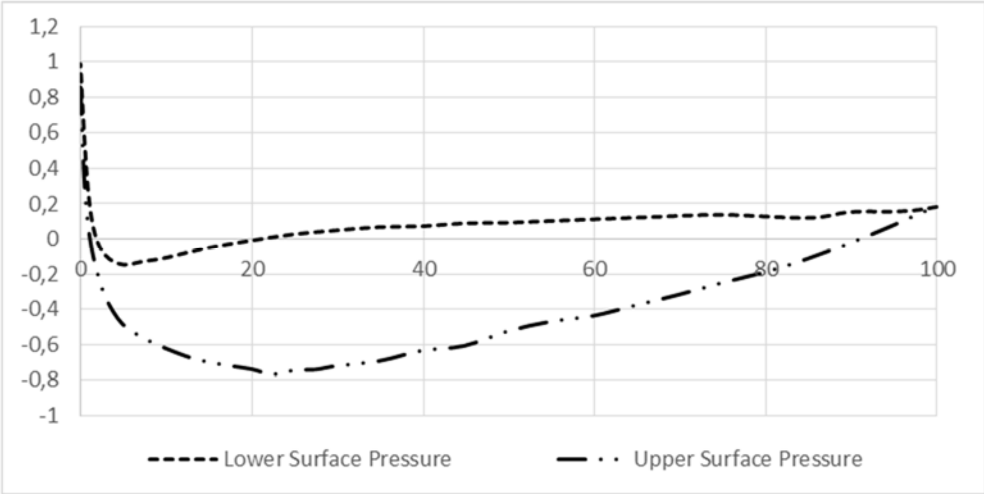

Figure 32: The Chordwise Pressure Distribution over the Morphing Wings at the Climb Configuration

The Schrenk distribution for the climb configuration was calculated and used in the linear elastic analysis of the morphing wings. In Figure 33, the elliptic, the planform shape and the Schrenk distributions for the climb phase are given.

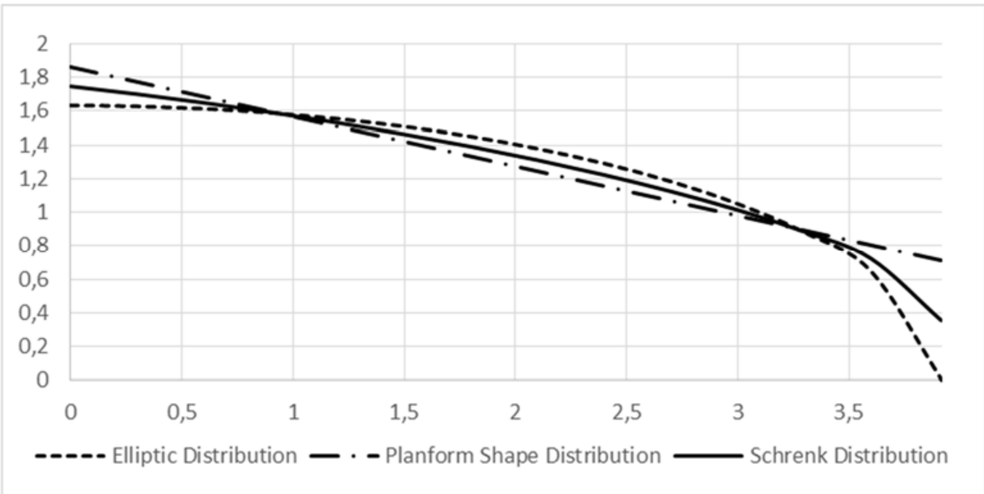

Figure 33: The Spanwise Pressure Distribution over the Morphing Wings at the Climb Configuration

5.2.3 The Steady Pressure Distribution over the Morphing Wings at Cruise Configuration

The angle of attack of the morphing wings at the cruise regime was calculated in Section 3.3.2.3 as 2°, which is the same as the one calculated for the climb case. For the same angle of attack the nondimensional chordwise distribution is the same; hence, it can be reviewed in Figure 32. On the other hand, the Schrenk distribution was different, because the planform properties of the climb and cruise cases were different. The spanwise pressure distribution of the cruise configuration is given in Figure 34, as a combination of the elliptic, the planform shape and the Schrenk distributions.

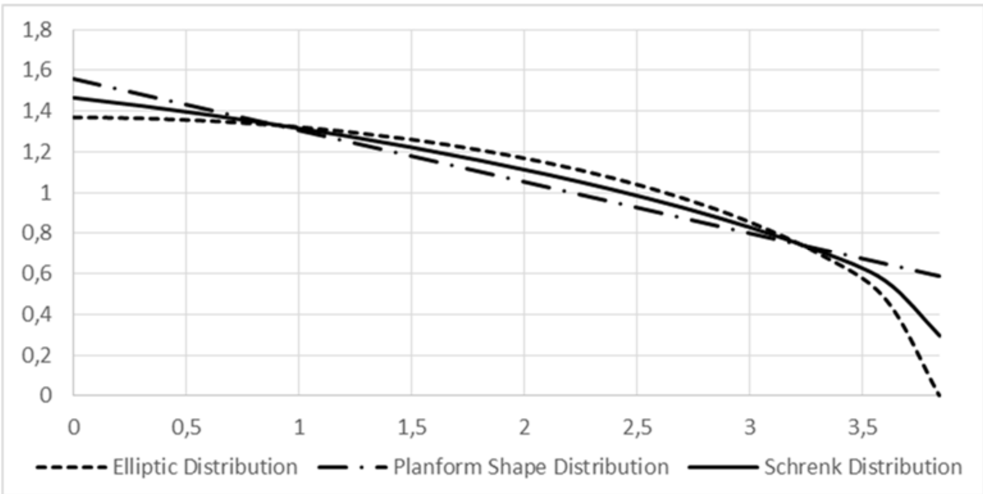

Figure 34: The Spanwise Pressure Distribution over the Morphing Wings at the Cruise Configuration

5.2.4 The Steady Pressure Distribution over the Morphing Wings at the Loiter Configuration

The calculated angle of attack in Section 3.3.2.4 for the loitering wing configuration was 12°. For the calculated angle of attack the experimental chordwise pressure distribution taken from [17] was plotted in Figure 35.

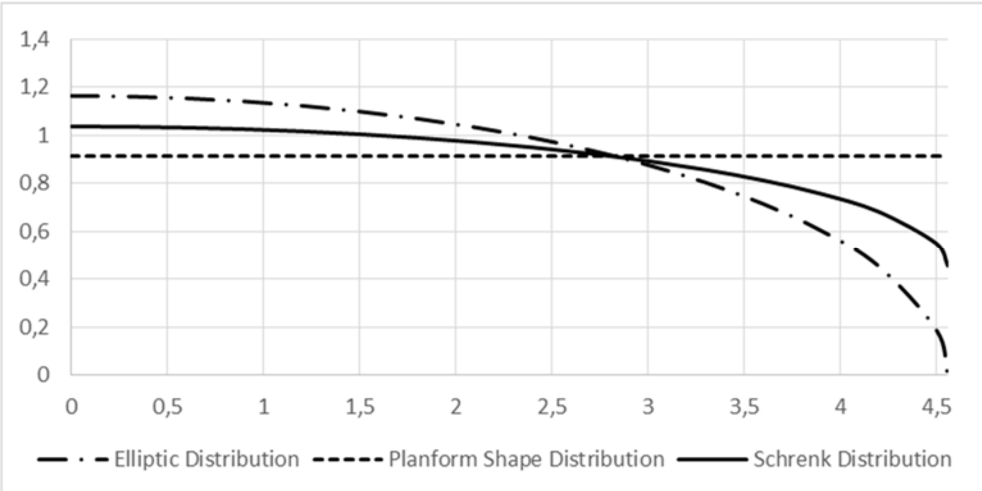

Figure 35: The Chordwise Pressure Distribution over the Morphing Wings at the Loiter Configuration

The spanwise pressure distribution for the loitering configuration of the morphing wings was also calculated by using Schrenk's Approximation Method. The Schrenk distribution obtained and used in the linear elastic analysis is shown in Figure 36, along with the elliptical distribution and the planform shape distribution.

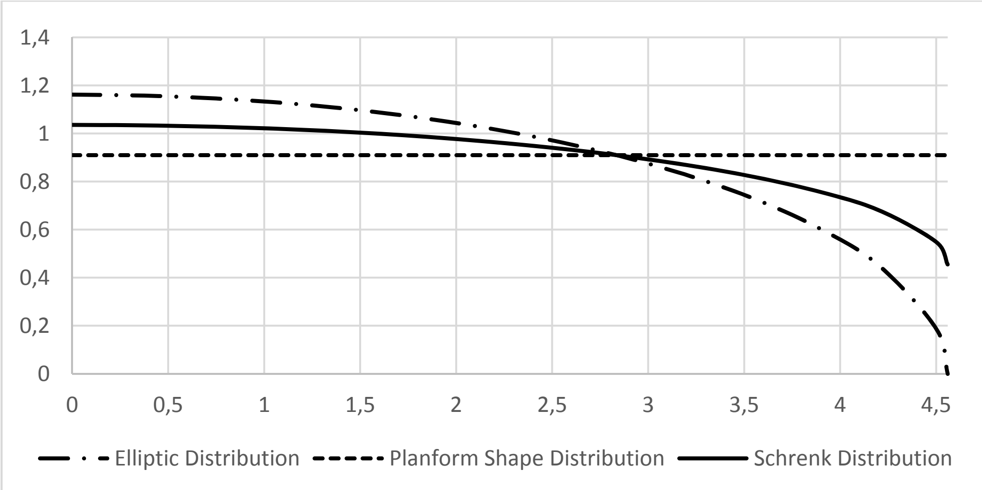

Figure 36: The Spanwise Pressure Distribution over the Morphing Wings at the Loiter Configuration

5.3 Unsteady Aerodynamic Model for Aeroelastic Analyses of the Morphing Wings

The aeroelastic behavior of the morphing wings and the effects of shape change on the aeroelastic behavior of the morphing wings are the key scope of this thesis. A steady aerodynamic model cannot be used for the dynamic aeroelastic solution. Although, some quasi-static and quasi-steady aerodynamic models, which are simpler to implement, exist; within this study, the unsteady aerodynamic solution developed by Theodore Theodorsen was adopted. This theory was considered to be one of the most accurate unsteady aerodynamic models in literature for the wings assumed to be in a low speed flight and low frequency harmonic oscillations [30].

Theodorsen's solution is based on the linear potential theory. It was assumed that, the oscillations of the wing can be modeled as simple harmonic motion, if the amplitudes of the oscillations are small. Based on this assumption the unsteady aerodynamic loads in Equations 2.1-2.3 can be formulated as follows [11].

$$L = \rho b^2\left(V\pi\dot{\alpha} + \pi\ddot{h} - \pi ba\ddot{\alpha} - VT_4\dot{\beta} - T_1 b\ddot{\beta}\right)$$
$$+ 2\pi\rho VbC(k)\left[V\alpha + \dot{h} + b\left(\frac{1}{2} - a\right)\dot{\alpha} + \frac{T_{10}V\beta}{\pi} + \frac{bT_{11}\dot{\beta}}{2\pi}\right] \quad (4.1)$$

$$M_{EA} = -\rho b^2\left\{\pi\left(\frac{1}{2} - a\right)Vb\dot{\alpha} + \pi b^2\left(\frac{1}{8} + a^2\right)\ddot{\alpha} + (T_4 + T_{10})V^2\beta\right.$$
$$\left. + \left[T_1 - T_8 - (c - a)T_4 + \frac{T_{11}}{2}\right]Vb\dot{\beta} - [T_7 + (c - a)T_1]b^2\ddot{\beta} - a\pi b\ddot{h}\right\}$$
$$+ 2\pi\rho Vb^2\left(a + \frac{1}{2}\right)C(k)\left[V\alpha + \dot{h} + b\left(\frac{1}{2} - a\right)\dot{\alpha} + \frac{T_{10}V\beta}{\pi} + \frac{bT_{11}\dot{\beta}}{2\pi}\right] \quad (4.2)$$

$$H = -\rho b^2\left\{\left[-2T_9 - T_1 + T_4\left(a - \frac{1}{2}\right)\right]Vb\dot{\alpha} + 2T_{13}b^2\ddot{\alpha} + \frac{V^2(T_5 - T_4T_{10})\beta}{\pi}\right.$$
$$\left. - \frac{VbT_4T_{10}\dot{\beta}}{2\pi} - \frac{T_4b^2\ddot{\beta}}{\pi} - T_1b\ddot{h}\right\} - \rho Vb^2T_{12}C(k)\left[V\alpha + h \dot{+} b\left(\frac{1}{2} - a\right)\dot{\alpha}\right.$$
$$\left. + \frac{T_{10}V\beta}{\pi} + \frac{bT_{11}\dot{\beta}}{2\pi}\right] \quad (4.3)$$

These three equations were defined as unsteady lift, pitch moment and hinge moment terms corresponding to the oscillating wing. The function C(k) in the equations was referred to as Theodorsen lift deficiency function and defined in terms of Hänkel functions of the second kind. The relation for the C(k) function is given in Equation 4.4.

$$C(k) = \frac{H_1^{(2)}(k)}{H_1^{(2)}(k) + iH_0^{(2)}(k)} \quad (4.4)$$

The T-functions were often referred to as Theodorsen functions. These functions were developed as geometry dependent functions. In the explicit form these functions are formulated as given in Equations from 4.5 to 4.18 [30].

$$T_1 = -\frac{1}{3}\sqrt{1-c^2}(2+c^2) + c(\cos^{-1}c) \tag{4.5}$$

$$T_2 = c(1-c^2) - \sqrt{1-c^2}(1+c^2)\cos^{-1}c + c(\cos^{-1}c)^2 \tag{4.6}$$

$$T_3 = -\left(\frac{1}{8}+c^2\right)(\cos^{-1}c)^2 + \frac{1}{4}c\sqrt{1-c^2}\cos^{-1}c(7+2c^2)$$
$$-\frac{1}{8}(1-c^2)(5c^2+4) \tag{4.7}$$

$$T_4 = -\cos^{-1}c + c\sqrt{1-c^2} \tag{4.8}$$

$$T_5 = -(1-c^2) - (\cos^{-1}c)^2 + 2c\sqrt{1-c^2}\cos^{-1}c \tag{4.9}$$

$$T_6 = T_2 \tag{4.10}$$

$$T_7 = -\left(\frac{1}{8}+c^2\right)\cos^{-1}c + c\sqrt{1-c^2} \tag{4.11}$$

$$T_8 = -\frac{1}{3}\sqrt{1-c^2}(2c^2+1) + c(\cos^{-1}c) \tag{4.12}$$

$$T_9 = \frac{1}{2}\left[\frac{1}{3}\sqrt{1-c^2} + aT_4\right] \tag{4.13}$$

$$T_{10} = \sqrt{1-c^2} + \cos^{-1}c \tag{4.14}$$

$$T_{11} = \cos^{-1}c(1-2c) + \sqrt{1-c^2}(2-c) \tag{4.15}$$

$$T_{12} = \sqrt{1-c^2}(2+c) - \cos^{-1}c(2c+1) \tag{4.16}$$

$$T_{13} = \frac{1}{2}[-T_7 - (c - a)T_1] \tag{4.17}$$

$$T_{14} = \frac{1}{16} + \frac{1}{2}ac \tag{4.18}$$

By direct substitution of the geometrical settings of the wings for desired missions into Equations 4.1-4.3, the unsteady aerodynamic loads can be found. The most important benefit of the Theodorsen aerodynamics is the geometry dependent functions given in Equations 4.5-4.18. Within the scope of the thesis the effects of geometry changes on the structural behavior were investigated; thus, a geometry dependent aerodynamic model was easily employed throughout the analyses.

Once the aerodynamic loadings were calculated for different morphing wing configurations, the results were used in order to construct the reduced order aeroelastic models of the morphing wings.

CHAPTER 6

FINITE ELEMENT MODELING OF THE MORPHING WINGS

6.1 Introduction

The method used for the development of the structural model of a wing generally depends on the application. For instance, if the stress distribution on every structural element was required, the preparation of a detailed structural model would be crucial. Within the scope of this study, the wing structural models were developed in order to investigate global structural behavior of the morphing wings. For this purpose a simplified modeling was accepted to be more convenient as long as it reflects the correct results of the structural analyses.

The proper methods of generating detailed structural models of UAV wings were discussed in [33]. The global structural properties of that wing were compared to the experimental results in that manuscript. A simplified version of that wing model was developed within this thesis. The simplified version of that wing was used to prove the validity of the techniques used during the development of the simplified structural models. Once the simplified model was verified, identical simplified modelling technique was used during the finite element modelling of the morphing wings conceptually designed in this study.

The finite element (FE) models of the morphing wings were used to show the in vacuo dynamic behavior of the wings, the global deformations and stresses under steady flight loads. In addition to these, and more importantly, FE models were the main sources of gathering the information required for the construction of the reduced order aeroelastic model. The geometrical properties, stiffness, mass and inertia information of the system were obtained with the employment of Finite Element Method (FEM). Some of these properties has required some special treatments for their appropriate extraction. For instance, the unit load method application was required to find the location of the elastic axis (EA) of the morphing wings.

This chapter was devoted to the description of the structural modeling techniques applied. These techniques would be validated by the comparison done between the experimental and the theoretical data [33].

6.2 Finite Element Models of the Morphing Wing

In this thesis, instead of modeling the wing with a detailed FE model, a simplified FE modeling technique was used to demonstrate the global structural behavior of the morphing wing.

This simplified model is based on the ideas involved in the "Equivalent Plate Modeling" method. During the conceptual design phase of the complicated wing systems, such as morphing wings, a structural model composed of shell elements could be generated instead of a detailed wing model. Those plate-like structures have the ability to reflect the global structural behavior of the wing. In order to obtain the correct results, the simplified model should have the same stiffness and mass characteristics. Non-structural masses should also be included into the model since they have very significant effects especially on the in-vacuo dynamical behavior of the wings and on the response of the wings under aerodynamic loading. The nonstructural masses considered were such as, paint, servo motors, cabling and so forth [34] [35] [36].

6.2.1 Description of the Simplified Finite Element Modeling Technique Used for the Structural Modeling of the Morphing Wings

The simplified model of the wings involved the main structural members such as spars, ribs and skin. These elements were considered to be plate-like structures which were connected together. In order to generate FE model of these members, it was sufficient to use shell elements. In terms of formulation, shell elements only constitute membrane stiffness and bending stiffness. For this reason, the shell elements behave too stiff in the lateral direction.

The other physical elements in the structure like stiffeners, studs, rivets and fasteners were omitted in the simplified model; however, the results of their structural effects were included mathematically through utilizing their equivalents. While applying this analogy, the elements such as fasteners or bonding materials are supposed to be perfectly rigid and their effects on the structural dynamics of the system were represented by simply merging the coincident nodes of the main structural members. The masses of the omitted members were included in the system either as distributed mass or lumped mass depending on their size, location and density. For elements like bonding materials, which were uniformly applied in real structures, it is more convenient to use distributed mass all over the wing structure. On the other hand, for heavy fasteners such as the ones used to connect wings onto the fuselage should be modeled by using lumped masses at their center of gravity locations.

A simplified model should consist of the lowest possible number of nodes and elements. Although, computational time is very important, the main reason of using coarse meshing is to be able to compute global dynamical characteristics to only get a general opinion about the structural behavior. When using a finer mesh for complex structures like wings, local characteristics may interfere with the global characteristics. If the number of finite elements on a local structural member is increased in a way that all of the local structural modes are computed on that particular structural member, one or more of these local modes may interfere with the global behavior of the structure. This interference may result in a poor graphical representation of the global behavior. To prevent this from happening or at least decrease its effects, it was considered to be crucial to use minimum number of elements with a homogeneous mesh density all over the structure [37].

All of the FE models within this thesis were developed by using MSC/Patran® 2012.2 commercial software, and the FEA were conducted by using

MSC/Nastran® 2012.2 commercial software, except the aeroelastic analyses, which were conducted by using an in-house developed MATLAB® code.

6.2.2 Verification of the Simplified Finite Element Modeling Technique Used for the Structural Modeling of the Morphing Wings

In order to verify the simplified FE Modeling technique used throughout this manuscript, a geometric model of wing torque box was taken from a previous study [33]. The structural model of the wing torque box was developed which was based on the simplified modelling technique described in Section 6.2.1. The developed simplified structural model is given in Figure 37.

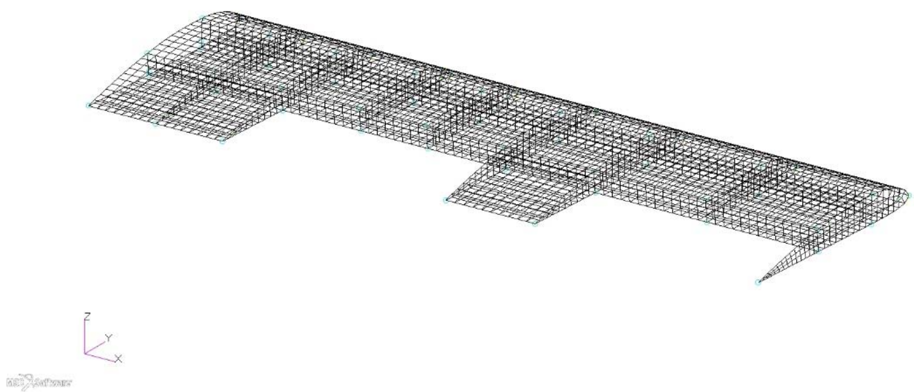

Figure 37: Simplified Model of the Wing Torque Box in Reference [33]

There were originally 19790 elements in the detailed model of the wing torque box whereas the simplified model had only 4002 elements which were 20.22 percent of the detailed model. Even the simplified model had less number of elements, it showed good accuracy compared to the detailed model when out-of-plane bending and torsional modes were concerned. However, in-plane bending behavior shows less accuracy and became stiffer in lateral direction compared to the original model as it was expected because the simplified model was formed only by shell elements.

The results of natural frequency and mode shape analysis for the simplified and detailed models were compared together with the experimentally obtained resonance frequencies were given in Table 9. The Figure 38 - Figure 41 show the corresponding mode shapes for the 1st out-of-plane bending, the 1st in-plane bending, the 1st torsional and the 2nd out-of-plane bending natural frequencies of the simplified model respectively as referred to the reference.

Table 9: Comparison of the In Vacuo Dynamic Behavior of the Simplified Model and the Detailed Model via Experimental Results (Hz)

Mode Shape	Detailed Model Natural Frequencies (FEM)[33]	Simplified Model Natural Frequencies (FEM)	Wing Resonance Frequencies (Experimental) [33]	% Difference of Detailed Model with Respect to Experimental Data [33]	% Difference of Simplified Model with Respect to Experimental Data
1. Out-of-plane Bending	14.90	14.60	14.75	~0.99	~-0.99
1. In-plane Bending	50.16	56.11	43.50	~15.32	~28.99
1. Torsional	63.30	67.84	66.75	~-5.17	~1.63
2. Out-of-plane Bending	93.00	90.47	93.0	~0.00	~-2,72

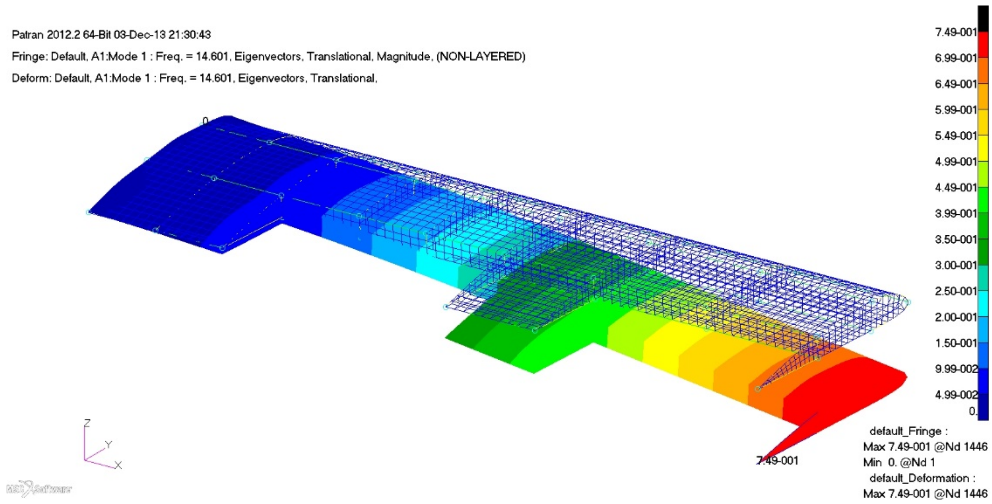

Figure 38: 1st Out-of-plane Bending Mode of the Simplified Model at 14.60 (Hz)

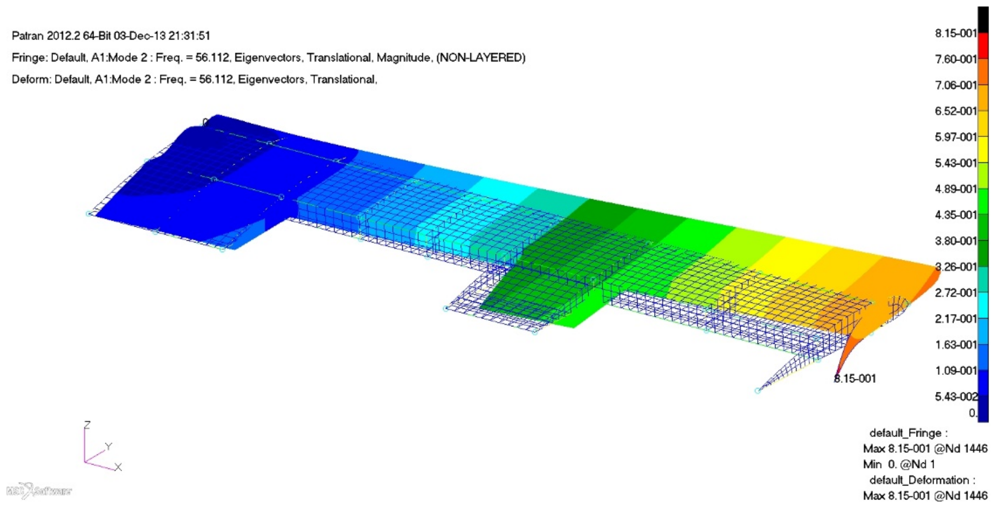

Figure 39: 1st In-plane Bending Mode of the Simplified Model at 56.11 (Hz)

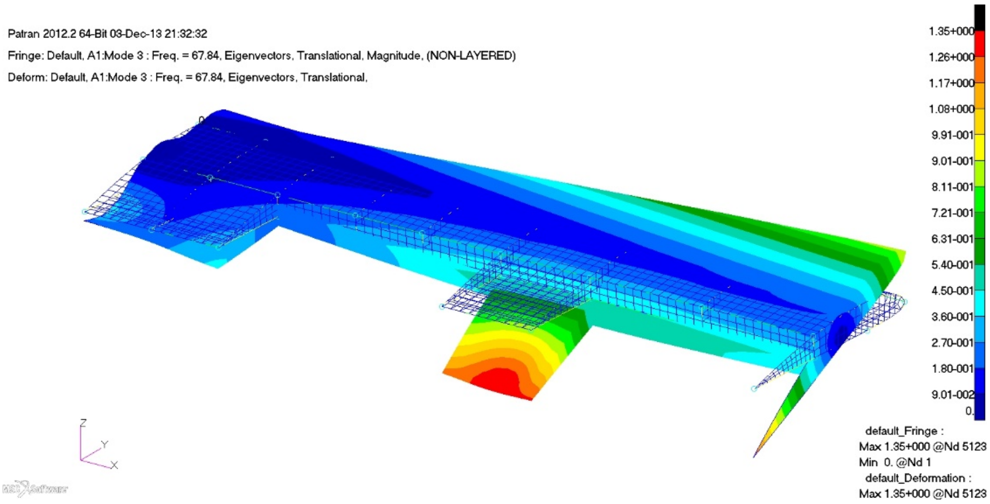

Figure 40: 1st Torsional Mode of the Simplified Model at 67.84 (Hz)

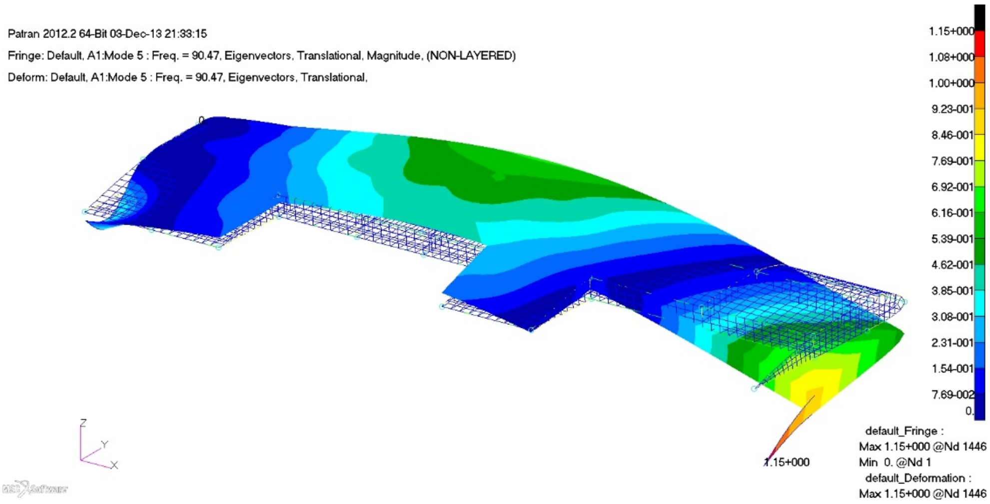

Figure 41: 2nd Out-of-plane Bending Mode of the Simplified Model at 90.47 (Hz)

The accuracy of the simplified model for the first out-of-plane and first torsional modes were found approximately as 1 percent and 1.6 percent, respectively. The accuracy of the model in terms of out-of-plane bending was the same with the detailed model. The accuracy of the simplified model in terms of the torsional mode was better than the original detailed model. The reason behind this was the one-dimensional elements used in the detailed model in order to demonstrate a better lateral behavior. Since one-dimensional elements had no torsional stiffness, the overall torsional stiffness of the model was reduced. On the other hand, in the simplified model used in this thesis, the lateral rigidity was not considered to be important since lateral modes were not taken into account in aeroelastic analyses of wings. The lateral modes do not have a coupling term with the transverse and torsional modes. For this reason, the torsional behavior was demonstrated better in the simplified model, if it was compared with the original model.

The wing structural models used in the structural analyses of this thesis study were developed according to the procedure used in the verified, and so-called simplified model. Since the simplified model is very accurate, when compared to the experimental results, for first out-of-plane bending and first torsional natural frequencies, this technique had a positive effect on the main scope of the thesis, which is the flutter prediction of the morphing wings. In order to have accurate aeroelastic analyses, i.e. flutter analysis, the bending-torsion frequency ratio had great importance. The more accurately this ratio is calculated, the more accurate the flutter prediction is obtained [6][7][8][9].

6.2.3 The Finite Element Model of the Morphing Wings at the Take-off Configuration

The conceptual design of the take-off phase of the morphing wings of the UAV was conducted and described in Section 3.3.1.1. Considering the geometrical constraints set for that design, a FE model of the morphing wing was developed. The developed FE model is shown in Figure 42, and the Table 10 gives the summary of the type and numbers of elements used in the model. The information in Table 10 was given in order to give an insight about the mesh density of the FE model.

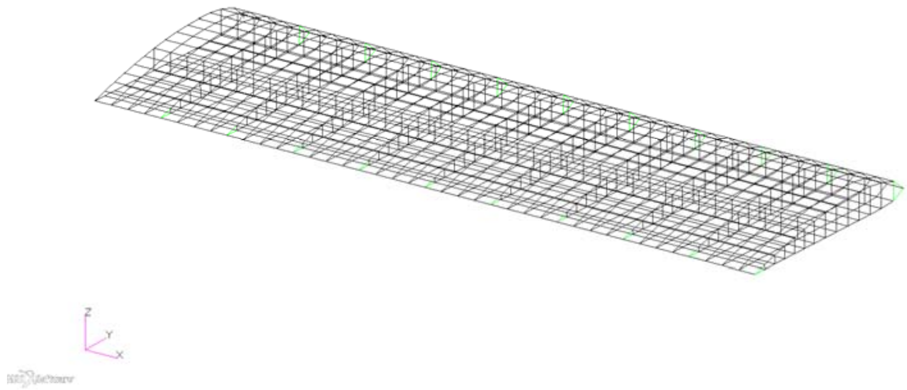

Figure 42: The Finite Element Model of the Right Morphing Wing at the Take-off Configuration

Table 10: The Number of Elements and Nodes Used in the Finite Element Model of the Right Morphing Wing at the Take-off Configuration

CQUAD4	1320
TRIA3	20
Total Elements	1340
Total Nodes	1148

6.2.4 The Finite Element Model of the Morphing Wings at the Climb Configuration

The conceptual design of the climb phase geometry was conducted in Section 3.3.1.2 of this manuscript. According to the geometrical description given at that section, the FE model of the wing was developed and FE model is shown in Figure 43. Some element properties of this model are given in Table 11.

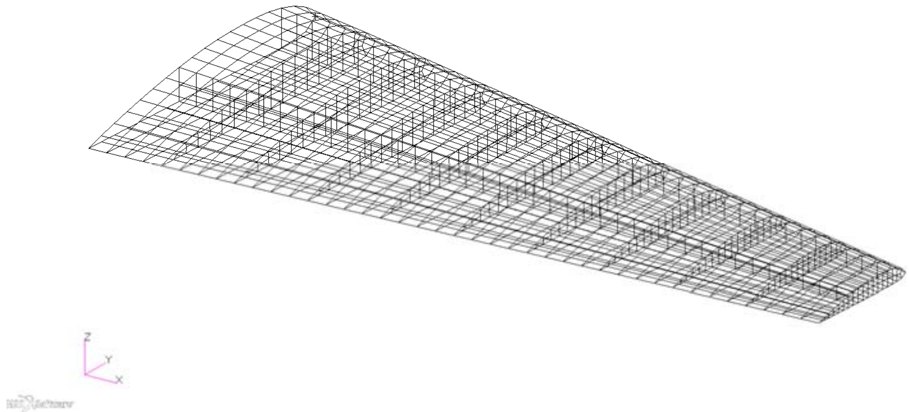

Figure 43: The Finite Element Model of the Right Morphing Wing at the Climb Configuration

Table 11: The Number of Elements and Nodes Used in the Finite Element Model of the Right Morphing Wing at the Climb Configuration

CQUAD4	1940
TRIA3	0
Total Elements	1940
Total Nodes	1708

6.2.5 The Finite Element Model of the Morphing Wings at the Cruise Configuration

The same FE model development procedure was applied to the cruise configuration data defined at Section 3.3.1.3. The developed FE model is shown in Figure 44, and the elemental attributes of the model are tabulated in Table 12.

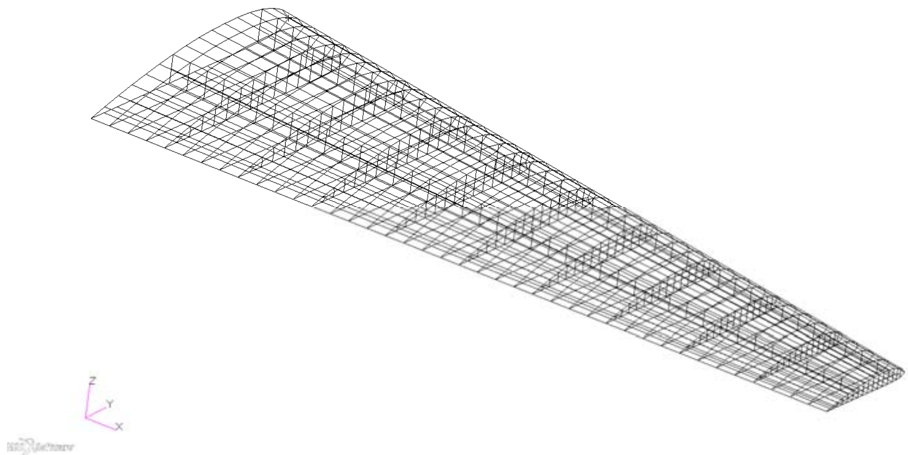

Figure 44: The Finite Element Model of the Right Morphing Wing at the Cruise Configuration

Table 12: The Number of Elements and Nodes Used in the Finite Element Model of the Right Morphing Wing at the Cruise Configuration

CQUAD4	1740
TRIA3	0
Total Elements	1740
Total Nodes	1524

6.2.6 The Finite Element Model of the Morphing Wings at the Loiter Configuration

What the last configuration that the morphing wing could transform into was considered to be the loiter configuration, for which the conceptual design was conducted at Section 3.3.1.4. The FE model developed for the loiter configuration can be seen in Figure 45, and the tabulated finite element properties can be followed in Table 13.

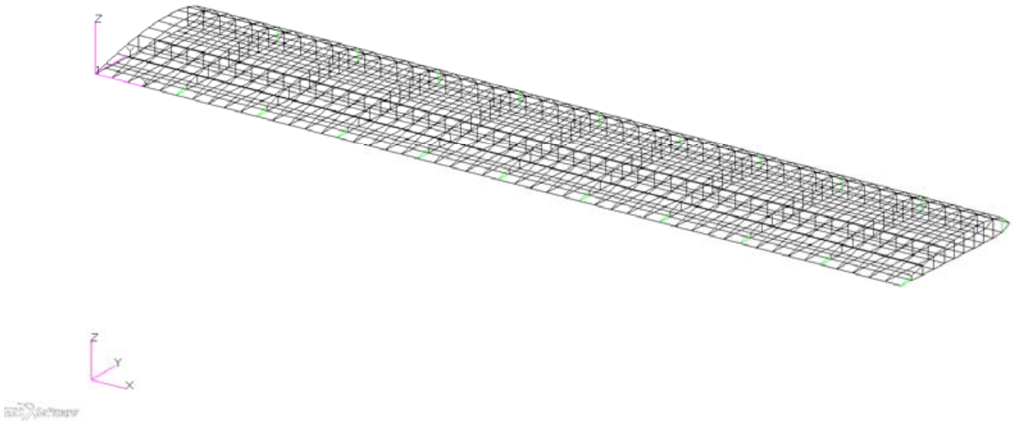

Figure 45: The Finite Element Model of the Right Morphing Wing at the Loiter Configuration

Table 13: The Number of Elements and Nodes Used in the Finite Element Model of the Right Morphing Wing at the Loiter Configuration

CQUAD4	1290
TRIA3	20
Total Elements	1310
Total Nodes	1122

CHAPTER 7

FINITE ELEMENT ANALYSES OF THE MORPHING WINGS

7.1 Introduction

The FE models of the morphing wings at different flight phases were developed and given in Section 6.2. Those models would be studied not only to construct the reduced order aeroelastic model but also to understand the effects of the morphing phenomena on the structural behavior of the wings.

7.2 Linear Elastic Analysis

The linear elastic analysis conducted on the morphing wings was focused on two points. The first one was the stress-strain analysis under the steady aerodynamic loading corresponding to the desired missions. The second one was mainly to locate the center of gravity and the elastic axis of the wing configurations. The information gathered during the linear elastic analyses would be used to construct the reduced order aeroelastic models corresponding to each mission configuration.

7.2.1 Stress-Strain Analysis of the Morphing Wing

It was believed that the verification of the structure's capability to withstand the aerodynamic loads was a necessary and sufficient condition before conducting aeroelastic analysis. Thus, the linear elastic analyses were conducted beforehand.

Furthermore, in order to clearly visualize and compare the aeroelastic behavior of the morphing wings, the wing stiffness should not be too high. Hence, stress-strain analysis were conducted in such a way that, the designed structure should be capable of carrying loads with a safety factor at most 1.5 for the least stiff morphed configuration.

In this thesis, it was assumed that the morphing mechanisms, which were primarily responsible for the shape change of the internal structure, has the capability to withstand the aerodynamic loads transmitted on them. The mechanisms were also assumed to deform by obeying the constraints from the strain field of the main structural members.

The chordwise and spanwise aerodynamic load distributions on the wings, which were actually varied for each phase of the flight, were applied on each wing configuration. In addition to the steady flight loads analysis of all configurations, an ultimate loading case of 4.5g maneuver was also analyzed for the most slender configuration of the wing, which was achieved at the loiter phase.

The displacement fields, strain fields and stress fields and other results under the steady aerodynamic loading are shown for each phase of the flight envelope in a separate subsection. First, the results of the loitering configuration will be given.

7.2.1.1 Stress-Strain Analysis of the Morphing Wing at the Loiter Configuration

The highest aspect ratio wing configuration was achieved for the loiter mission. For this reason, the ultimate loading case study was only conducted for the loiter configuration. For the wing conceptually designed in Sections 3.3.1.4 and 3.3.2.4, the linear static analyses were conducted by using MSC/Nastran® Finite Element Analysis (FEA) software. The results for steady level loitering mission and a 4.5 g maneuver during the loitering mission would follow respectively.

7.2.1.1.1 The Stress-Strain Analyses of the Morphing Wing at the Loiter Configuration for the Steady-Level Flight Conditions

A steady-level flight condition was referred to as a flight at fixed altitude with no acceleration. For this case the lift has been equal to the total weight of the UAV. In other words, the summation of the pressure distribution adds up to the half of the weight of the UAV for each wing. Within this study, only the right wing of the UAV was investigated, since the wing structure was believed to be symmetrical.

The analyses were conducted under the steady aerodynamic loading discussed in Section 5.2. The pressure distribution was applied on the FE model by using the 'Spatial Field' utility of MSC/Patran®. The combination of the chordwise and spanwise pressure distributions were applied on the upper and lower surfaces of the wing. The pressure field contours of the upper and lower skins of the morphing wing at the loiter configuration are given in Figure 46 and Figure 47 respectively.

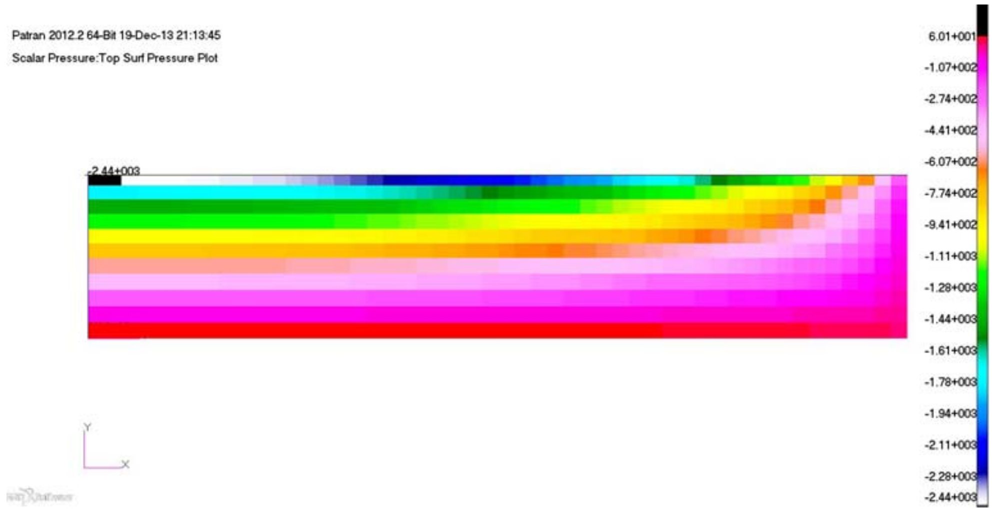

Figure 46: Pressure Distribution on the Upper Skin of the Morphing Wing at the Loiter Configuration in Steady-Level Flight (Pa)

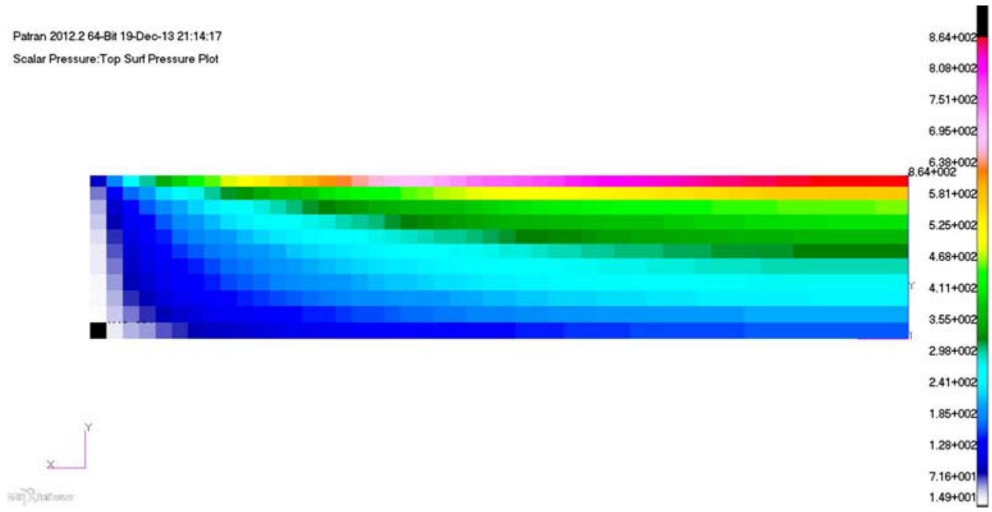

Figure 47: Pressure Distribution on the Lower Skin of the Morphing Wing at the Loiter in Steady-Level Flight (Pa)

Under the loading shown in Figure 46 and Figure 47, the maximum stress value on the wing was found as 7.18 (MPa), which is below the tensile strength value of the internal structure material PA-3200GF and the skin material PA-1101 which are 51 (MPa) and 48 (MPa) respectively. Additionally, the strain values were also found to be small enough to remain in the linear elastic deformation region. The maximum percent elongation on the wing structure was calculated as 0.169. The von Misses stress and strain distributions are given in Figure 48 and Figure 49 respectively. The displacement field under the prescribed loading is shown in Figure 50.

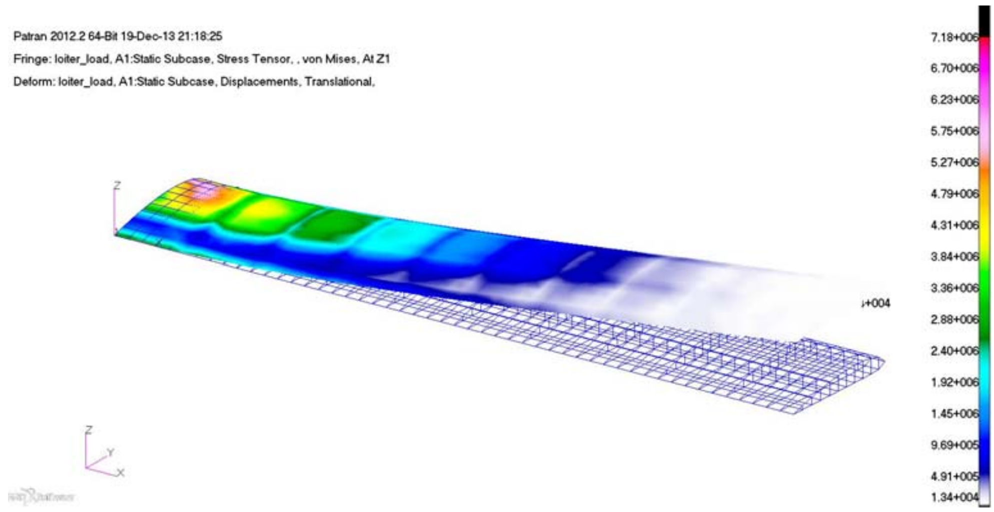

Figure 48: von Misses Stress Distribution over the Morphing Wing under the Aerodynamic Loading of the Loiter Configuration at Steady-Level Flight (Pa)

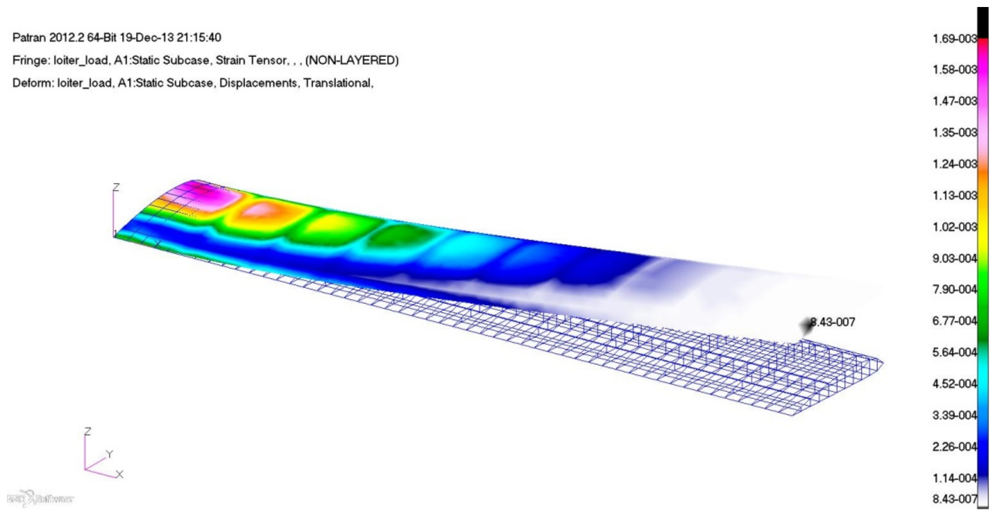

Figure 49: von Misses Strain Distribution over the Morphing under the Aerodynamic Loading of the Loiter Configuration at Steady-Level Flight

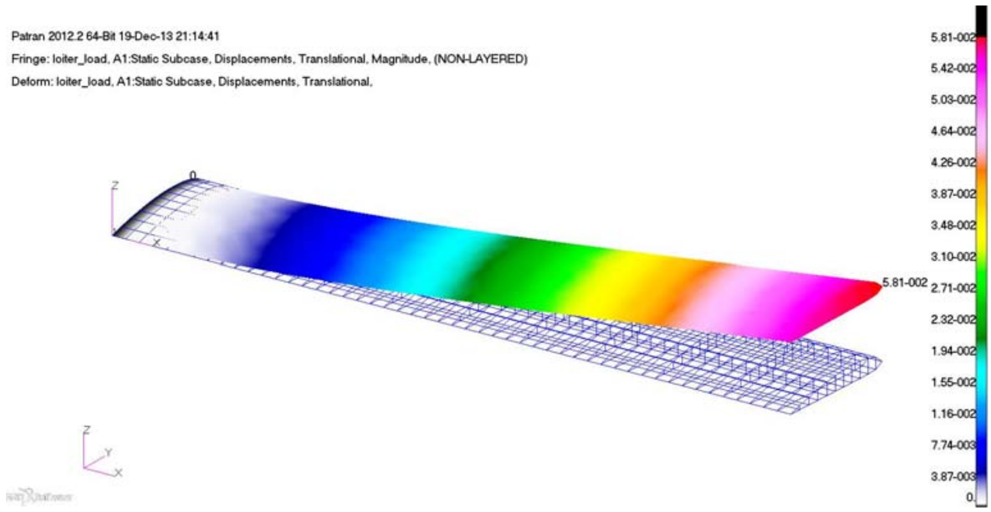

Figure 50: Displacement Field over the Morphing Wing under the Aerodynamic Loading of the Loiter Configuration at Steady-Level Flight (m)

7.2.1.1.2 The Stress-Strain Analyses of the Morphing Wing at the Loiter Configuration for the Ultimate Loading Case

The UAV with morphing wings was intended to achieve a successful maneuver of 3g load factor. The wings should withstand 50 % higher loads than the 3g load factor maneuver without any failure in the structure, namely 4.5g load factor [15]. During the analysis for the ultimate loading case, it was assumed that the thrust vector and the drag vector are aligned so that the lift could be defined as;

$$L = nW \tag{7.1}$$

Achieving the condition given in Equation 7.1 was possible by increasing the load factor of the spatial field used to define the pressure distribution for the steady-level flight conditions discussed in Section 7.2.1.1.1. The pressure distribution on the upper and lower skin, under the 4.5g aerodynamic loading is shown in Figure 51 and Figure 52 respectively.

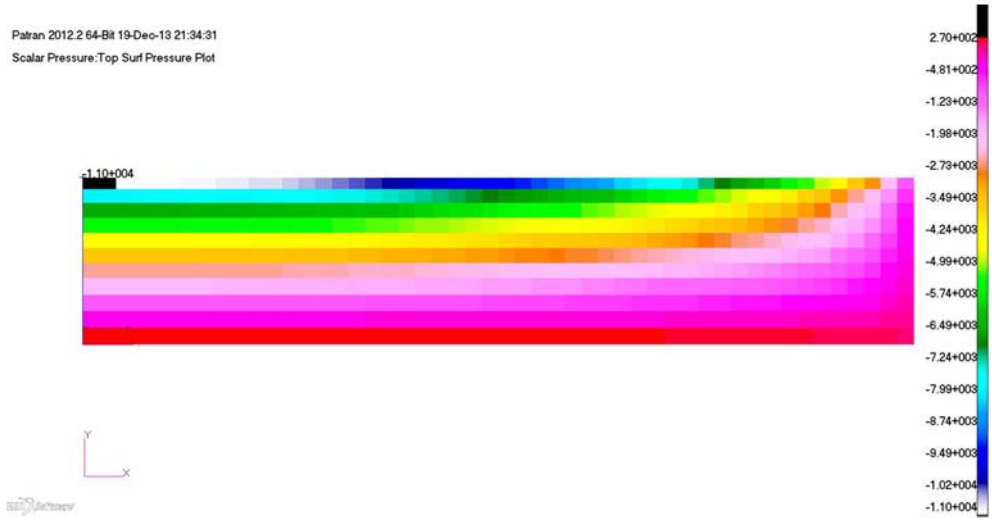

Figure 51: Pressure Distribution on the Upper Skin of the Morphing Wing at the Loiter Configuration for a 4.5g Maneuver Case (Pa)

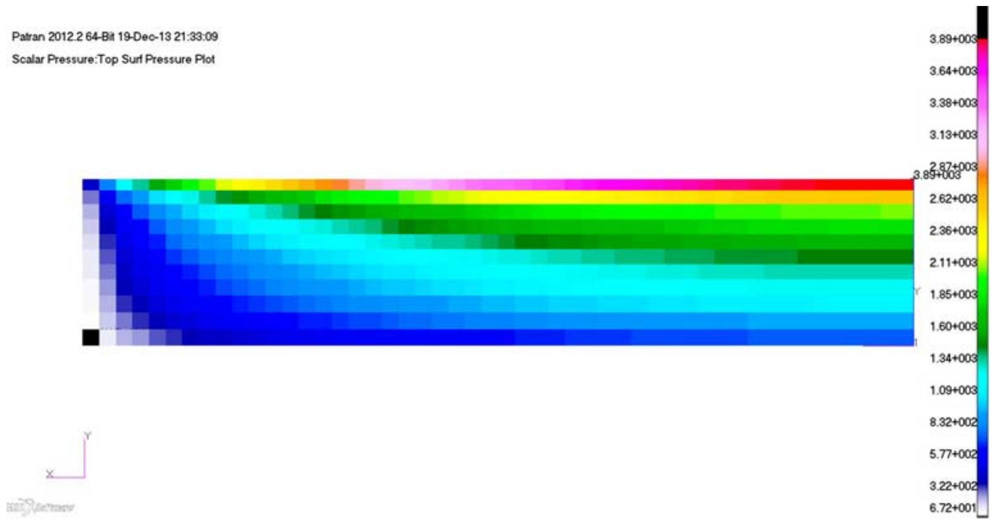

Figure 52: Pressure Distribution on the Lower Skin of the Morphing Wing at the Loiter Configuration for a 4.5g Maneuver Case (Pa)

Under the action of the given aerodynamic loading the maximum stress value computed on the wing was 32.3 (MPa). This value is lower than the tensile strength of the materials used for the internal structure and the skin. The maximum stress value was achieved at the root of the main spar, hence, the allowable stress was 34 (MPa) with a factor of safety of 1.5. This showed that the designed structure could withstand the possible ultimate loading during the flight. The stress field on the wing structure is shown in Figure 53.

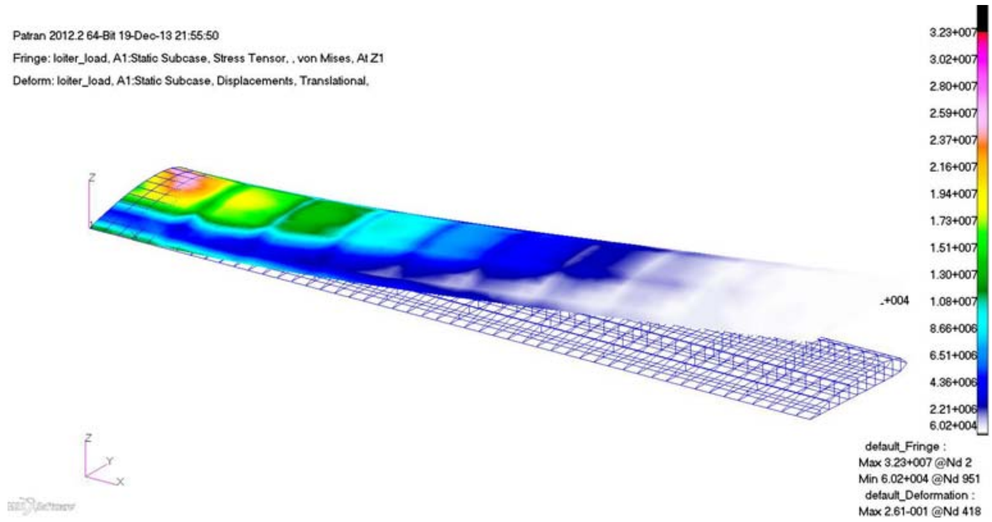

Figure 53: von Misses Stress Distribution over the Morphing Wing under the Aerodynamic Loading of the Loiter Configuration at the Ultimate Loading of a 4.5g Maneuver (Pa)

The strains observed on the wing structure were still low enough to be considered within the linear elastic region. The highest elongation percentage on the wing structure was 0.761. The strain field and the displacement field of the wing structure for 4.5g maneuver case are shown in Figure 54 and Figure 55 respectively.

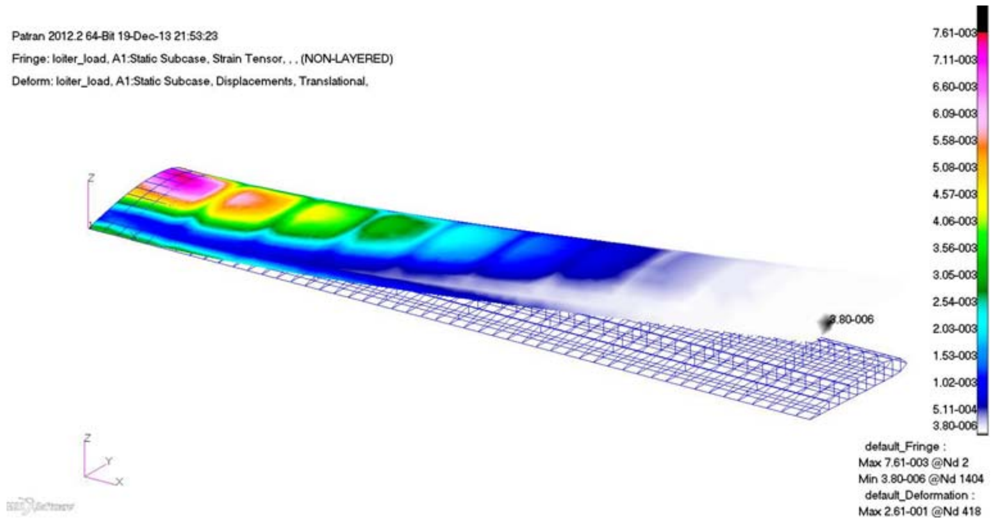

Figure 54: von Misses Strain Distribution over the Morphing Wing under the Aerodynamic Loading of the Loiter Configuration at the Ultimate Loading of a 4.5g Maneuver

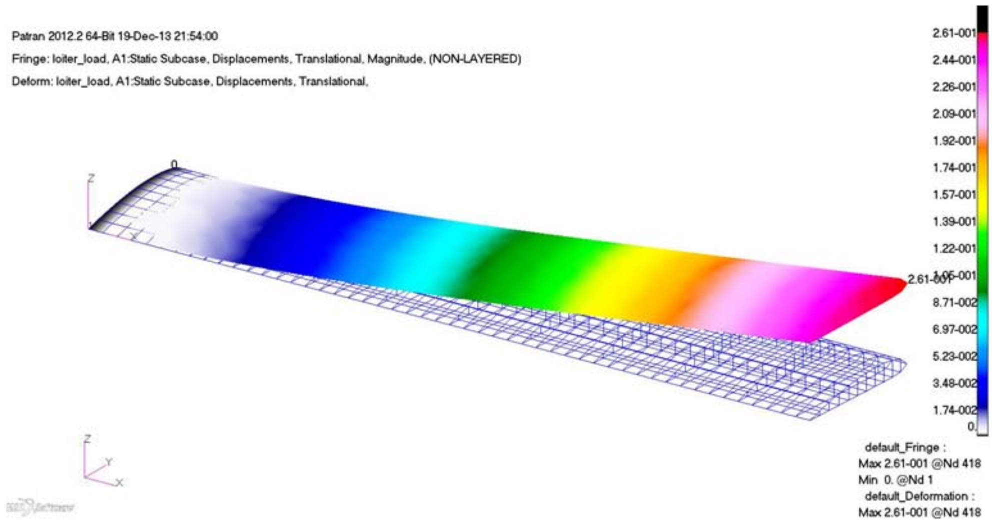

Figure 55: Displacement Field over the Morphing Wing under the Aerodynamic Loading of the Loiter Configuration at the Ultimate Loading of a 4.5g Maneuver (m)

7.2.1.2 Stress-Strain Analysis of the Morphing Wing at the Take-off Configuration

The shortest period of time, in which the wing was morphed into within the flight regime, is the take-off phase. Despite this, the linear elastic analyses should be conducted to assure that the wing would sustain the necessary strength to withstand the aerodynamic loads during the take-off period.

The analysis was based on a steady flight where there is no translational or rotational acceleration. In other words, only 1g analysis was performed on the wing, since by definition, there are no continuous higher load factor maneuvers in a take-off phase. The aerodynamic loading applied on the structural model was the three dimensional combination of the chordwise and spanwise pressure distribution given in Section 5.2.1. The pressure distribution applied on the structural model on the upper surface and lower surface of the right wing are given in Figure 56 and in Figure 57, respectively.

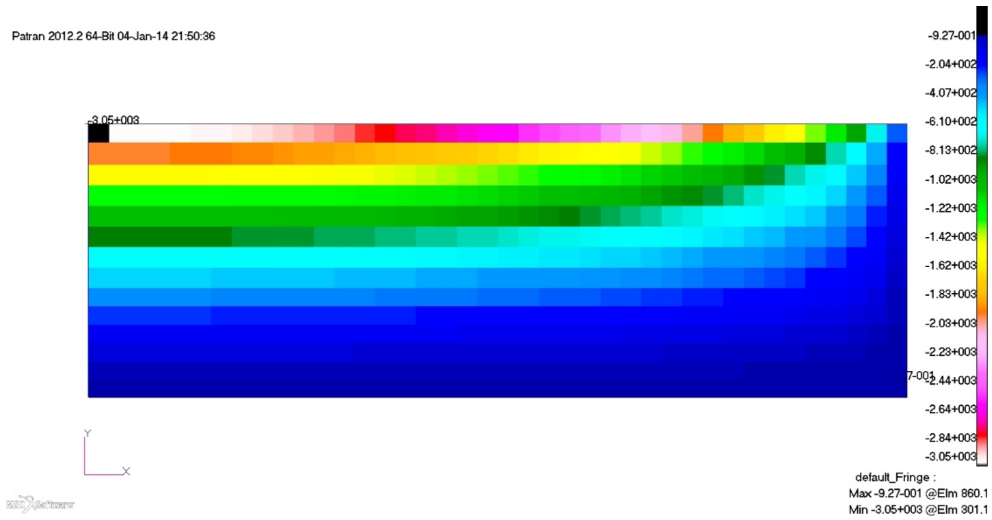

Figure 56: Pressure Distribution on the Upper Skin of the Morphing Wing at the Take-off Configuration in Steady-Level Flight (Pa)

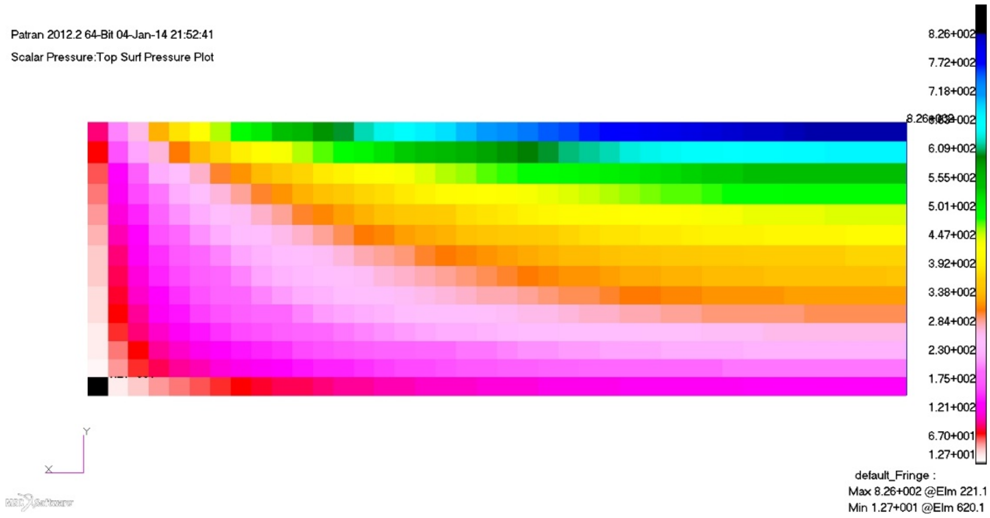

Figure 57: Pressure Distribution on the Lower Skin of the Morphing Wing at the Take-off Configuration in Steady-Level Flight (Pa)

After the approximated pressure distribution over the morphing wing had been applied, the static elastic analysis was conducted to compute the displacement, strain and stress fields. The fringe results for the computed displacement, strain and stress fields are shown in Figure 58, Figure 59 and Figure 60, respectively.

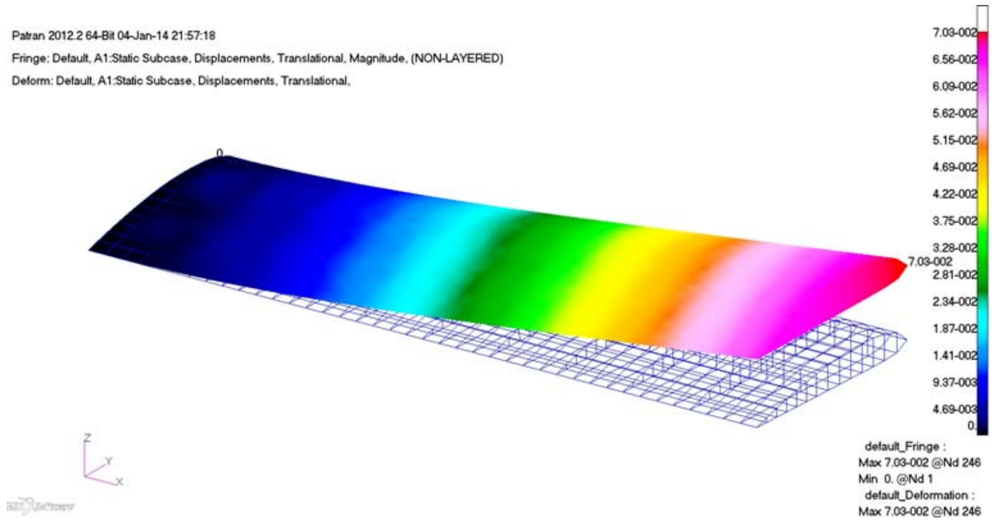

Figure 58: Displacement Field over the Morphing Wing under the Aerodynamic Loading of the Take-off Configuration at Steady-Level Flight (m)

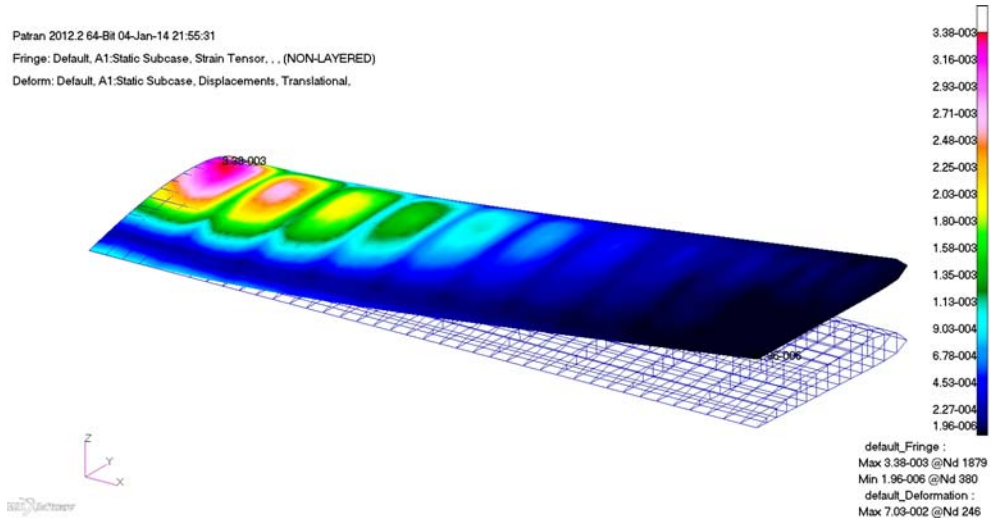

Figure 59: von Misses Strain Distribution over the Morphing Wing under the Aerodynamic Loading of the Take-off Configuration at Steady-Level Flight

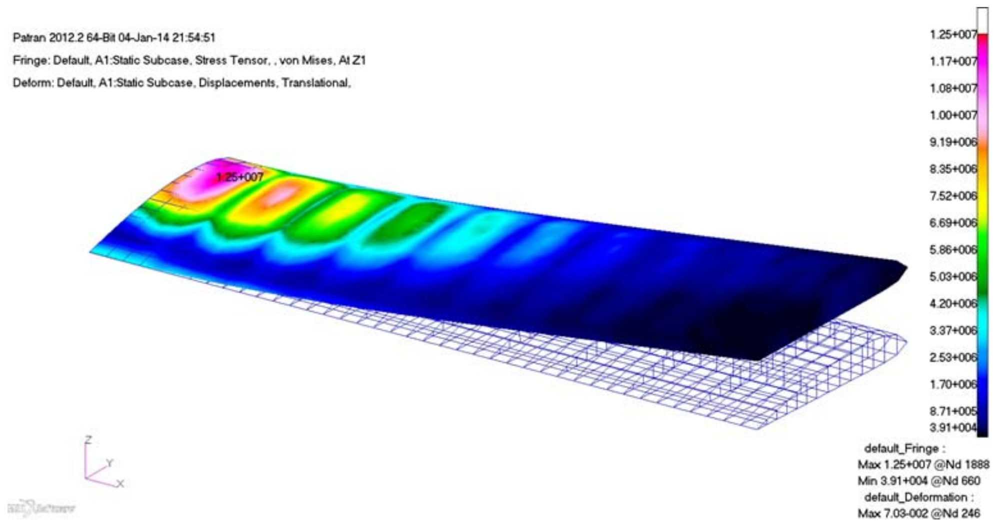

Figure 60: von Misses Stress Distribution over the Morphing Wing under the Aerodynamic Loading of the Take-off Configuration at Steady-Level Flight (Pa)

The maximum amount of stress computed in the analyses was 12.5 (MPa). This maximum stress value was reached at the upper skin of the morphing wing, for which the used material for production has an elastic failure value of 48 (MPa). In addition to this, the maximum strain value was found to be 0.00338, which could be regarded as a linear deformation. The analysis showed that there would be no possibility of failure due to the steady state loading of the morphing wings at take-off phase.

7.2.1.3 Stress-Strain Analysis of the Morphing Wing at the Climb Configuration

The climb motion is a steady flight condition, where there would be no acceleration, in most of the cases. The chordwise and the spanwise pressure distributions defined in Section 5.2.2 were combined together to approximate the aerodynamic loading over the wings at the climb phase. By direct application of the pressure distribution at the upper and lower surfaces of the right wing, the pressure contours were obtained as shown in Figure 61 and Figure 62 respectively.

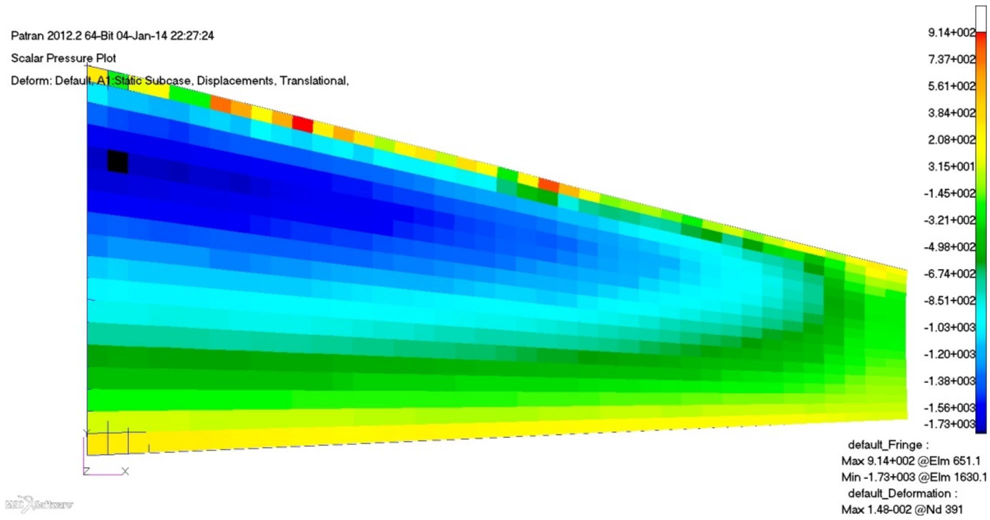

Figure 61: Pressure Distribution on the Upper Skin of the Morphing Wing at the Climb Configuration in Steady Flight (Pa)

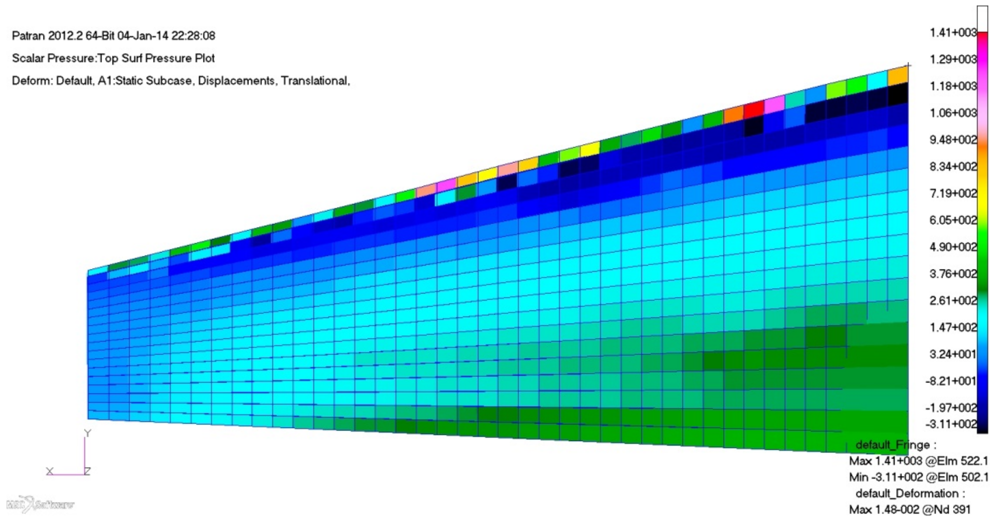

Figure 62: Pressure Distribution on the Lower Skin of the Morphing Wing at the Climb Configuration in Steady Flight (Pa)

After applying the proper pressure distribution over the wing, the linear static analysis was conducted. The displacement, strain and stress fields over the wings were obtained. The obtained results for the displacement, von Misses strain and stress fields are given in Figure 63 - Figure 65, respectively.

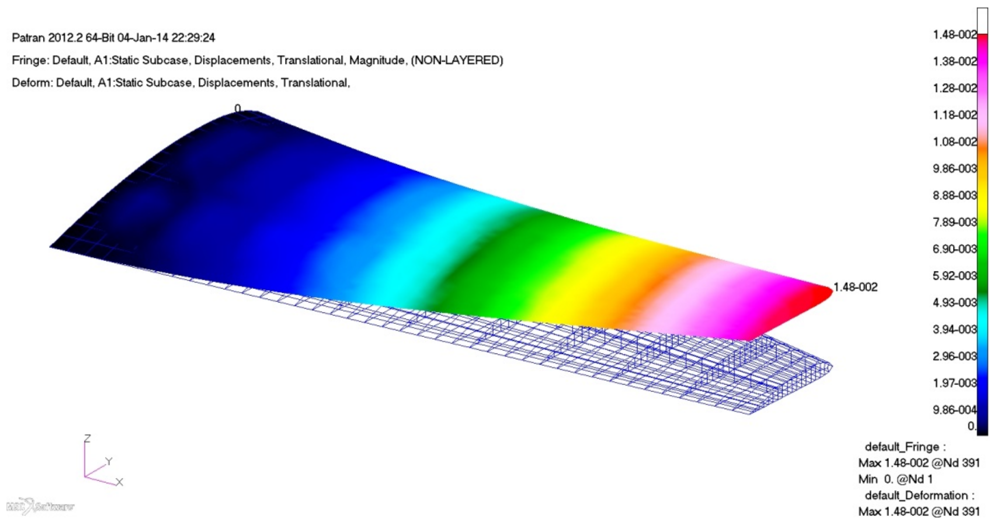

Figure 63: Displacement Field over the Morphing Wing under the Aerodynamic Loading of the Climb Configuration at Steady Flight (m)

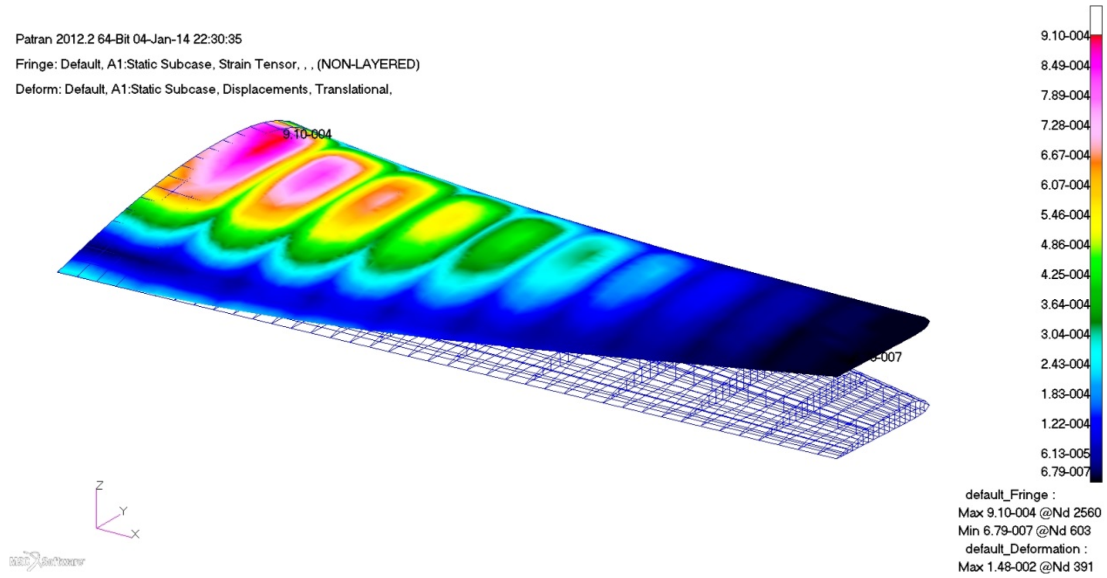

Figure 64: von Misses Strain Distribution over the Morphing Wing under the Aerodynamic Loading of the Climb Configuration at Steady Flight

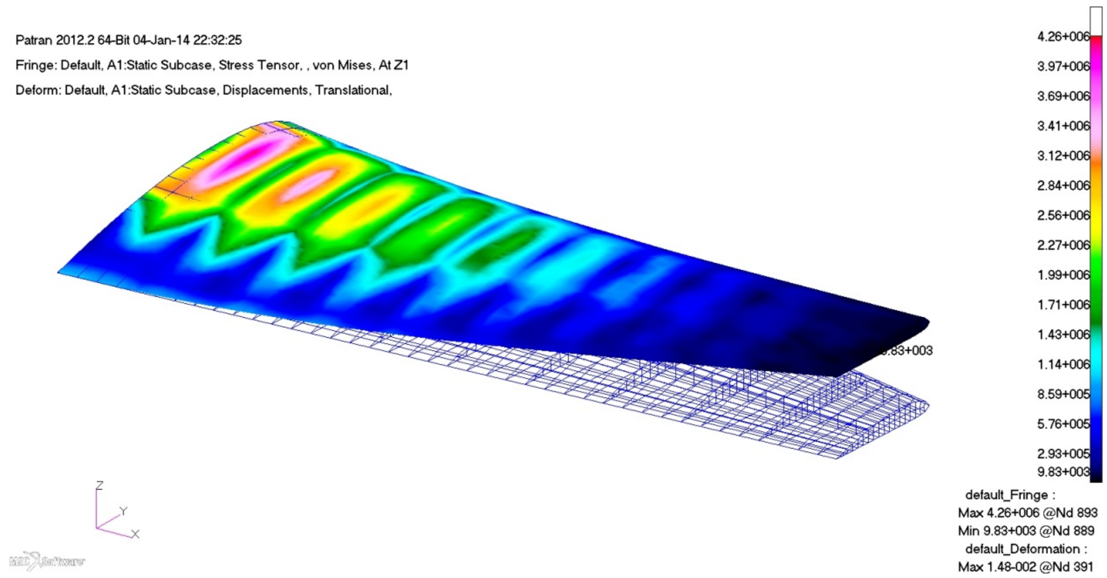

Figure 65: von Misses Stress Distribution over the Morphing Wing under the Aerodynamic Loading of the Climb Configuration at Steady Flight (Pa)

The maximum von Misses stress obtained in conducted analysis was 4.26 (MPa), which is very small compared to 48 (MPa) failure value of PA-1101 material used in the skin. If the structure was analyzed in terms of the deformation, the maximum strain value encountered was 0.00091, which would be treated as a linear behavior.

7.2.1.4 Stress-Strain Analysis of the Morphing Wing at the Cruise Configuration

The same procedure applied in the analyses corresponding to the other mission configurations were repeated for the cruise wing configuration. The chordwise and spanwise pressure distributions given in Section 5.2.3 were applied on the structural model by combining them as a three-dimensional pressure distribution. The pressure distributions over upper and lower surfaces of the morphing wing at cruise configuration are given in Figure 66 and Figure 67, respectively.

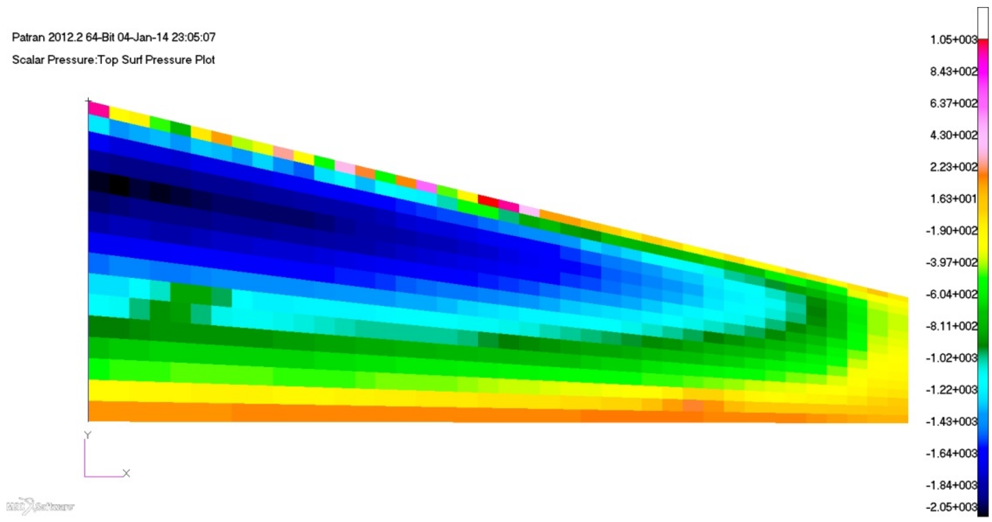

Figure 66: Pressure Distribution on the Upper Skin of the Morphing Wing at the Cruise Configuration in Steady-Level Flight (Pa)

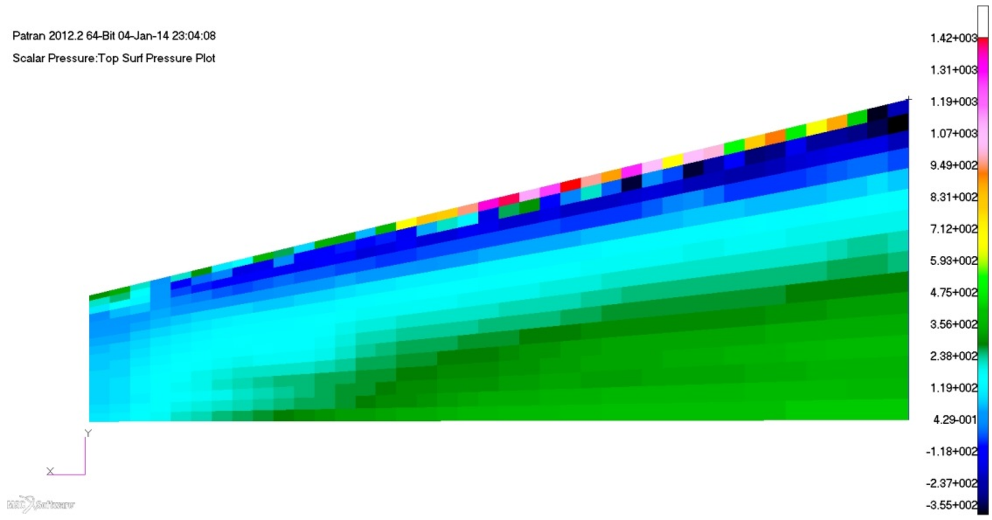

Figure 67: Pressure Distribution on the Lower Skin of the Morphing Wing at the Cruise Configuration in Steady-Level Flight (Pa)

Using the developed structural model, linear elastic analysis was conducted on the morphing wing at cruise configuration for a steady-level flight case. The fringe results of displacement, von Misses strain and stress distributions are given in Figure 68 - Figure 70, respectively.

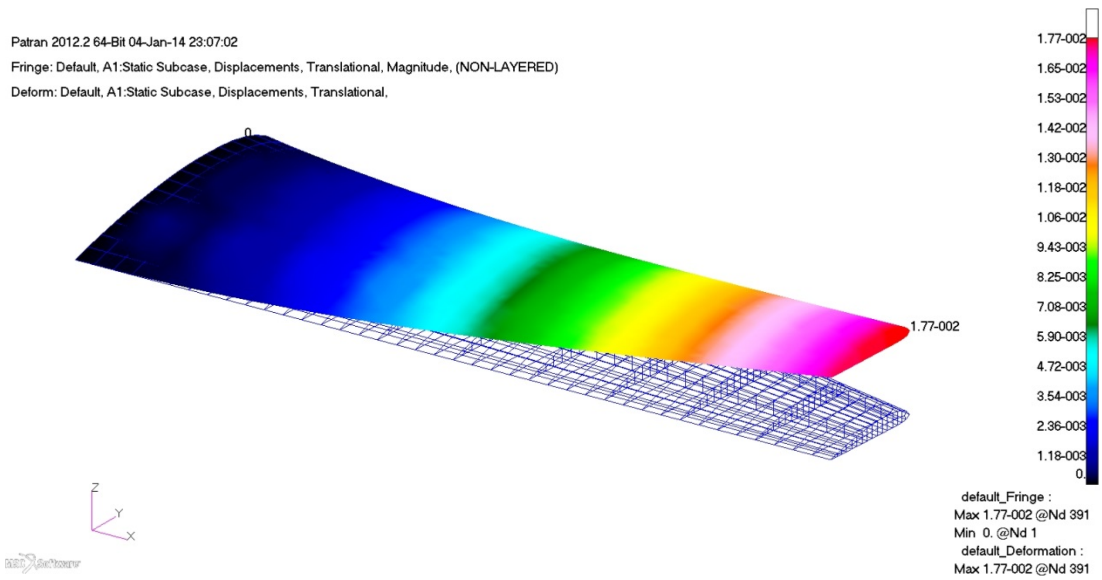

Figure 68: Displacement Field over the Morphing Wing under Aerodynamic Loading of the Cruise Configuration at Steady-Level Flight (m)

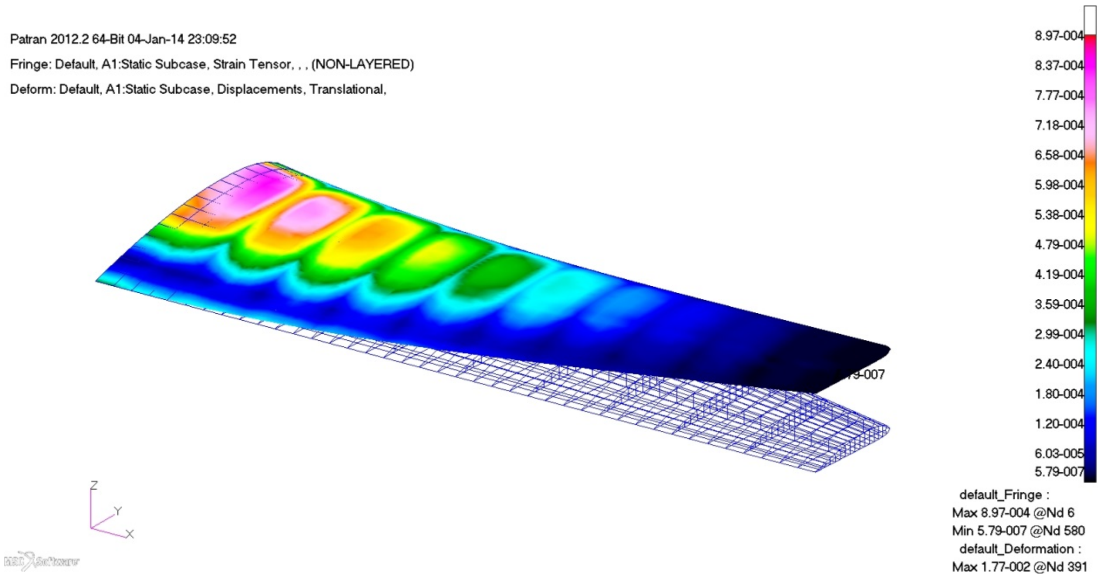

Figure 69: von Misses Strain Distribution over the Morphing Wing under Aerodynamic Loading of the Cruise Configuration at Steady-Level Flight

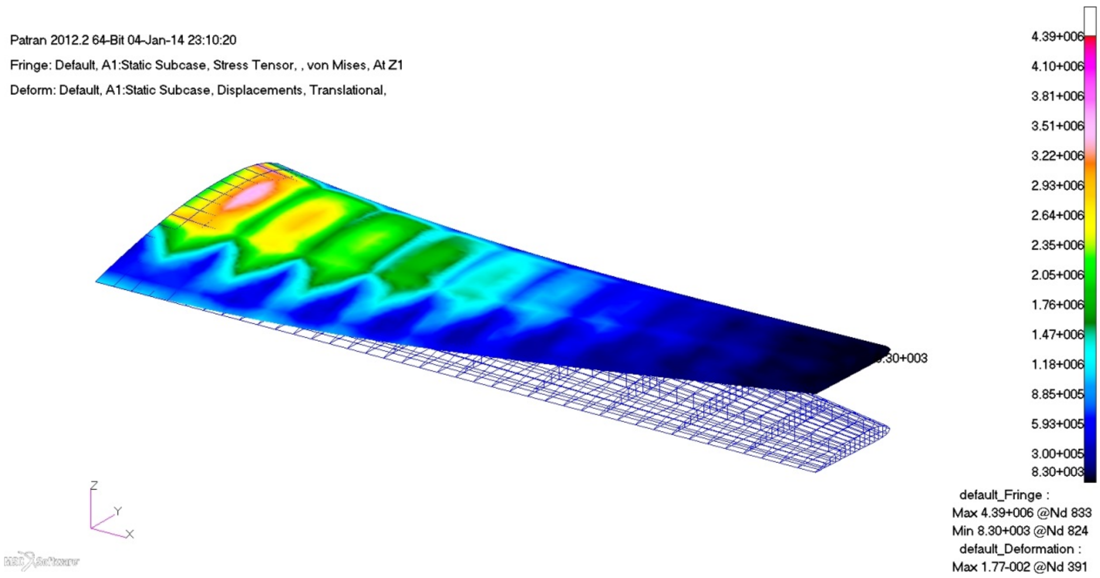

Figure 70: von Misses Stress Distribution over the Morphing Wing under Aerodynamic Loading of the Cruise Configuration at Steady-Level Flight (Pa)

The analysis showed that the aerodynamic loading at steady-level flight developed a maximum von Misses stress of 4.1 (MPa) on the upper skin of the morphing wing at cruise phase. This value is below the elastic failure value of the skin material PA-1101, which was given as 48 (MPa). In addition to this, the maximum strain achieved in the structure was 0.0008974, at which the structure remains in the linear elastic region.

7.2.1.5 Summary of the Linear Elastic Analyses

In order to understand the structural behavior of the morphing wings under static loading, a series of linear elastic analyses were conducted. During the analyses, a combination of the experimental chordwise pressure distributions for certain angles of attack and the spanwise pressure distribution based on Schrenk's method was used to simulate the aerodynamic loading over the wings. These pressure distributions were applied on the FE models developed for each phases of the flight regime. The analyses were conducted by using MSC/Nastran° finite element analyses software. The analyses showed that the wings can withstand the aerodynamic loads for steady flight conditions. In addition to the analyses conducted for steady flight conditions, a 4.5g maneuver at loitering phase was investigated. Again, it was realized that the wings can carry the required loading with a safety factor of approximately 1.5. These analyses verified that the wings, on which the aeroelastic analyses conducted, can accomplish the desired missions without permanent deformations or failure. The summary of results of the linear elastic analyses is given in Table 14.

Table 14: Summary of Results of the Linear Elastic Analyses Conducted on the Structural Models of the Morphing Wings

	Maximum von Misses Stress (MPa)	Maximum von Misses Strain ($x10^{-3}$)	Maximum Displacement (m)
Steady Level Flight Loading at the Take-off Configuration	12.5	3.38	0.07
Steady Level Flight Loading at the Climb Configuration	4.26	0.91	~0.02
Steady Level Flight Loading at the Cruise Configuration	4.39	0.90	~0.02
Steady Level Flight Loading at the Loiter Configuration	7.18	1.69	~0.06
4.5g Maneuver Loading at the Loiter Configuration	32.3	7.61	~0.26

7.2.2 Determination of the Structural Parameters for the Reduced Order Aeroelastic Model

Certain geometrical and structural parameters namely, mass moment of inertia, location of the elastic axis, weight and location of the center of gravity, and natural frequencies were required for the aeroelastic model of the morphing wings. The natural frequencies could only be determined by the in-vacuo dynamic analysis.

The rest of the required values were extracted from the output files of various linear elastic analyses.

For the construction of the reduced order aeroelastic model the chordwise location of the intersection point of the elastic axis with the cross-section of the wing at 75 percent of the half-span was required. In order to identify the location of that intersection, a series of analyses based on unit load method were conducted. A distributed unit load per unit span was applied on the wing starting from the leading edge of the wing structure. In each step, the load was transmitted to a parallel line of action with a distance of approximately 1 (inch). When the displacement at 75 percent of the half-span is purely translational with no twist, the chordwise location of the applied distributed force was assigned as the elastic axis intersection point.

When the fringe contour of the translational deformations was observed from the top view of the wing planform; it could be realized that when a rotation around spanwise axis was present, the fringe contours were not perpendicular to the spanwise axis. Whenever the contour at the 75 percent was perpendicular to the spanwise axis, the intersection of the line on which a distributed unit loading was applied and the cross-section at 75 percent was selected as the shear center of the reduced order aeroelastic model.

The procedure described was applied on each mission configuration of the morphing wings separately.

7.2.2.1 Locating the Shear Center and the Center of Gravity at the Loiter Configuration

In order to find the location of the shear center of the cross-section at 75 percent of the half-span, the necessary linear elastic analyses were conducted. Figure 71 shows a sample distributed loading used for this case study. Figure 72 and Figure 73 gives the fringe result for twisted deformation and untwisted deformation at 75 percent of the half-span respectively.

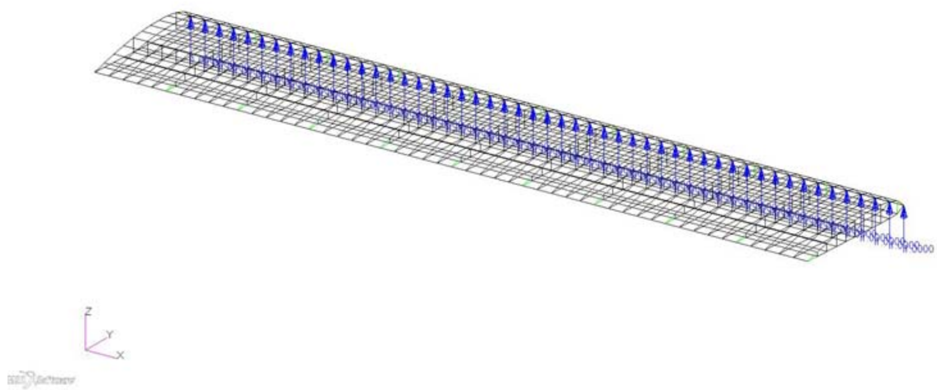

Figure 71: Distributed Unit Load per Unit Span Applied on the Wing Structure for the Identification of the Elastic Axis Intersection Location at the 75 percent of the Half-span

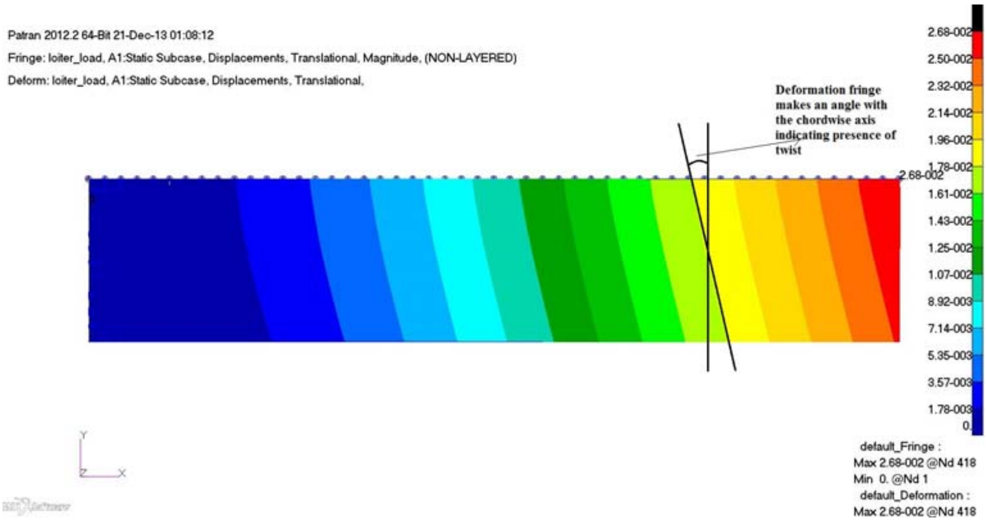

Figure 72: Presence of Twist in the Deformation Fringe when the Distributed Load is not applied on the Shear Center at the 75 Percent of the Half-span of the Wing

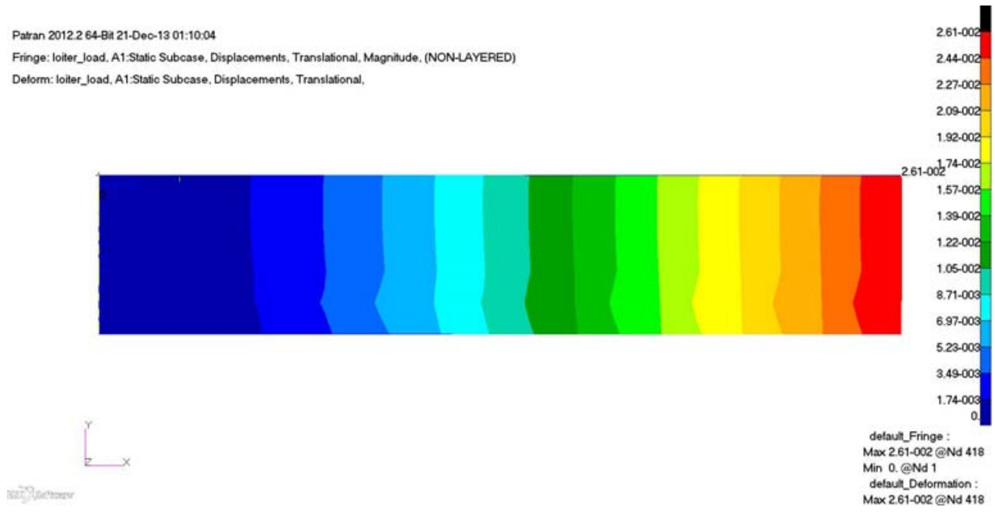

Figure 73: No Twist at 75 percent of the Half-Span Indicating the Location of the Sectional Shear Center under Pure Shear Loading for the Loiter Wing Configuration

The case study showed that the location of the intersection of the elastic axis and the cross-section of the wing at 75 percent of the half-span, which indeed was the sectional shear center, was located at 0.222 (m) from the leading edge. A summary of the geometrical and structural properties required for the reduced order aeroelastic model are tabulated in Table 15.

Table 15: Some Geometrical and Structural Properties of the Morphing Wing at the Loitering Configuration in SI Units

Location of the Elastic Axis at 75 percent of the Half-Span	-0.222 (m)
Chordwise Location of the Center of Gravity	-0.124 (m)
Mass Moment of Inertia about Spanwise Axis	0.675 (kg.m^2)
Mass Moment of Inertia about Elastic Axis	0.775 (kg.m^2)
Weight	4,08 (kgf)

7.2.2.2 Locating the Shear Center and the Center of Gravity at the Take-off Configuration

The same procedure was followed on the wing structural model corresponding to the take-off configuration, in order to determine the necessary parameters required for the construction of the reduced order aeroelastic model. The application of the unit distributed load resulted in a shear center location at the cross-section at 75 percent of the half-span measured from the leading edge as 0.366 (m). In Figure 74 the position of the shear center can be determined by the perpendicular fringe lines to the span when the distributed load was applied at 0.366 (m) behind the leading edge.

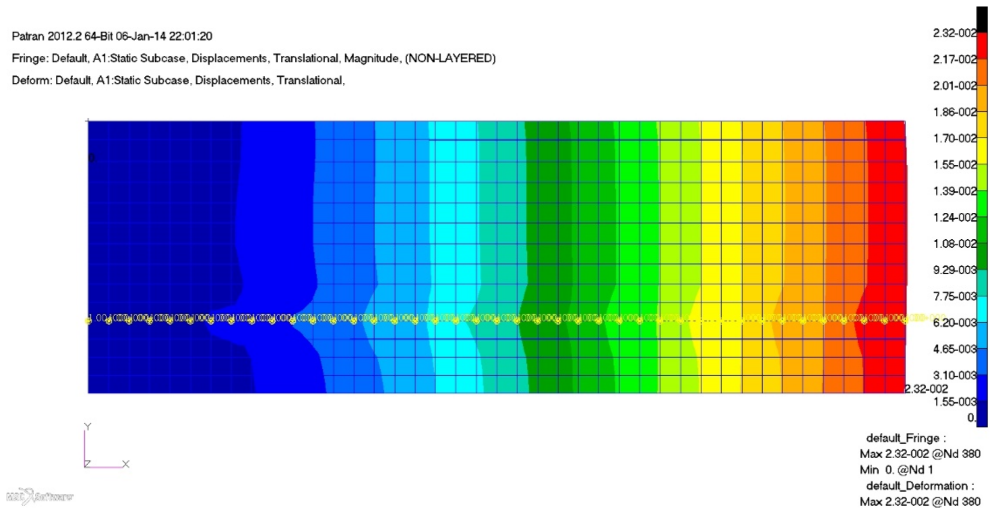

Figure 74: No Twist at 75 percent of the Half-Span Indicating the Location of the Sectional Shear Center under Pure Shear Loading for the Take-off Wing Configuration

During the analysis, the necessary data for the construction of the reduced order aeroelastic model was collected. The parameters were collected from the output of the FEA software. These parameters are listed in Table 16.

Table 16: Some Geometrical and Structural Properties of the Morphing Wing at the Take-off Configuration in SI Units

Location of the Elastic Axis at 75 percent of the Half-Span	-0.366 (m)
Chordwise Location of the Center of Gravity	-0.254 (m)
Mass Moment of Inertia about Spanwise Axis	0.884 (kg.m^2)
Mass Moment of Inertia about Elastic Axis	1.16 (kg.m^2)
Weight	4,08 (kgf)

7.2.2.3 Locating the Shear Center and the Center of Gravity at the Climb Configuration

The location of the shear center at the cross-section at 75 percent of the half-span, location of the center of gravity and the mass moment of inertia had to be determined in order to conduct flutter analysis on the climb wing configuration. In order to achieve this, the same methodology was followed. The fringe result on which the location of the shear center was approximated is shown in Figure 75.

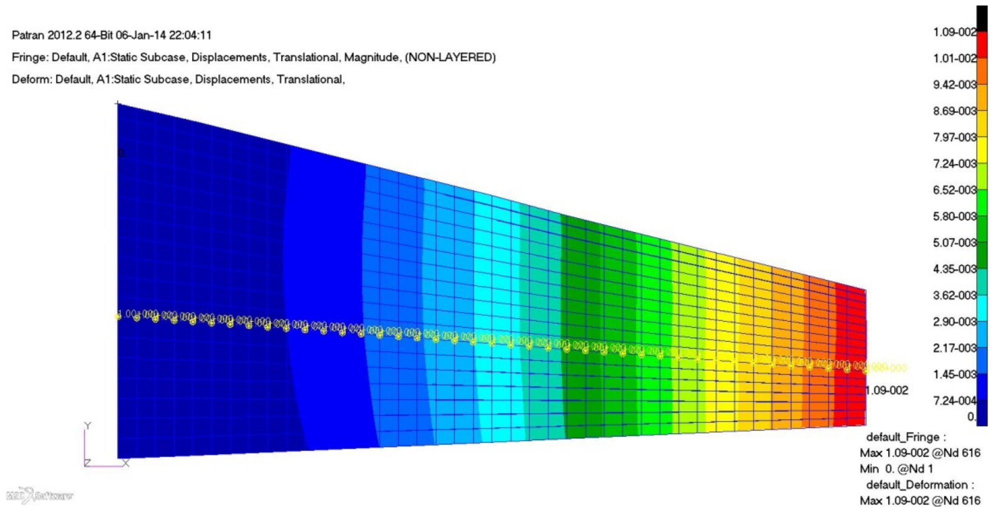

Figure 75: No Twist at 75 percent of the Half-Span Indicating the Location of the Sectional Shear Center under Pure Shear Loading for the Climb Wing Configuration

The necessary geometric and structural properties for the construction of the reduced order aeroelastic model of the wing at climb configuration were obtained by the conducted linear static analysis. These values are given in Table 17.

Table 17: Some Geometrical and Structural Properties of the Morphing Wing at the Climb Configuration in SI Units

Location of the Elastic Axis at 75 percent of the Half-Span	-0.848 (m)
Chordwise Location of the Center of Gravity	-0.331 (m)
Mass Moment of Inertia about Spanwise Axis	0.517 (kg.m^2)
Mass Moment of Inertia about Elastic Axis	0.853 (kg.m^2)
Weight	4,08 (kgf)

7.2.2.4 Locating the Shear Center and the Center of Gravity at the Cruise Configuration

By using the same method, the desired values of the location of the shear center, the location of the center of gravity and the mass moment of inertia was computed for the cruise configuration. In Figure 76 the no twist condition at 75 percent of the half-span was shown and in Table 18 the necessary parameters for the construction of the reduced order aeroelastic model were listed.

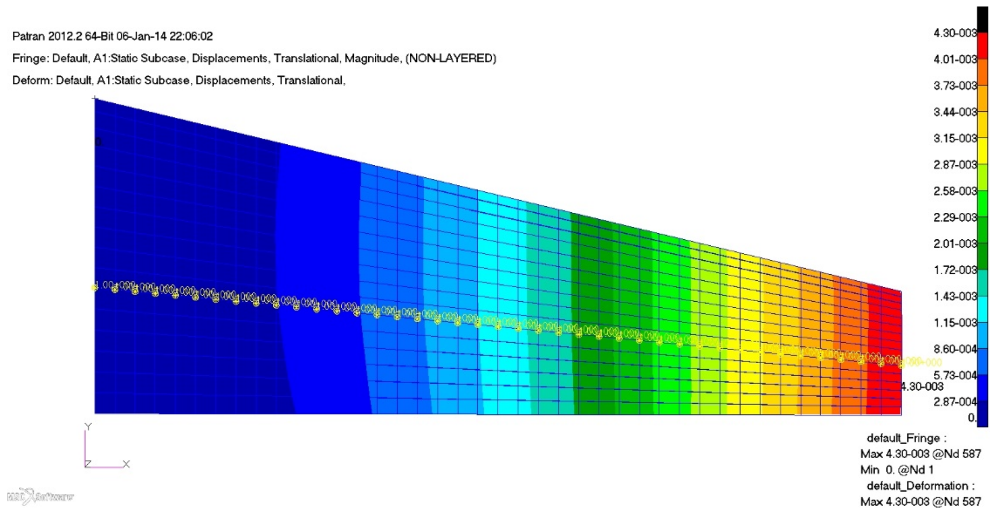

Figure 76: No Twist at 75 percent of the Half-Span Indicating the Location of the Sectional Shear Center under Pure Shear Loading for the Cruise Wing Configuration

Table 18: Some Geometrical and Structural Properties of the Morphing Wing at the Cruise Configuration in SI Units

Location of the Elastic Axis at 75 percent of the Half-Span	-0.739 (m)
Chordwise Location of the Center of Gravity	-0.283 (m)
Mass Moment of Inertia about Spanwise Axis	0.481 (kg.m^2)
Mass Moment of Inertia about Elastic Axis	0.745 (kg.m^2)
Weight	4,08 (kgf)

7.3 In Vacuo Dynamic Analyses of the Morphing Wings

The aim of in-vacuo dynamic analyses conducted was to determine the natural frequencies of the wing structure at various mission profiles. The results were used for the construction of the reduced order aeroelastic model. FE models used for the linear static analysis were also applicable for the natural frequency and mode shape analysis. The analyses were conducted for all configurations, take-off, climb, cruise and endurance. The frequency range selected during the analysis was 0-100 (Hz). The natural frequencies and the corresponding mode shapes of the wings at intended mission configurations are given accordingly.

7.3.1 Natural Frequencies and Mode Shapes of the Morphing Wings at the Take-off Configuration

The natural frequency and mode shape analysis was conducted on the FE model described in Section 6.2.3. The results of the analysis are tabulated for 0-100 (Hz) band in Table 19. The corresponding mode shapes are shown in Figure 77-Figure 80, in ascending order.

Table 19: The Natural Frequencies of the Morphing Wing at the Take-off Configuration

1st Out-of-plane Bending Mode	5.71 (Hz)
2nd Out-of-plane Bending Mode	31.41 (Hz)
1st In-plane Bending Mode	35.94 (Hz)
1st Torsional Mode	40.14 (Hz)

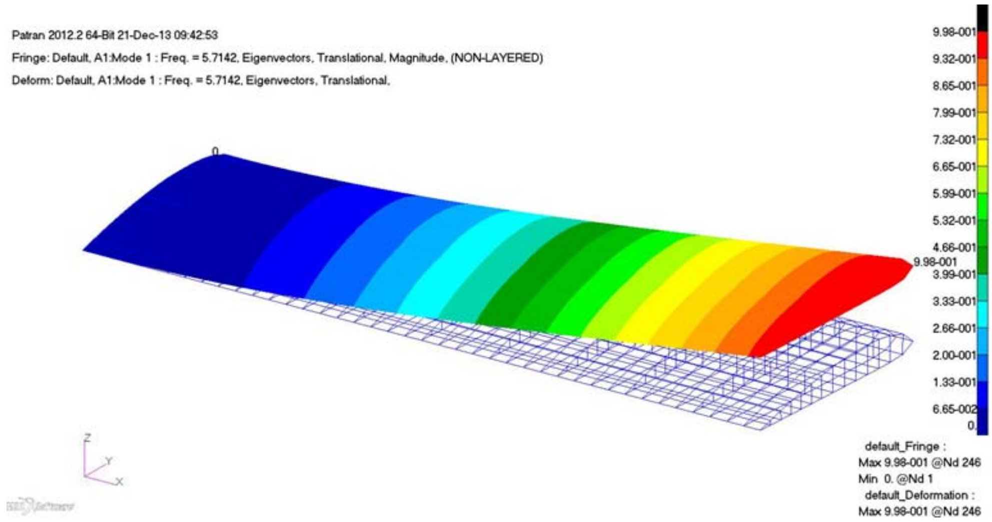

Figure 77: 1st Out-of-plane Bending Mode Shape of Morphing Wing at the Take-off Configuration (5.71 Hz)

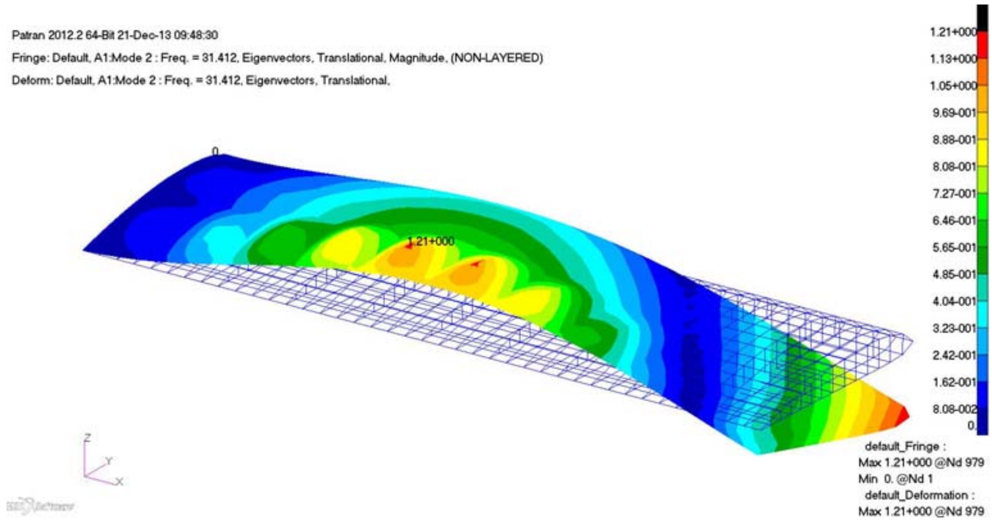

Figure 78: 2nd Out-of-plane Bending Mode Shape of Morphing Wing at the Take-off Configuration (31.41 Hz)

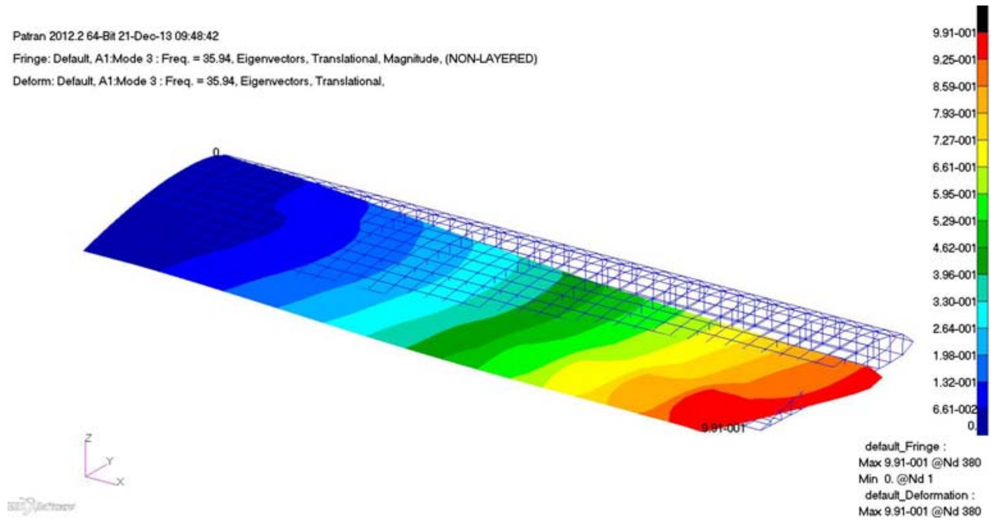

Figure 79: 1st In-plane Bending Mode Shape of Morphing Wing at the Take-off Configuration (35.94 Hz)

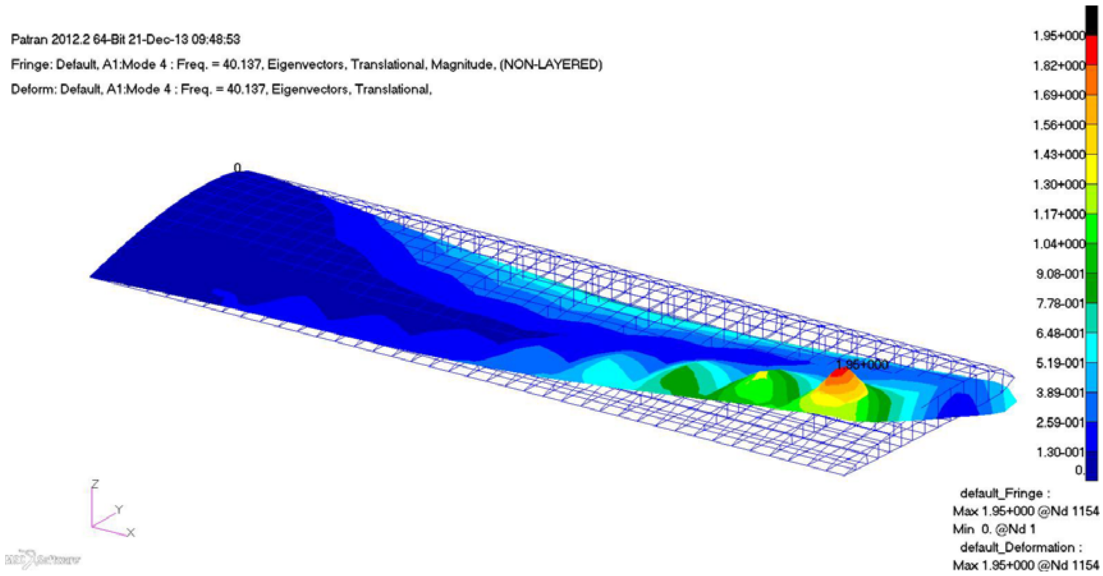

Figure 80: 1st Torsional Mode Shape of Morphing Wing at the Take-off Configuration (40.14 Hz)

In some of the mode shapes of the morphing wings, some locally large values of translations have been encountered. Figure 80 gives a typical example to this phenomenon. That was believed to be due to the very low local internal structure strength and that yielded very large displacements of the skin panels both inward and outward. These local instabilities in mode shapes do not have any influence on the reduced order aeroelastic models and the important modes are the 1st out-of-plane and 1st torsional modes.

7.3.2 Natural Frequencies and Mode Shapes of the Morphing Wings at the Climb Configuration

For the morphing wing in climb configuration, the natural frequencies and mode shapes were calculated by using the developed FE model shown in Section 6.2.4. Natural frequencies of the morphing wing within 0-100 (Hz) frequency band are given in Table 20. The corresponding mode shapes are shown between Figure 81 and Figure 84 in an ascending order.

Table 20: The Natural Frequencies of the Morphing Wing at the Climb Configuration

1st Out-of-plane Bending Mode	12.71 (Hz)
2nd Out-of-plane Bending Mode	49.51 (Hz)
1st In-plane Bending Mode	68.88 (Hz)
1st Torsional Mode	82.61 (Hz)

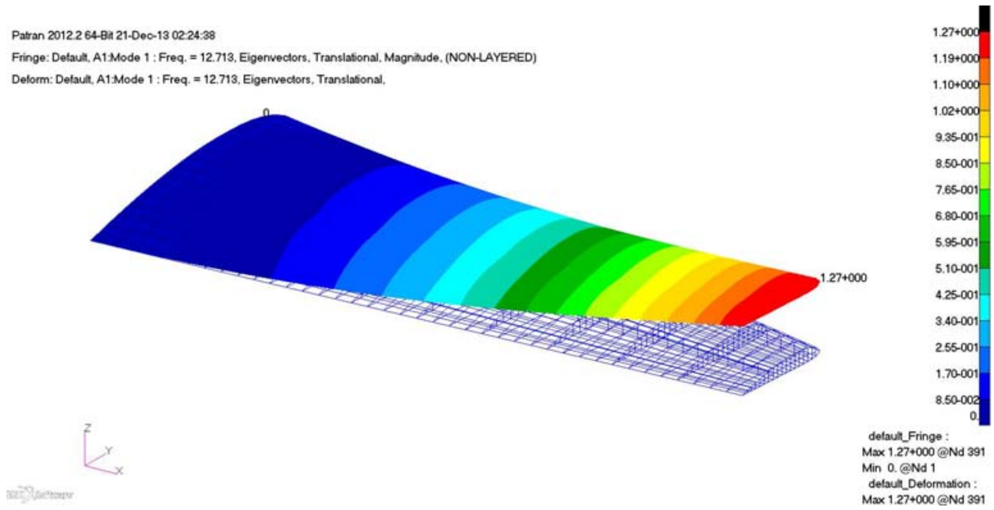

Figure 81: 1st Out-of-plane Bending Mode Shape of Morphing Wing at the Climb Configuration (12.71 Hz)

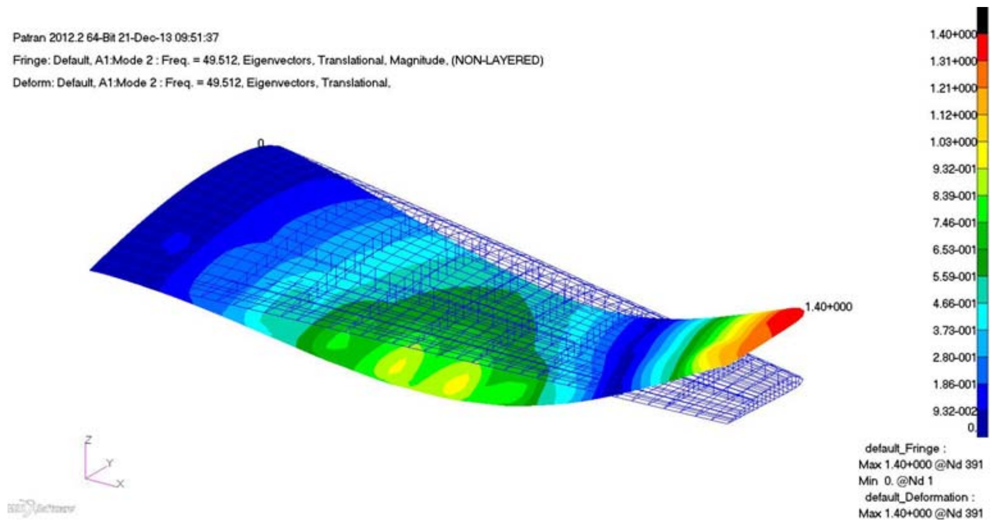

Figure 82: 2nd Out-of-plane Bending Mode Shape of Morphing Wing at the Climb Configuration (49.51 Hz)

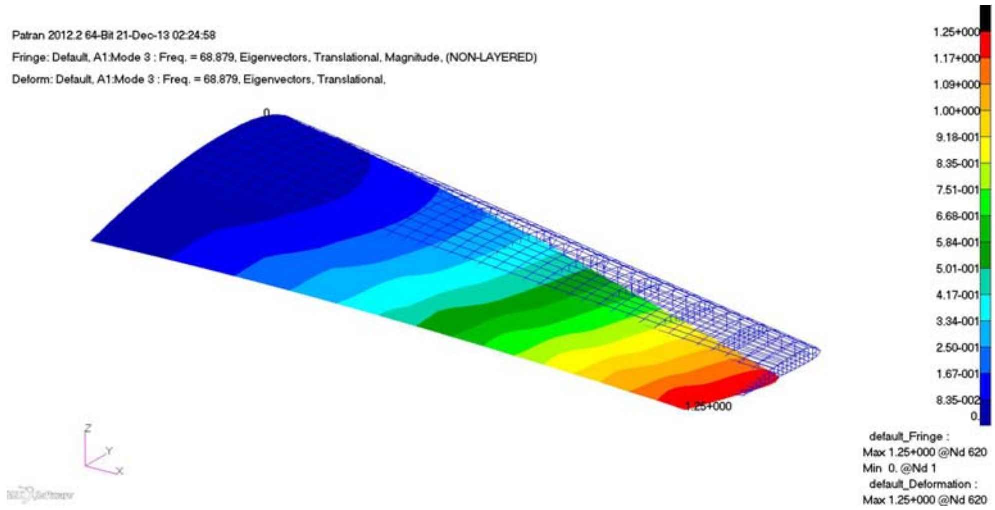

Figure 83: 1st In-plane Bending Mode Shape of Morphing Wing at the Climb Configuration (68.88 Hz)

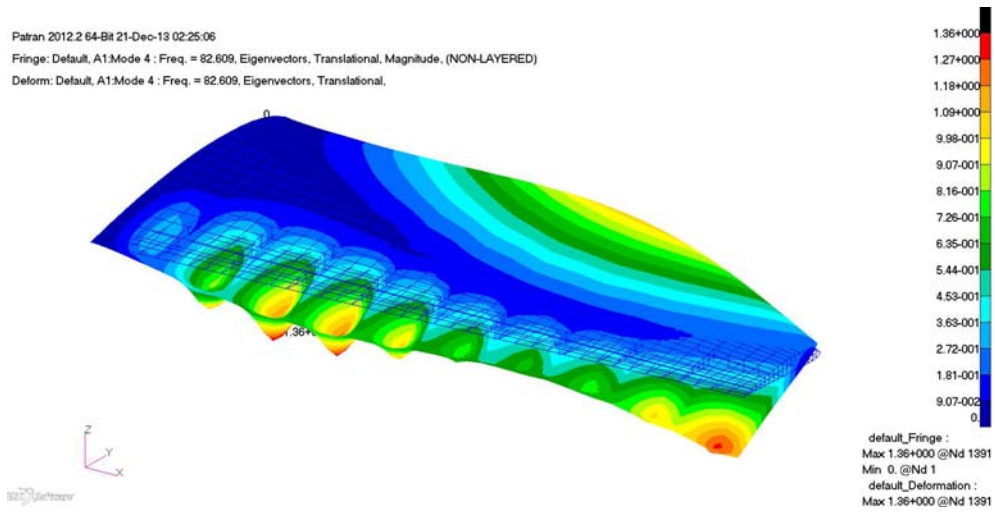

Figure 84: 1st Torsional Mode Shape of Morphing Wing at the Climb Configuration (82.61 Hz)

7.3.3 Natural Frequencies and Mode Shapes of the Morphing Wings at the Cruise Configuration

Normal modes analysis was repeated for the cruise configuration of the morphing wings. The results of the natural frequencies in 0-100 Hz band are listed in Table 21. The mode shapes corresponding to these natural frequencies are shown in Figure 85-Figure 89.

Table 21: The Natural Frequencies of the Morphing Wing at the Cruise Configuration

1st Out-of-plane Bending Mode	11.53 (Hz)
2nd Out-of-plane Bending Mode	46.75 (Hz)
1st In-plane Bending Mode	54.04 (Hz)
1st Torsion Dominated Torsion-Bending Mode	86.77 (Hz)
1st Torsion Influenced Out-of-plane Bending Mode	95.51 (Hz)

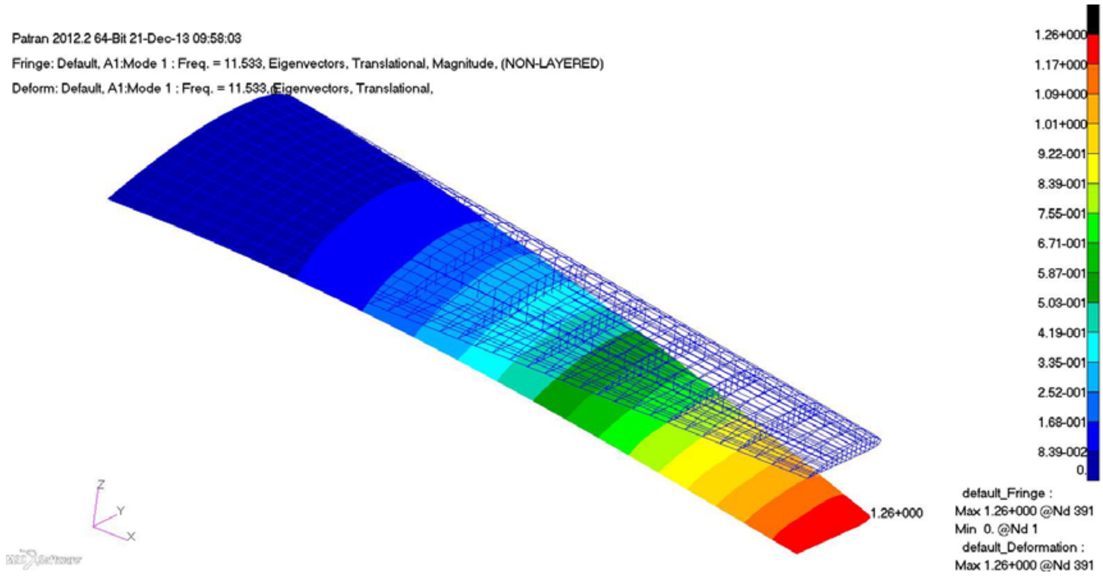

Figure 85: 1st Out-of-plane Bending Mode Shape of Morphing Wing at the Cruise Configuration (11.53 Hz)

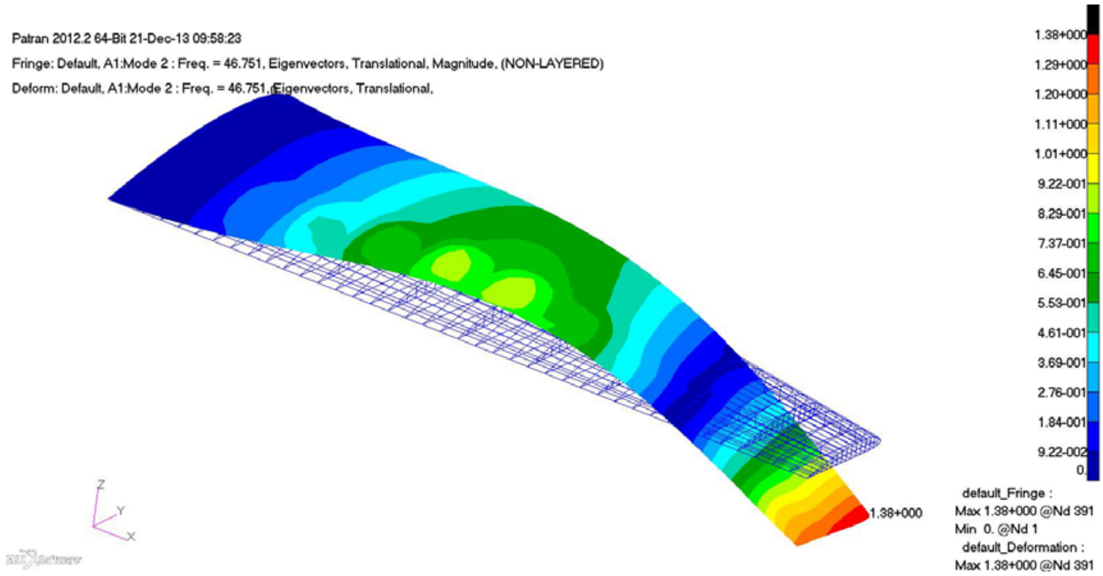

Figure 86: 2nd Out-of-plane Bending Mode Shape of Morphing Wing at the Cruise Configuration (46.75 Hz)

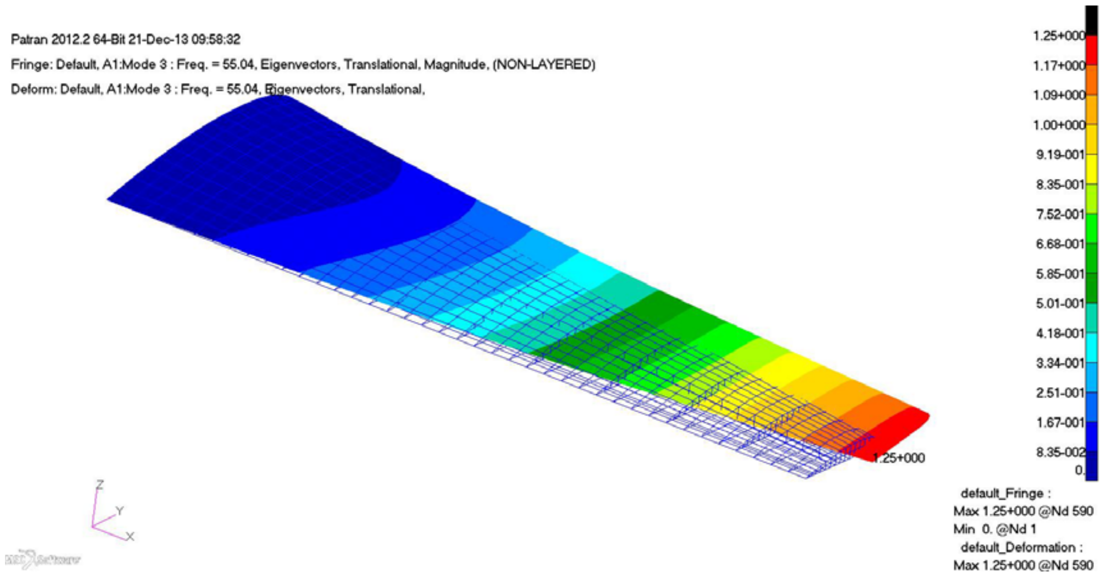

Figure 87: 1st In-plane Bending Mode Shape of Morphing Wing at the Cruise Configuration (55.04 Hz)

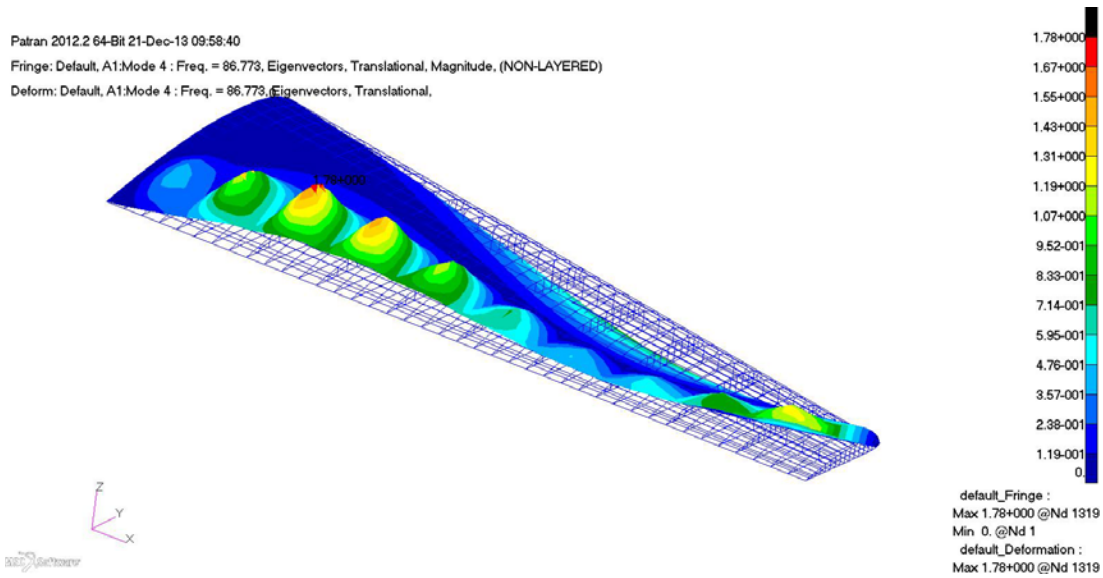

Figure 88: 1st Torsion Dominated Torsion-Bending Mode Shape of Morphing Wing at the Cruise Configuration (86.77 Hz)

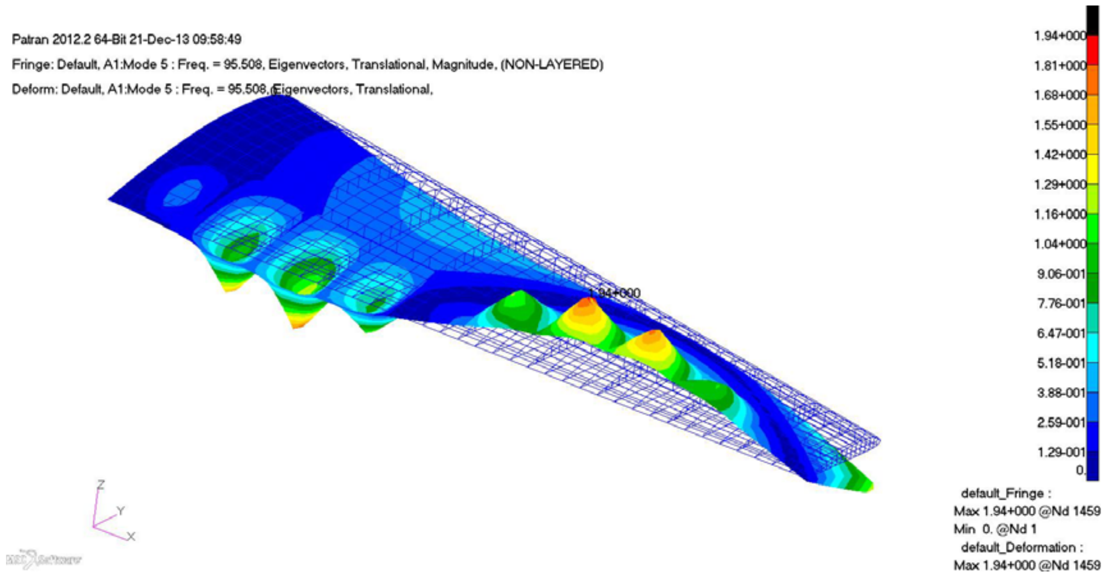

Figure 89: 1st Torsion Influenced Out-of-plane Bending Mode Shape of Morphing Wing at the Cruise Configuration (95.51 Hz)

7.3.4 Natural Frequencies and Mode Shapes of the Morphing Wings at the Loiter Configuration

The last configuration of the morphing wing geometry, on which the natural frequency and mode shape analysis was conducted, was loiter configuration. The FE model developed and shown in Section 6.2.6 was used during the analysis. The natural frequencies fall in between 0 and 100 (Hz) were calculated. The results are tabulated in Table 22. The corresponding mode shapes for the natural frequencies are shown in ascending order in Figure 90-Figure 94.

Table 22: The Natural Frequencies of the Morphing Wing at the Loiter Configuration

1st Out-of-plane Bending Mode	4.40 (Hz)
2nd Out-of-plane Bending Mode	20.40 (Hz)
1st In-plane Bending Mode	26.51 (Hz)
1st Torsional Mode	54.40 (Hz)
3rd Out-of-plane Bending	68.03 (Hz)

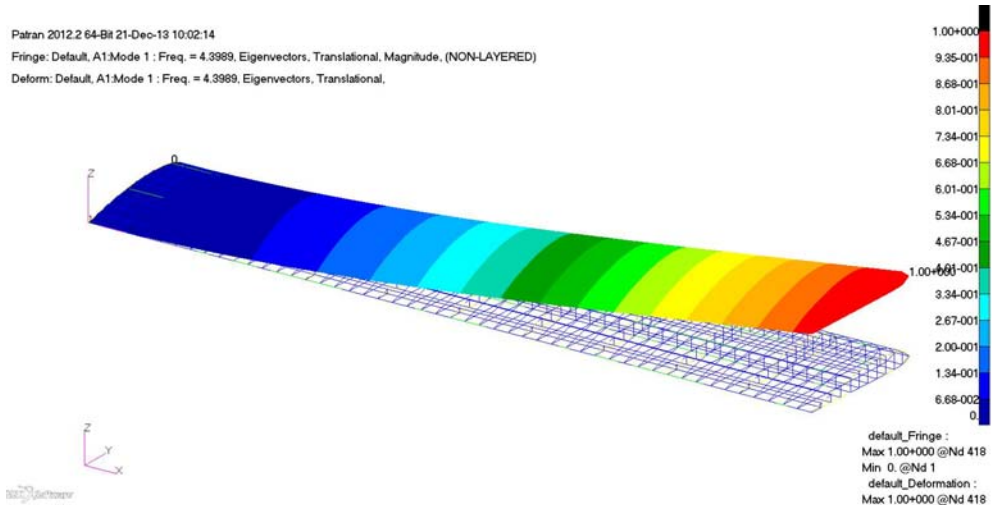

Figure 90: 1st Out-of-plane Bending Mode Shape of Morphing Wing at the Loiter Configuration (4.40 Hz)

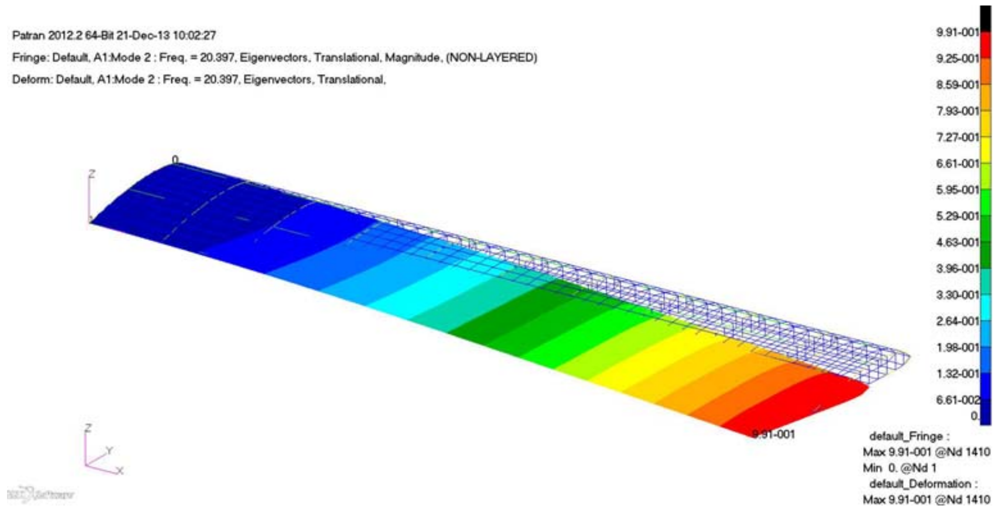

Figure 91: 1st In-plane Bending Mode Shape of Morphing Wing at the Loiter Configuration (20.40 Hz)

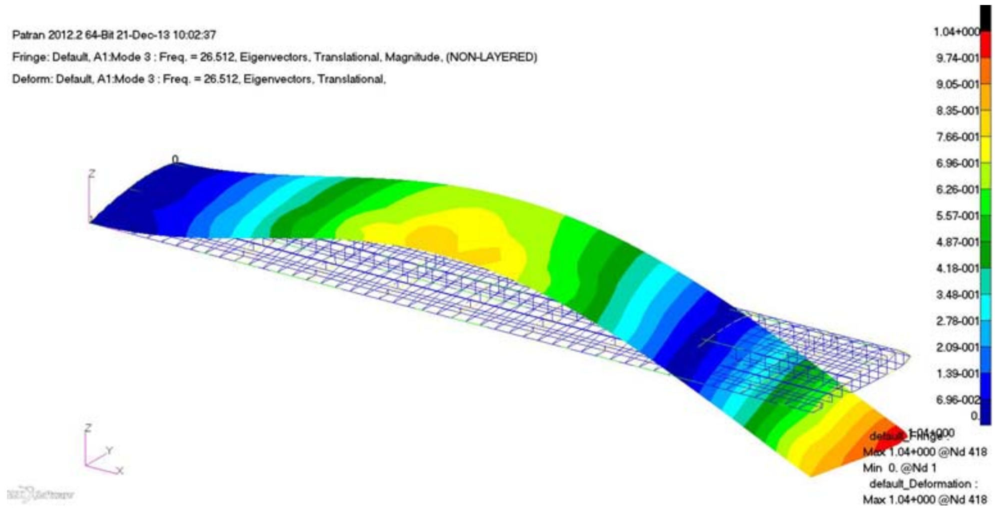

Figure 92: 2nd Out-of-plane Bending Mode Shape of Morphing Wing at the Loiter Configuration (26.51 Hz)

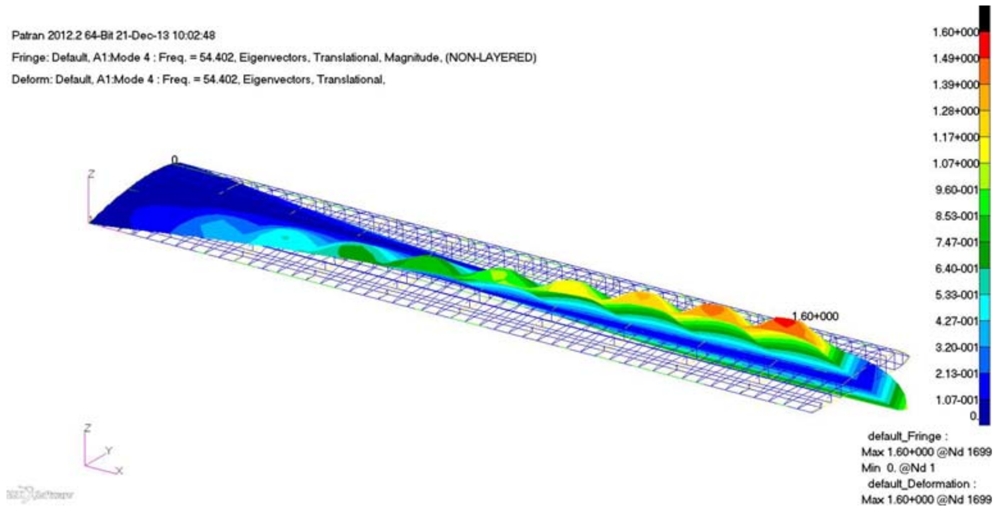

Figure 93: 1st Torsion Mode Shape of Morphing Wing at the Loiter Configuration (54.40 Hz)

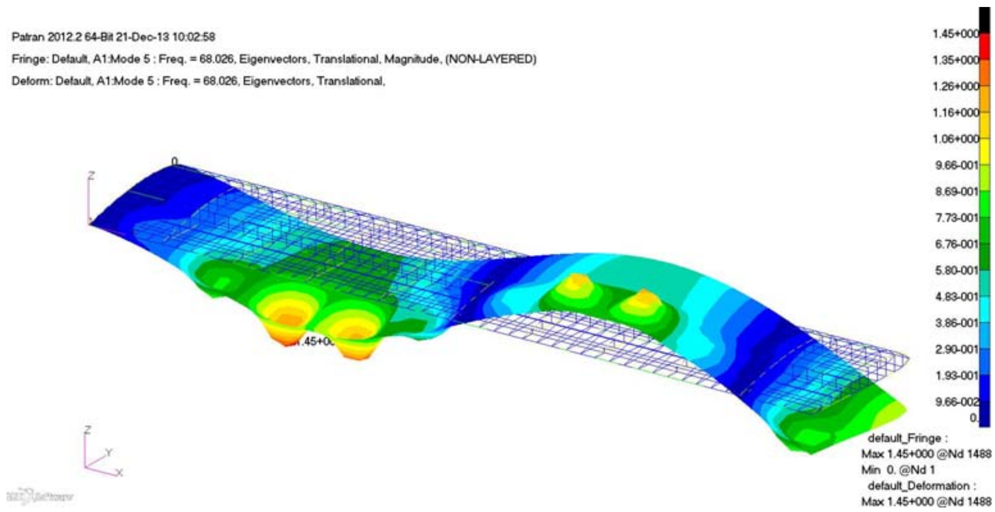

Figure 94: 3rd Out-of-plane Bending Mode Shape of Morphing Wing at the Loiter Configuration (68.03 Hz)

7.3.5 Summary of the Results of In-Vacuo Dynamic Analyses

The natural frequencies and mode-shapes presented here gives a possibility to compare the in-vacuo dynamic behavior of the four different morphing phases studied in this thesis. The aeroelastically important modes are the first bending and first torsional mode shapes. It will be convenient to state here that the torsion dominated mode shapes of some cases were also considered as the first torsional mode, since there are no more similar behavior. Out-of-plane bending modes, which will be expected to couple with the torsional modes are considered as the bending modes in short.

When the two modes described in the previous paragraph are compared among the four flight configurations, the difference between the dynamic behaviors can be understood. The dynamic behavior between the mission configurations is considered to be drastically changing. These changes should influence the design phase of the morphing wings, since there are more modes to be avoided or suppressed. The values of the two modes for each mission are tabulated together to give a perspective to this issue in Table 23.

Table 23: Comparison of the In-vacuo Dynamic Behavior among the Wing Configurations at Four Flight Phases

Flight Phase	Bending Mode	Torsional Mode
Take-off	5.71 (Hz)	40.14 (Hz)
Climb	12.71 (Hz)	82.61 (Hz)
Cruise	11.53 (Hz)	86.77 (Hz)
Loiter	4.40 (Hz)	54.40 (Hz)

7.4 Discussion and Conclusion

In this chapter, a series of finite element analyses were conducted by using MSC/Nastran® commercial software for which the finite element models were developed using MSC/Patran® commercial software. The main purpose of the analyses was to shed a light, if possible, to the effect of morphing on the predicted flutter speed of the wings.

The necessary information for the aeroelastic analysis was also extracted from FEA. The location of the center of gravity of the wing, location of the elastic axis on 75 percent of the half-span, radius of gyration, second moment of area and weight were gathered information from FEA for the construction of the reduced order flutter model.

The values obtained in this chapter would be used for further analysis of the morphing structure.

CHAPTER 8

AEROELASTIC ANALYSES OF THE MORPHING WINGS

8.1 Introduction

Aeroelastic behavior of the wings has very significant effects on the flight performance. This became more significant by using morphing wings on a UAV, since the structural characteristics of the system deviates significantly. Hence, every phase of the flight should also be treated separately in terms of the aeroelastic behavior.

Having the highest importance among all aero-structural instabilities and being the most catastrophic one; the flutter will be the main focus in this chapter. The flutter solution in this thesis was based on a reduced order aeroelastic model described in Section 2.2, in detail. Two different methods were used for the flutter solution; k-method and p-k method, which were also described in Section 2.4 of this manuscript.

The flutter analyses in this chapter were conducted on two degrees of freedom and three degrees of freedom models. Two degrees of freedom models were used for the identification of the characteristics of the wing structure alone. In the three degrees of freedom model, an adaptive camber aileron was installed on the morphing wing.

The analyses were conducted on all phases of the flight; take-off, climb, cruise and loiter. The results obtained by two different methods for all cases will be compared to identify the effects of shape change on the flutter behavior of the morphing structures, which was the main focus in this thesis.

In order to conduct the analyses an in-house developed code was used. The code was based on two methods, k-method and p-k methods. MATLAB® language was used for the program developed.

8.2 Linear Aeroelastic Solutions of the Morphing Wings

Linear aeroelastic analyses were conducted on both two-degrees-of-freedom and three-degrees-of-freedom models. The results would be given in this section under relevant subsections.

8.2.1 Aeroelastic Solutions of the Morphing wings by Using Two-Degrees-of-Freedom Model

Two-degrees-of-freedom version of the reduced order aeroelastic model consisted of plunge stiffness and pitch stiffness of the wing structures with the wing mass and the mass moment of inertia properties. The geometric quantities extracted from FEA results were also used in the solution. Both k-method and pk-method, which were described in detail in Section 2.3, were used for the solution of the two-degrees-of-freedom system.

8.2.1.1 Two-Degrees-of-Freedom Aeroelastic Analysis of the Morphing Wings for Take-off Configuration

The in-house developed computer program computed the flutter speed for the take-off configuration without any control surfaces as 122.2 (ft/s) by using k-method and 122.3 (ft/s) by using p-k method respectively. The flutter was detected at the torsional aeroelastic mode. However, while it could not be detected by k-method due to its limitations, p-k method detected a divergence, which is a static aeroelastic phenomenon, before the flutter speed. At a speed of 70.95 (ft/s) the wing diverges in bending deformation mode. In the p-k method, if any of the modes frequency value decreases to zero, in other words, the imaginary part of the corresponding eigenvalue goes to zero, divergence should be predicted [38]. The respective plots of the analyses for both methods are given in Figure 95-Figure 98.

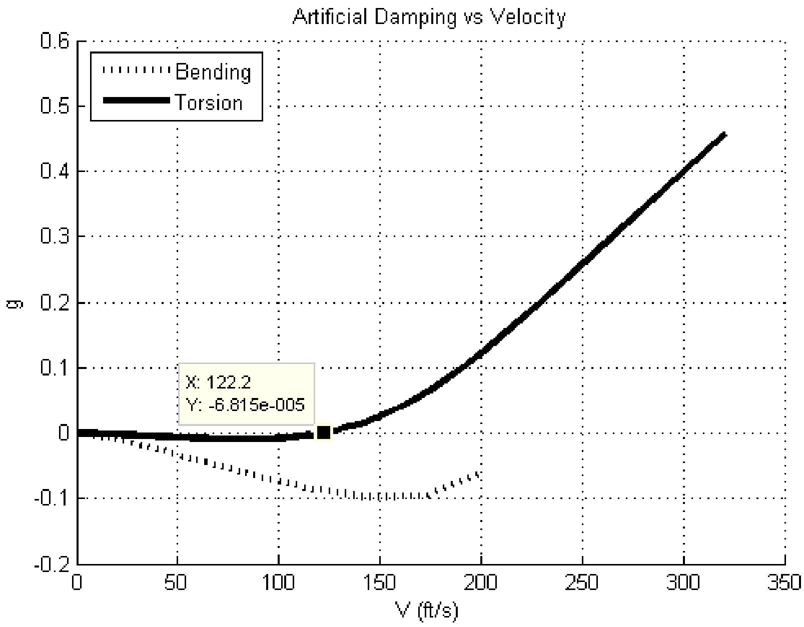

Figure 95: Damping vs. Velocity Plot of Modes of the Take-off Wing Configuration by using k-method in Two-Degrees-of-Freedom

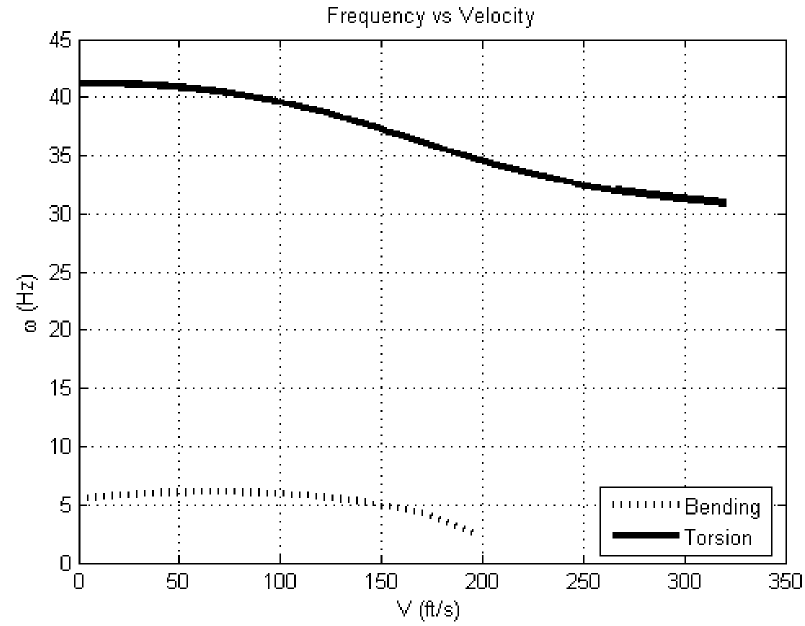

Figure 96: Frequency vs. Velocity Plot of Modes of the Take-off Wing Configuration by using k-method in Two-Degrees-of-Freedom

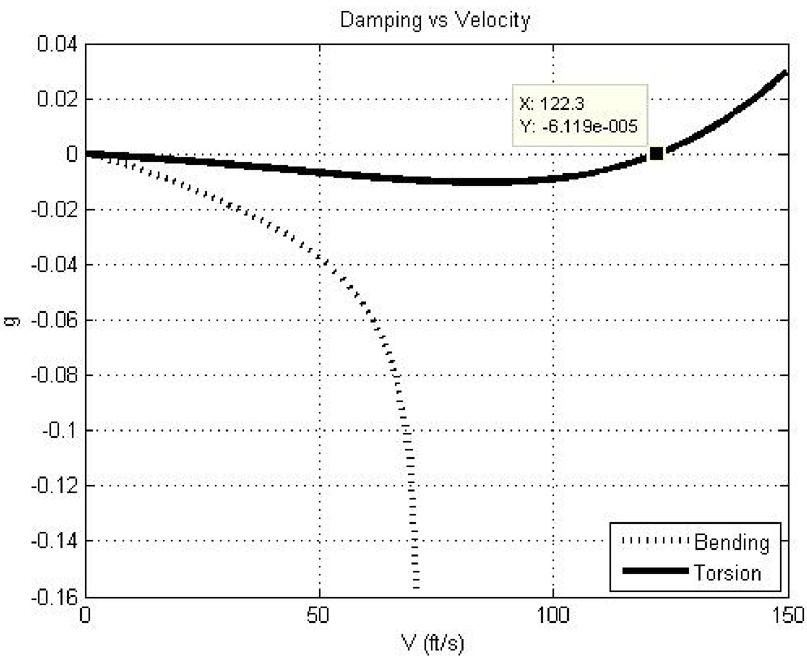

Figure 97: Damping vs. Velocity Plot of Modes of the Take-off Wing Configuration by using pk-method in Two-Degrees-of-Freedom

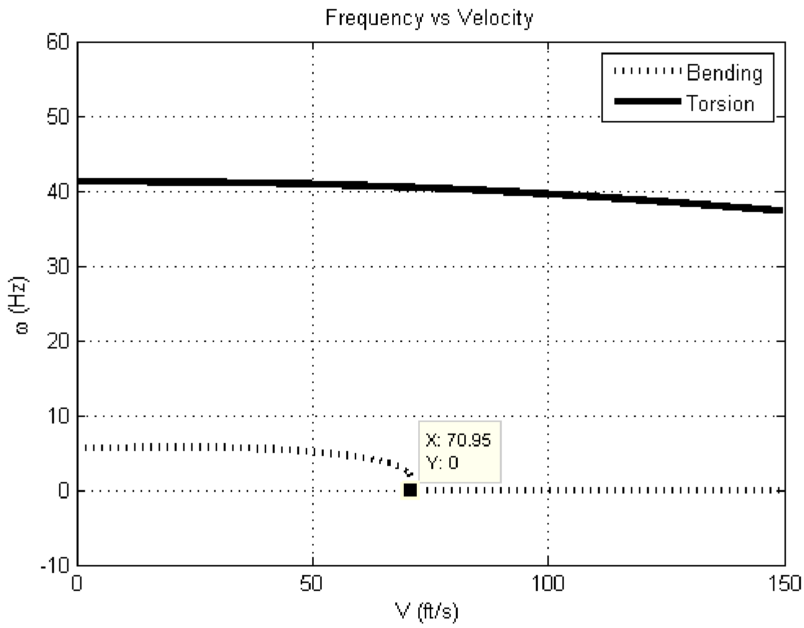

Figure 98: Frequency vs. Velocity Plot of Modes of the Take-off Wing Configuration by using pk-method in Two-Degrees-of-Freedom

8.2.1.2 Two-Degrees-of-Freedom Aeroelastic Analysis of the Morphing Wings for the Climb Configuration

Identical two-degrees-of-freedom system analyses were conducted on the climb configuration of the morphing wings. The results showed a rare phenomenon; the speed at which torsional mode flutters, bending mode diverges. This has been a desired condition, since in either condition there would be a failure in the structure, collecting the two phenomena at single speed would make it possible avoiding or suppressing both of them at the same time.

After conducting the required analyses, the flutter speed was found as 257.1 (ft/s) with k-method and 257.4 (ft/s) with the pk-method. The divergence speed obtained by pk-method was 257.9 (ft/s). The plots of the damping and frequency terms with respect to speed are given in Figure 99-Figure 102.

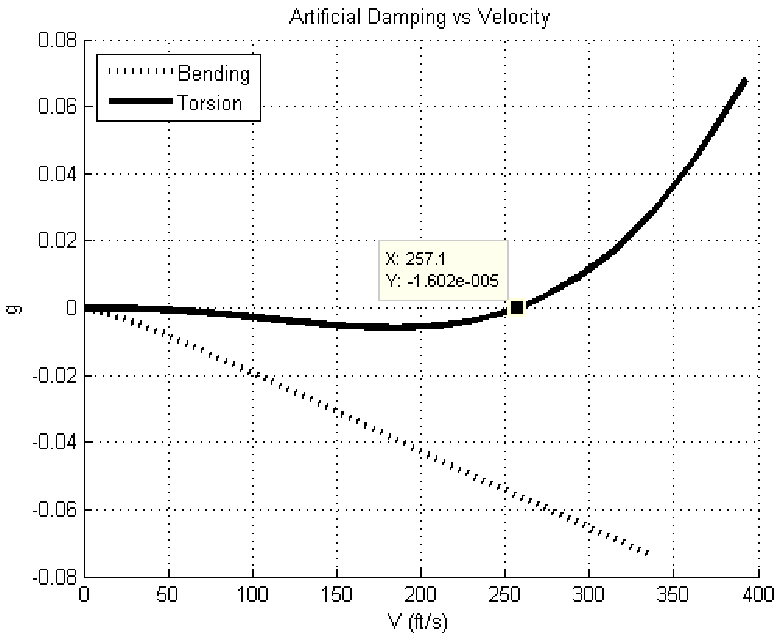

Figure 99: Damping vs. Velocity Plot of Modes of the Climb Wing Configuration by using k-method in Two-Degrees-of-Freedom

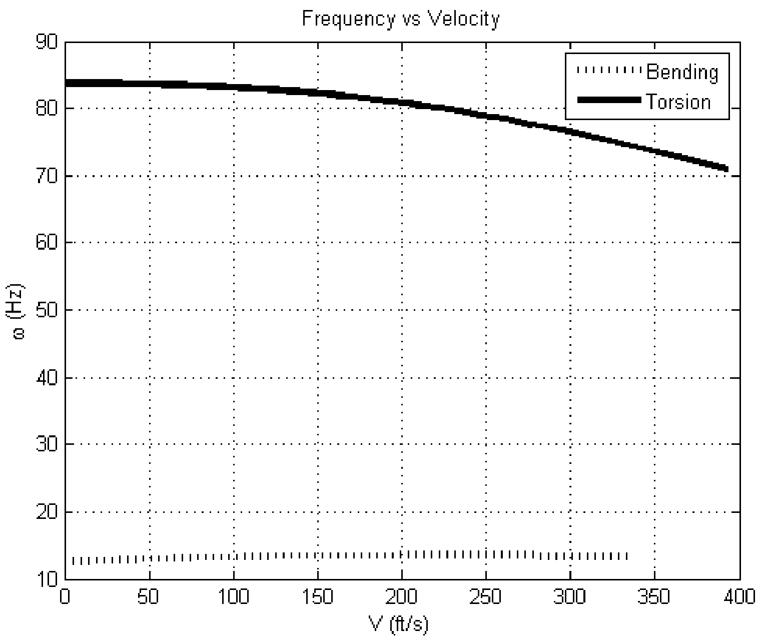

Figure 100: Frequency vs. Velocity Plot of Modes of the Climb Wing Configuration by using k-method in Two-Degrees-of-Freedom

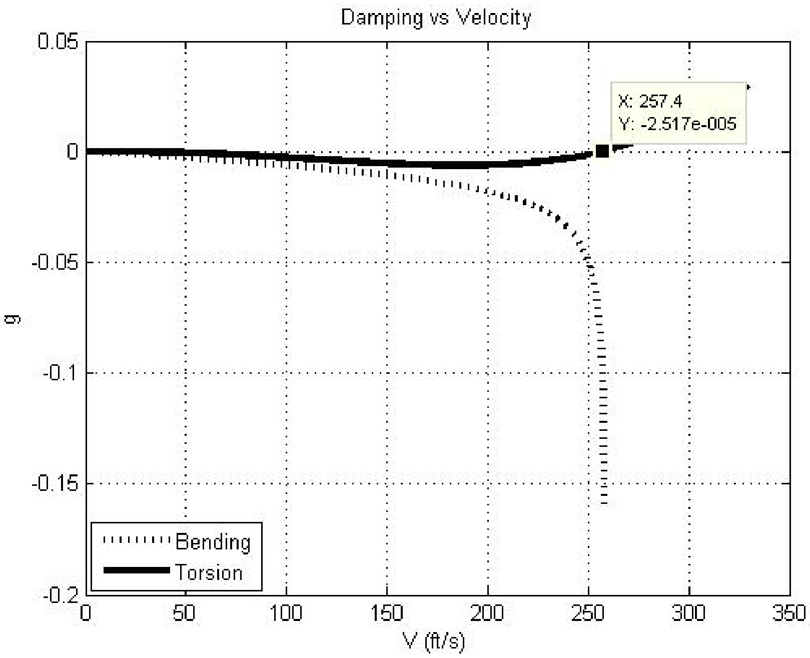

Figure 101: Damping vs. Velocity Plot of Modes of the Climb Wing Configuration by using pk-method in Two-Degrees-of-Freedom

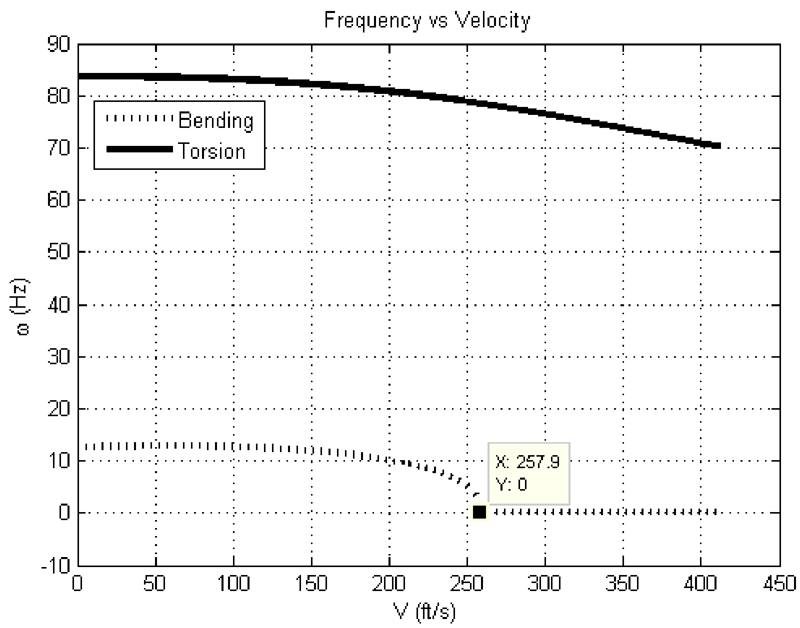

Figure 102: Frequency vs. Velocity Plot of Modes of the Climb Wing Configuration by using pk-method in Two-Degrees-of-Freedom

8.2.1.3 Two-Degrees-of-Freedom Aeroelastic Analysis of the Morphing Wings for the Cruise Configuration

The aeroelastic analyses by using a two-degrees-of-freedom model were also repeated for the climb configuration of the morphing wings. The analyses showed that the highest flutter speed of all the flight regimes was achieved at the cruise configuration. Since the morphing wings had the smallest planform area and the lowest aspect ratio at the cruise configuration, this was an expected outcome.

289.7 (ft/s) was the flutter speed value computed with k-method, whereas the value obtained from pk-method was 290.8 (ft/s). In addition to the flutter speed calculated, pk-method also revealed that the divergence speed of the wing was 286.1 (ft/s), which is slightly lower than the flutter speed. Damping and frequency terms were plotted versus the corresponding airspeed of the vehicle. These plots are given in Figure 103-Figure 106.

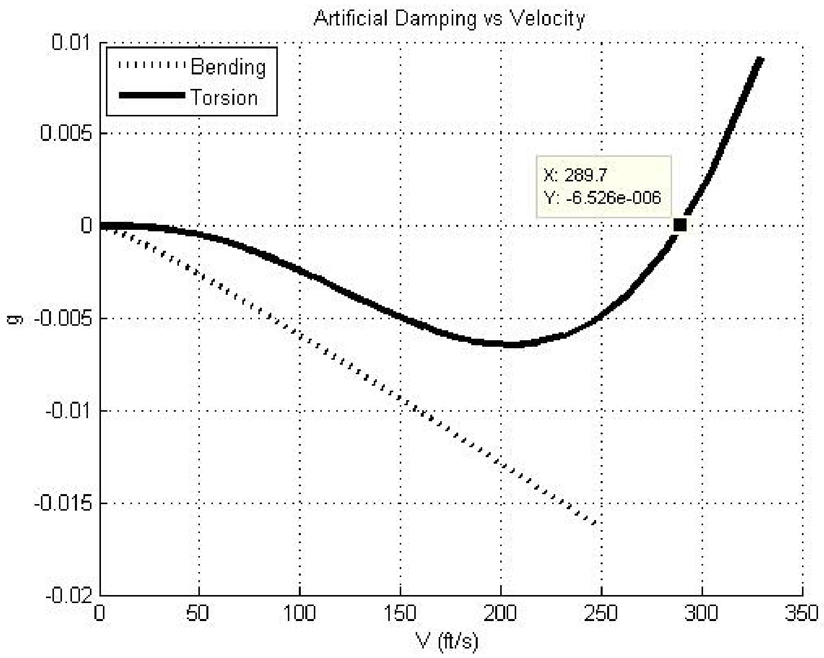

Figure 103: Damping vs. Velocity Plot of Modes of the Cruise Wing Configuration by using k-method in Two Degrees of Freedom

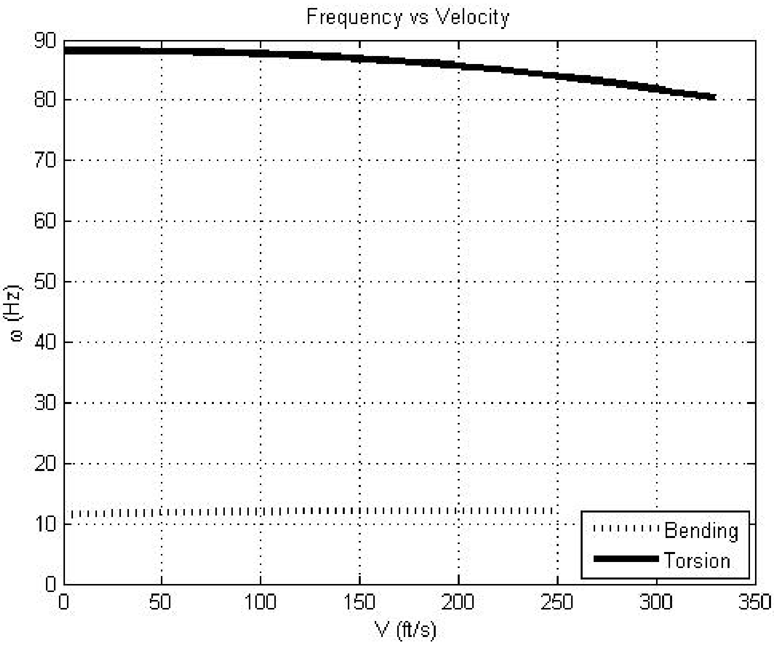

Figure 104: Frequency vs. Velocity Plot of Modes of the Cruise Wing Configuration by using k-method in Two-Degrees-of-Freedom

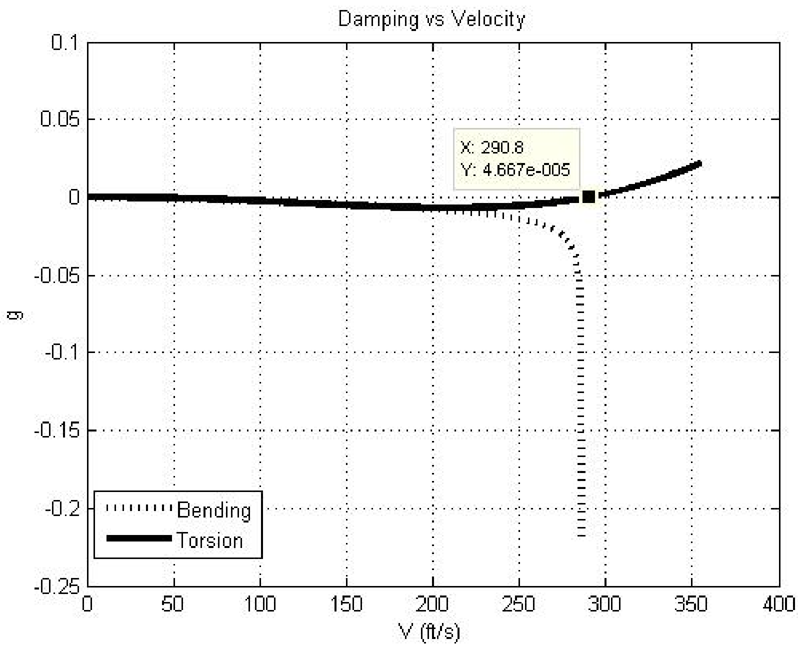

Figure 105: Damping vs. Velocity Plot of Modes of the Cruise Wing Configuration by using pk-method in Two-Degrees-of-Freedom

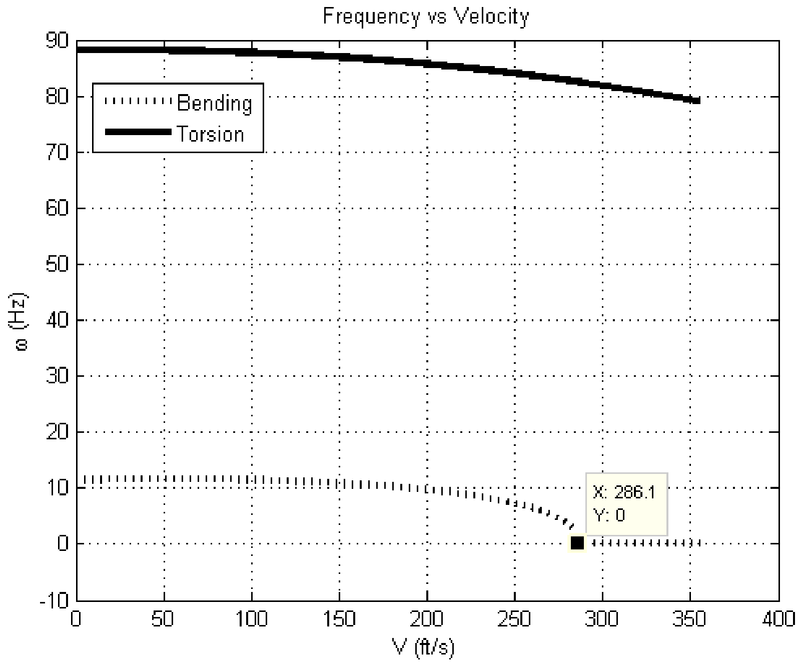

Figure 106: Frequency vs. Velocity Plot of Modes of the Cruise Wing Configuration by using pk-method in Two-Degrees-of-Freedom

8.2.1.4 Two-Degrees-of-Freedom Aeroelastic Analysis of the Morphing Wings for the Loiter Configuration

The last configuration on which the aeroelastic analyses conducted was the loiter configuration. Although the flutter speed was found as 184 (ft/s) by using k-method and 184.1 (ft/s) by pk-method, the divergence speed obtained from pk-method was 108.4 (ft/s). This was a result of the high aspect ratio used for the conceptual design of the morphing wings to increase the loitering performance. This was not a desired condition for an aircraft wing. Having the same amount of material and building a slender wing, it was inevitable to achieve such a result. This was actually the goal of this thesis, to give a perspective to the literature about some deficiencies of the fully morphing wings, which should be carefully treated. The results of the aeroelastic analyses conducted are given in Figure 107-Figure 110.

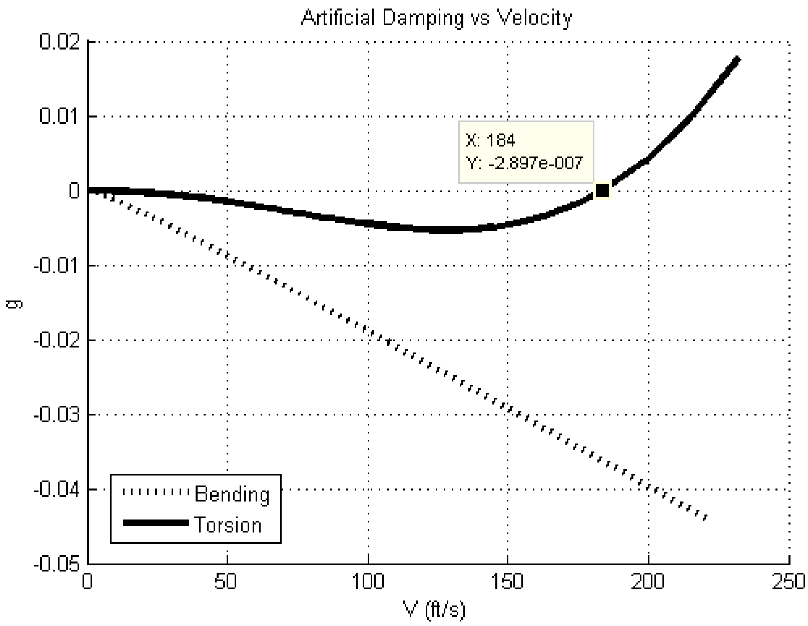

Figure 107: Damping vs. Velocity Plot of Modes of the Loiter Wing Configuration by using k-method in Two-Degrees-of-Freedom

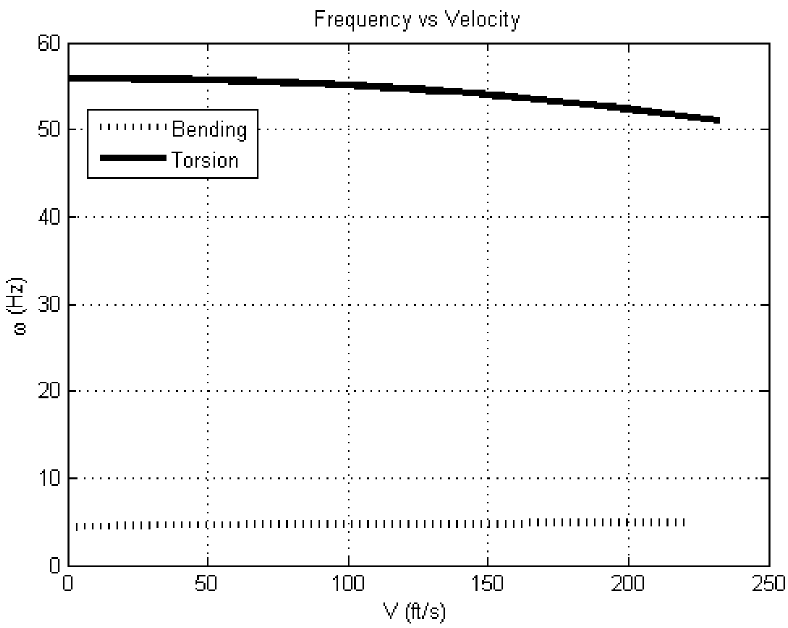

Figure 108: Frequency vs. Velocity Plot of Modes of the Loiter Wing Configuration by using k-method in Two-Degrees-of-Freedom

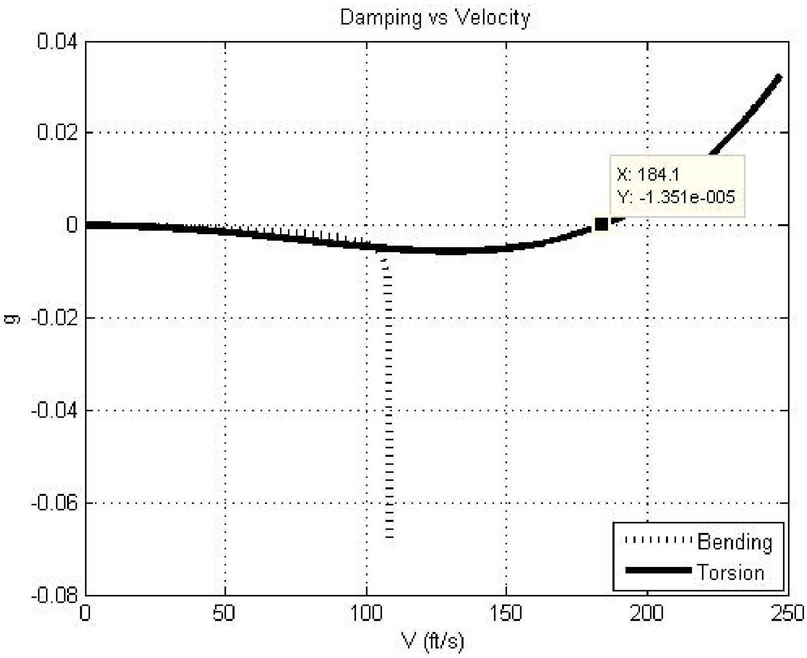

Figure 109: Damping vs. Velocity Plot of Modes of the Loiter Wing Configuration by using pk-method in Two-Degrees-of-Freedom

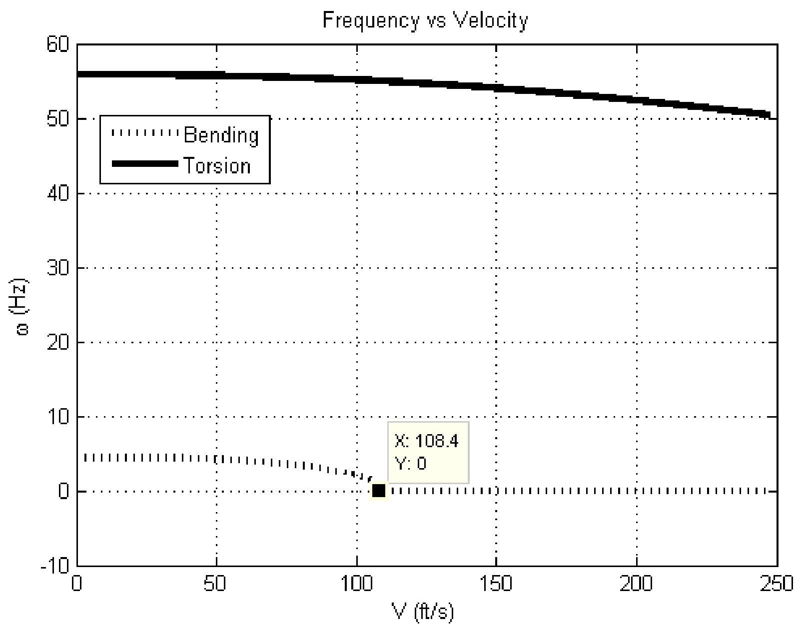

Figure 110: Frequency vs. Velocity Plot of Modes of the Loiter Wing Configuration by using pk-method in Two-Degrees-of-Freedom

8.2.1.5 Discussion on the Results of the Analyses Conducted on the Two-Degrees-of-Freedom Reduced Order Aeroelastic Model

The results obtained from the two-degrees-of-freedom reduced order aeroelastic model showed that divergence instability occurs at speeds lower than the flutter speed except at the climb condition. Flutter, or divergence speeds were compared with the maximum possible speed of the UAV at the specified configurations, calculated by using Equation 7.1.

$$V_{max} = \left\{ \frac{\left[T_{A,max}/W\right] W/S + (W/S)\sqrt{\left[T_{A,max}/W\right]^2 - 4C_{D,0}K}}{\rho_\infty C_{D,0}} \right\}^{\frac{1}{2}} \qquad 7.1$$

When Equation 7.1 was evaluated at sea level (to achieve the lowest value) for the wing loading of each configuration, the maximum velocities for each mission within the flight envelope were determined. These maximum speeds were compared to the divergence and flutter speeds obtained from the two-degrees-of-freedom aeroelastic model in Table 24.

Table 24: Comparison of the Flutter and Divergence Speeds Obtained from Two-Degrees-of-Freedom Reduced Order Model with Maximum Speed of the UAV

Mission Configuration	Maximum Speed	Predicted Divergence Speed	Predicted Flutter Speed
Take-off	211.95 (ft/s)	70.95 (ft/s)	122.30 (ft/s)
Climb	290.42 (ft/s)	257.90 (ft/s)	257.90 (ft/s)
Cruise	299.37 (ft/s)	286.10 (ft/s)	290.80 (ft/s)
Loiter	271.52 (ft/s)	108.40 (ft/s)	184.10 (ft/s)

As it can be understood from the comparison of the aeroelastic instabilities to the maximum velocities, all of them are achievable within the flight envelop. This proves how essential aeroelastic analyses were, for the design of wing structures. Furthermore, the drastic effect of morphing on the flutter and divergence speeds could be seen in Table 24. The high performance wing geometries for each phase of the flight were calculated based on the flight mechanics point of view in Section 3.3. Then, the structural design of the wings was conducted in Sections 4.3 and 4.4, by considering the smallest planform as the basis to achieve a lighter structure. This resulted in a less stiff structure in all other configurations. As the planform area and/ or the aspect ratio increased, the flutter and divergence speeds decreased drastically. If compared to the results of the cruise configuration, the divergence speed of the take-off configuration was calculated as 75.3 percent lower. Similarly, the flutter speed computed for the take-off configuration was 57.9 percent lower than the flutter speed achieved at the cruise configuration. Hence, it has been even more essential to conduct a series of aeroelastic analyses through the design of morphing wing structures.

8.2.2 Aeroelastic Analyses of the Morphing Wings by Using a Three-Degree-of-Freedom Model

Installment of ailerons on the wings was essential since the wings were not designed for gradual twist or camber change capability. It would be better to recall that, the morphing was achieved by the shape changes in terms of planform area, chord length, span and the sweep angle. Therefore, a set of ailerons were installed on the wings for employing maneuverability. The control surface was cut out from the trailing edge at the 90 percent chord location, where the folding skin concept described in Section 4.3 was not applied, in order not to affect the aerodynamics of the wing. It was assumed that the addition of the control surface did not affect the overall mass and stiffness of the wing. A typical frequency ratio of 10 was set between the control surface (C.S.) flapping and the plunge motion of the wings [11].

To illustrate, at loiter phase the plunge natural frequency was 4.4 (Hz), the C.S. flapping natural frequency should then be 44 (Hz).

The ratio between C.S. flapping and the plunge motion of the wings depended on the torsional stiffness of the hinge rod, which was used to rotate the aileron. The torsional stiffness of the rod should be high enough, not to be affected by the oscillatory motions of the wing at out-of plane bending modes. Since, the stiffness of the torsional rod rotating the aileron was considered at the conceptual design phase, the wing could be approximated as a cantilevered beam. The ratio of the first out-of-plane bending mode and the second out-of-plane bending mode for a uniform cantilevered beam in classical beam theory has been given approximately as 6.2 [29]. In order to achieve a safety margin of at least 50 percent the ratio of the torsional mode of the hinge rod should be at least 9.3. This was the reason why in literature the ratio of 10 was considered as to be a typical parameter. Here, it would be convenient to refer to the normal modes analyses conducted in Section 7.3. The ratio of the first out-of-plane bending mode and the second out-of-plane bending mode for the take-off, and loiter configurations, which could be approximated as uniform cantilevered beams since the chord length kept constant, were found as 5.51 and 6.02 respectively. Therefore, the analogy of using the formulas given for the uniform cantilevered beam as conceptual design constraints was appropriate. The wings at the climb and cruise were not included in the comparison since they are tapered and their behavior is slightly different.

In addition, the mass of the control surface was chosen to be 5 percent of the whole wing. This value was selected from the finite element models. The mass of the last 10 percent of the wing in chordwise direction was found as 5 percent of the total weight.

This case study was a generic study based on historical trends. The purpose of the study was to show the effects of an aileron on the flutter behavior of morphing wings. This aileron might also be a camber changing mechanism [1][2][3]; since the design criteria explained in the previous paragraph was fixed, the implementation of the model would not change. The results are given for each set of wing, designed for different mission, separately.

8.2.2.1 Three-Degrees-of-Freedom Aeroelastic Analysis for the Take-off Configuration of Morphing Wings

Aeroelastic analyses were conducted on the three-degrees-of-freedom reduced order model of the morphing wings. The same methods of solution were used for the analyses. At the take-off configuration, conducted analyses showed that the predicted flutter speed of the wings was 113.1 (ft/s) based on the both k-method and pk-method. As it was in the case of two-degrees-of-freedom model, pk-method predicted the divergence speed around 71.62 (ft/s), which was approximately the same as two-degrees-of-freedom case. However, it could be noticed that the flutter speed due to oscillations at the torsion mode decreased by 7.5 percent. This was a direct effect of the additional control surface. The control surface reduced the predicted flutter speed of the wing configuration at take-off. The plots of damping and frequency terms extracted from the eigenvalue problems are given in Figure 111 - Figure 114.

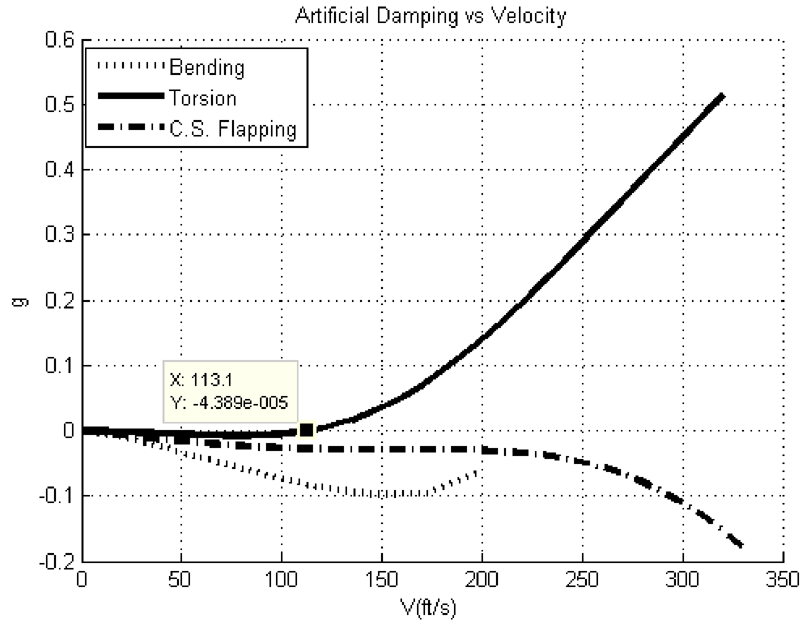

Figure 111: Damping vs. Velocity Plot of Modes of the Take-off Wing Configuration by using k-method in Three-Degrees-of-Freedom

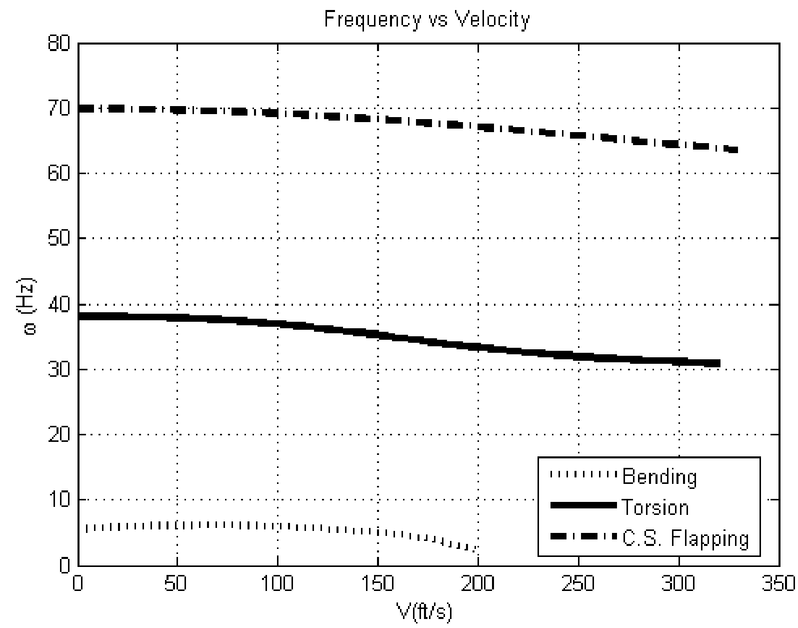

Figure 112: Frequency vs. Velocity Plot of Modes of the Take-off Wing Configuration by using k-method in Three-Degrees-of-Freedom

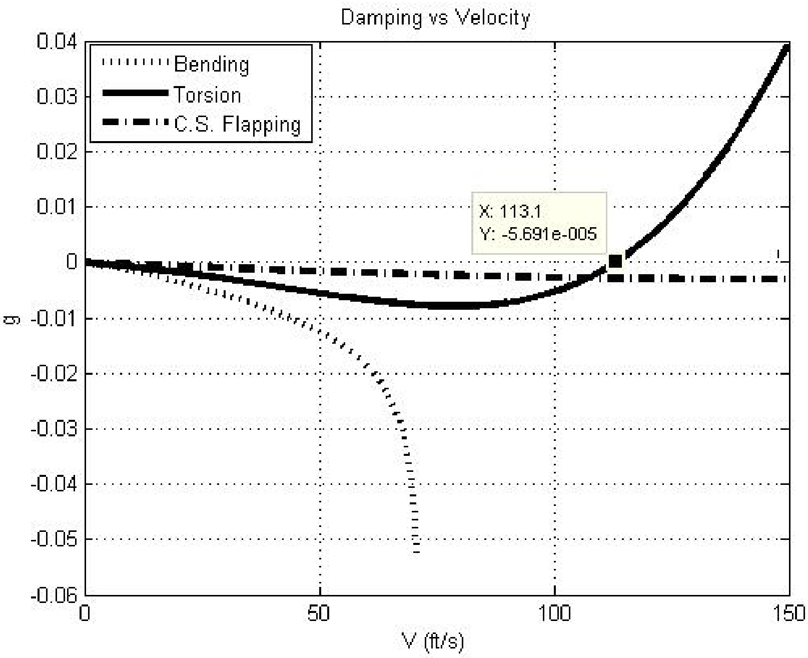

Figure 113: Damping vs. Velocity Plot of Modes of the Take-off Wing Configuration by using pk-method in Three-Degrees-of-Freedom

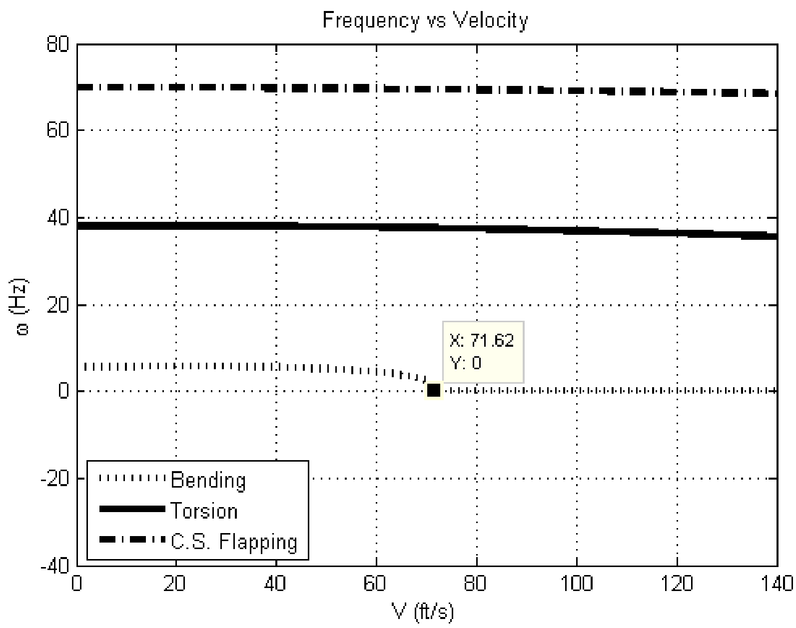

Figure 114: Frequency vs. Velocity Plot of Modes of the Take-off Wing Configuration by using pk-method in Three-Degrees-of-Freedom

8.2.2.2 Three-Degrees-of-Freedom Aeroelastic Analysis for the Climb Configuration of Morphing Wings

The same analyses were conducted on the climb wing configuration by using the three degrees of freedom reduced order model. A different behavior was experienced for the climb configuration. Since, the climb wing had a relatively low aspect ratio and a tapered planform, it was stiffer than the rectangular and/ or higher aspect ratio take-off and loiter configurations. This resulted in the occurrence of flutter in C.S. flapping mode. The C.S. flutter speed was found to be 190.1 (ft/s) by using k-method and 191.2 (ft/s) by using pk-method. The divergence speed, as being a static aeroelastic phenomenon, once again was not affected by the addition of a new degree of freedom to the system. It was computed as 257.5 (ft/s) by the in-house developed pk-method solver. The obtained results are given in plots of damping and frequency terms versus airspeed in Figure 115- Figure 118.

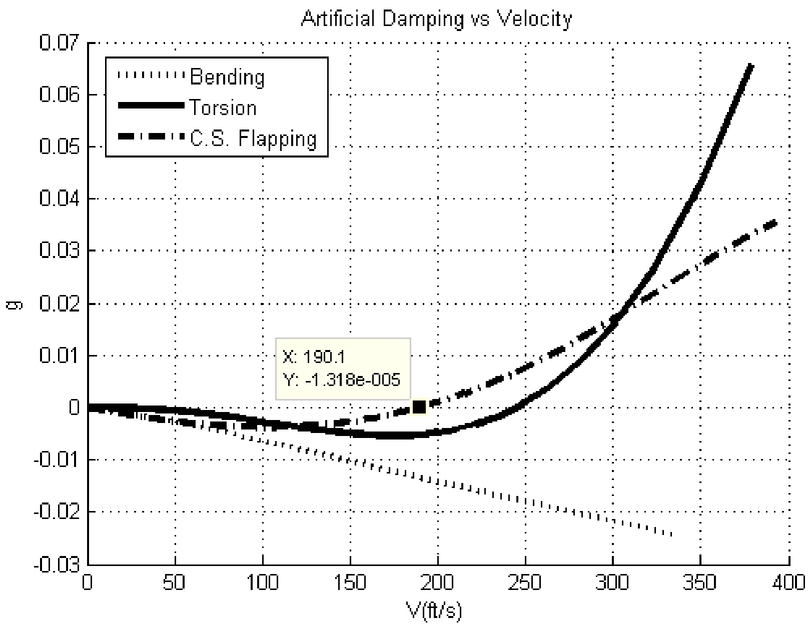

Figure 115: Damping vs. Velocity Plot of Modes of the Climb Wing Configuration by using k-method in Three-Degrees-of-Freedom

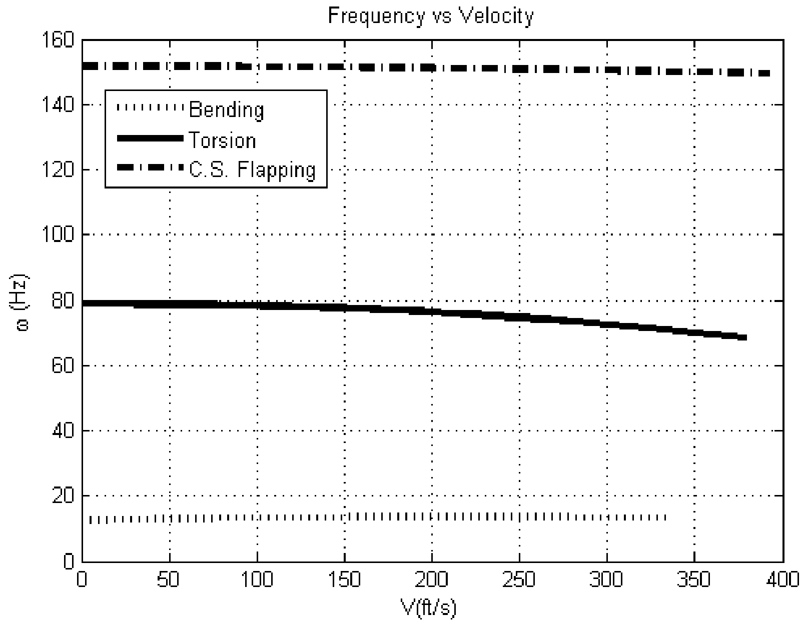

Figure 116: Frequency vs. Velocity Plot of Modes of the Climb Wing Configuration by using k-method in Three-Degrees-of-Freedom

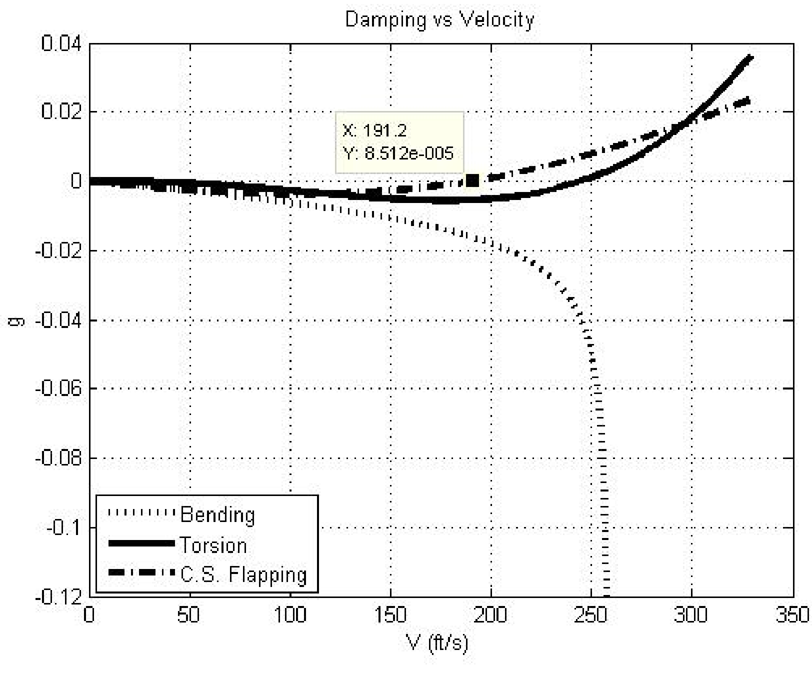

Figure 117: Damping vs. Velocity Plot of Modes of the Climb Wing Configuration by using pk-method in Three-Degrees-of-Freedom

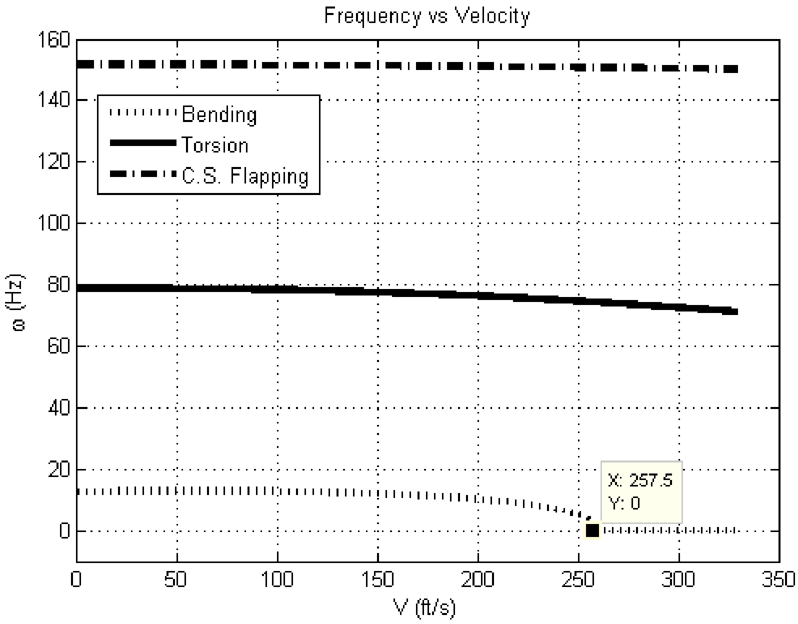

Figure 118: Frequency vs. Velocity Plot of Modes of the Climb Wing Configuration by using pk-method in Three-Degrees-of-Freedom

8.2.2.3 Three-Degrees-of-Freedom Aeroelastic Analysis for the Cruise Configuration of Morphing Wings

Aeroelastic analyses conducted on the three degrees of freedom model of the cruise wing configuration by using k-method and pk-method led to flutter speed results, 269.6 (ft/s) and 270.1 (ft/s) respectively. There was a 7.1 % decrement in the flutter speed due to the effect of the presence of a control surface on the structure. For the cruise configuration, divergence was predicted at 286.1 (ft/s). It was observed in the previous analyses that the divergence speed was not affected by the addition of a dynamic phenomenon into the system. These results could also be observed in pk-analysis conducted for the cruise configuration. The results obtained from the conducted analyses are given in Figure 119- Figure 122.

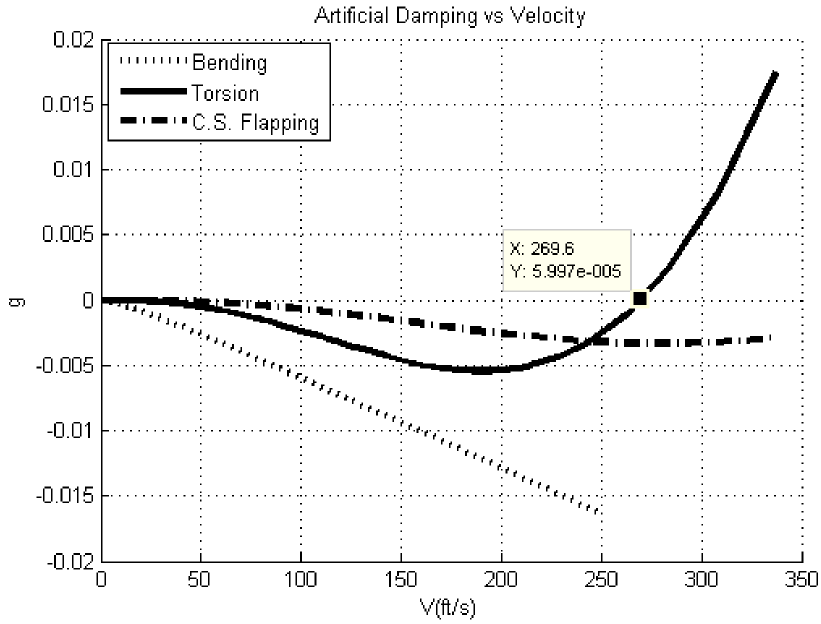

Figure 119: Damping vs. Velocity Plot of Modes of the Cruise Wing Configuration by using k-method in Three-Degrees-of-Freedom

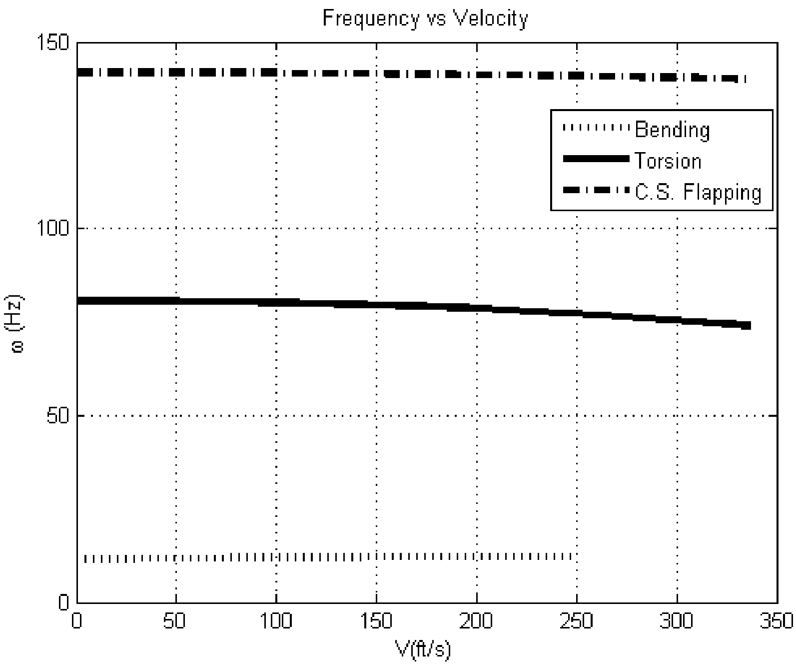

Figure 120: Frequency vs. Velocity Plot of Modes of the Cruise Wing Configuration by using k-method in Three-Degrees-of-Freedom

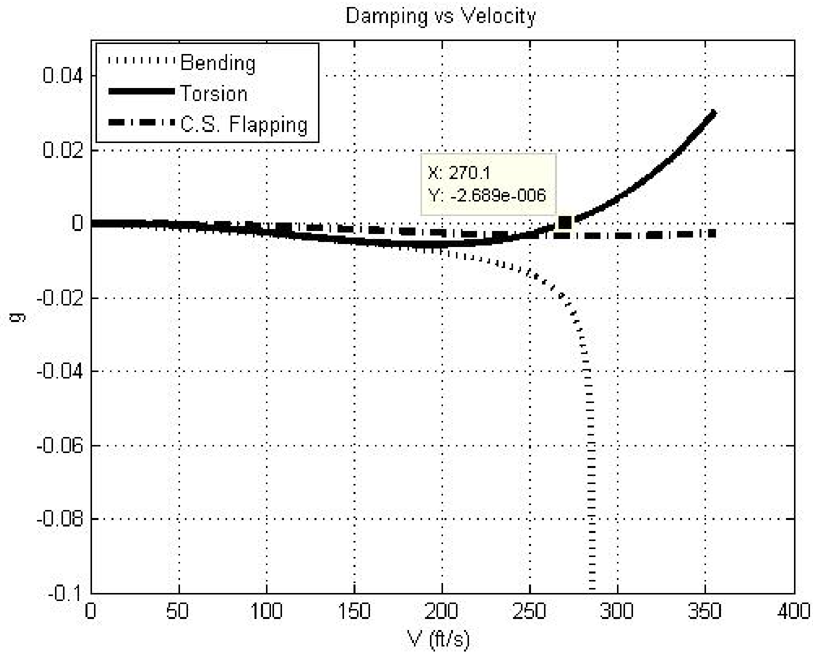

Figure 121: Damping vs. Velocity Plot of Modes of the Cruise Wing Configuration by using pk-method in Three-Degrees-of-Freedom

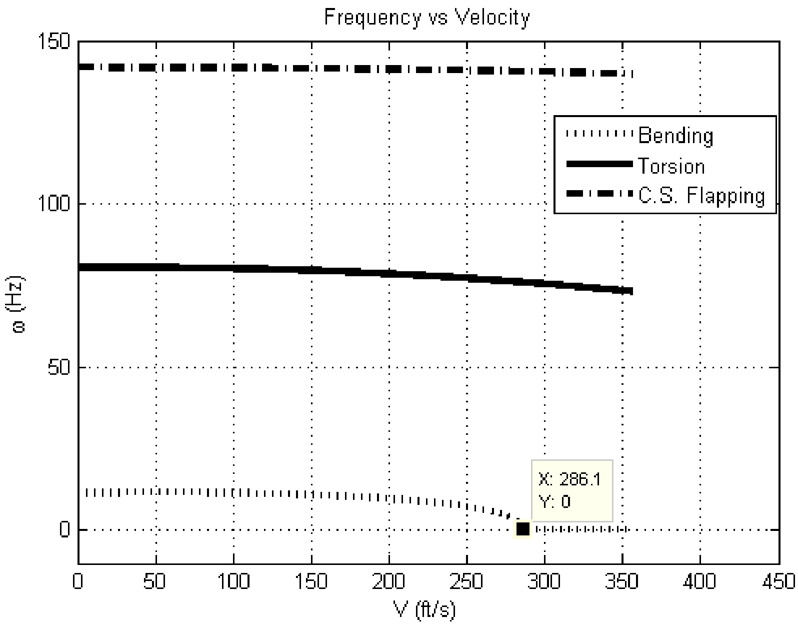

Figure 122: Frequency vs. Velocity Plot of Modes of the Cruise Wing Configuration by using pk-method in Three-Degrees-of-Freedom

8.2.2.4 Three-Degrees-of-Freedom Aeroelastic Analysis for the Loiter Configuration of Morphing Wings

Three degree of freedom reduced order model of the loiter configuration, when analyzed by using the in-house developed computer program with k-method and pk-method applications, gave flutter speed results as; 136.6 (ft/s) in k-method, 133.7 (ft/s) in pk-method. Unstable mode computed was torsional mode; however, before reaching that speed, at 108.2 ft/s, an aeroelastic divergence was predicted by the p-k algorithm. The results of analyses are given in Figure 123 - Figure 126.

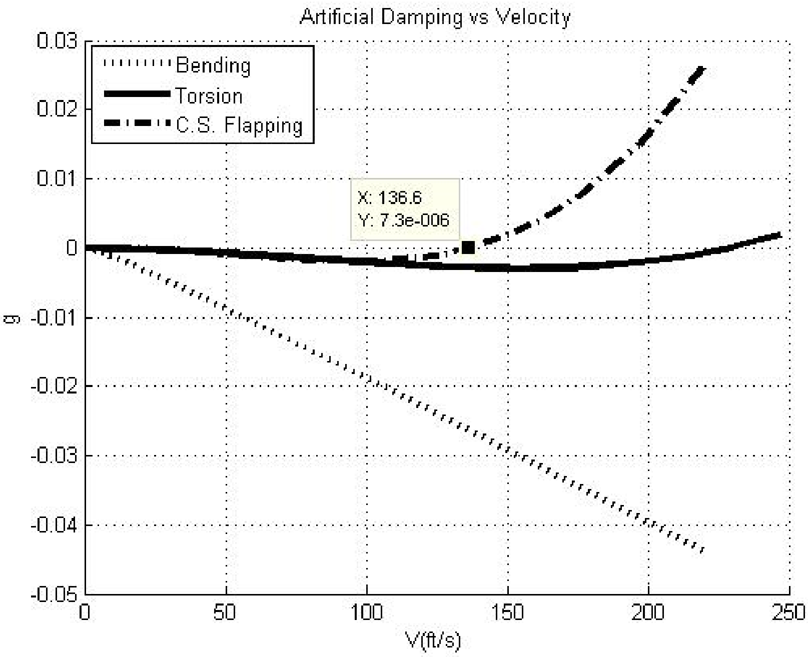

Figure 123: Damping vs. Velocity Plot of Modes of the Loiter Wing Configuration by using k-method in Three-Degrees-of-Freedom

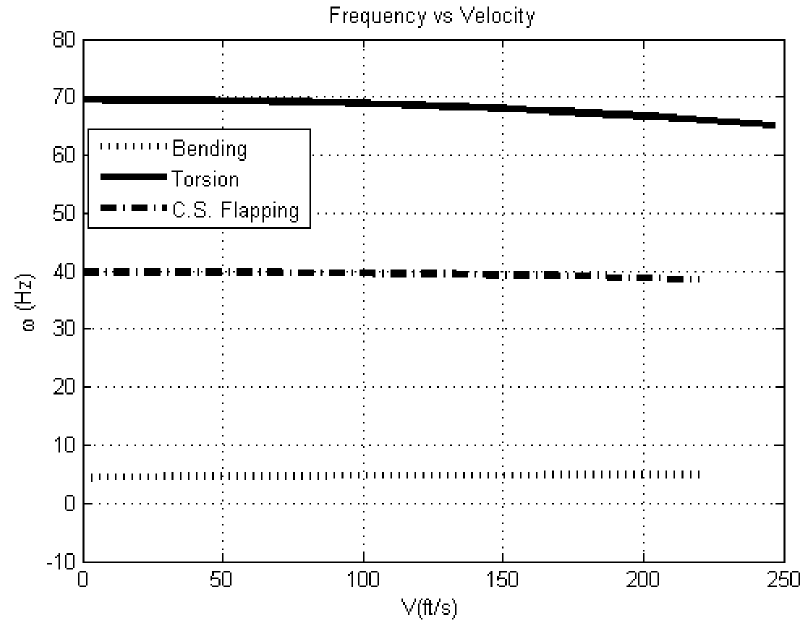

Figure 124: Frequency vs. Velocity Plot of Modes of the Loiter Wing Configuration by using k-method in Three-Degrees-of-Freedom

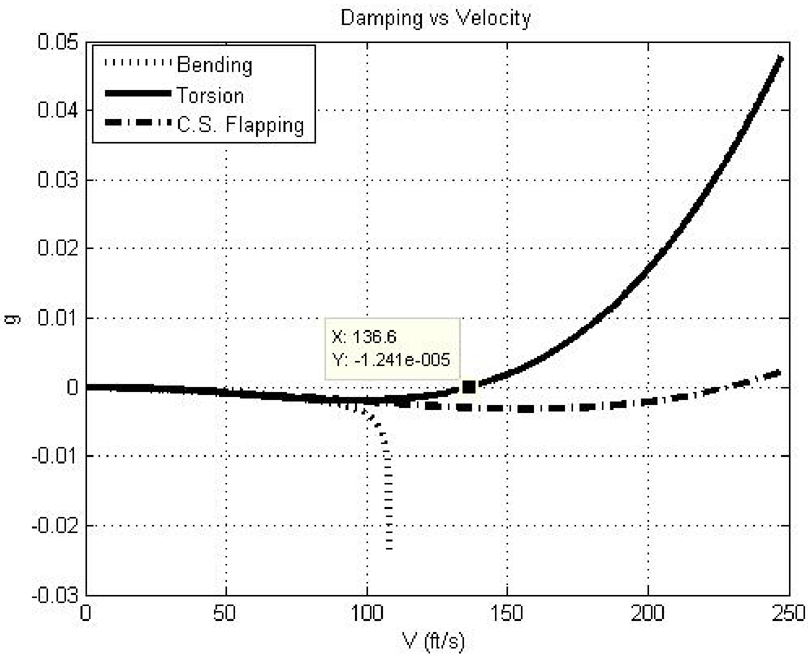

Figure 125: Damping vs. Velocity Plot of Modes of the Loiter Wing Configuration by using pk-method in Three-Degrees-of-Freedom

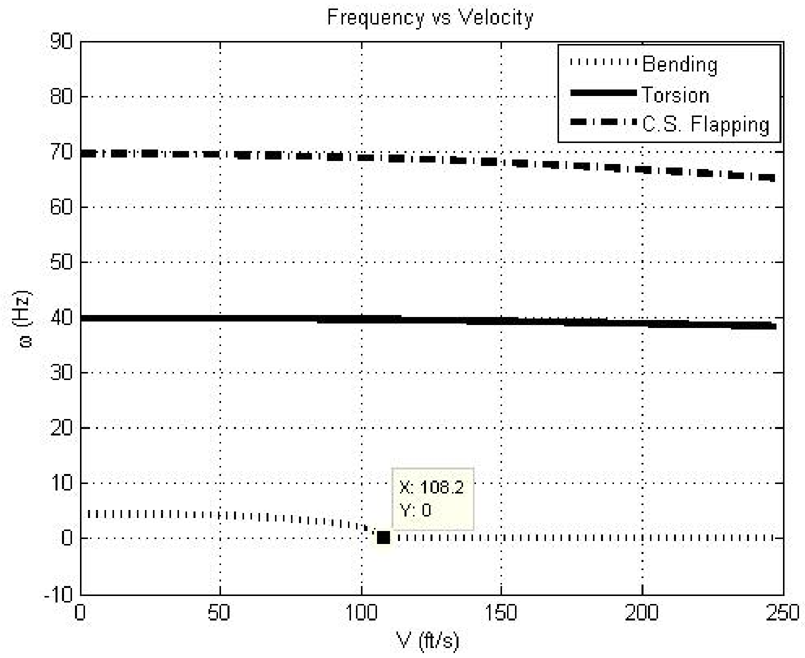

Figure 126: Frequency vs. Velocity Plot of Modes of the Loiter Wing Configuration by using pk-method in Three-Degrees-of-Freedom

8.2.2.5 Discussion on the Results of Three-Degrees-of-Freedom Reduced Order Aeroelastic Model

Three-degrees-of-freedom model was used to identify the effects of an additional dynamic phenomenon into the system, such as a set of ailerons. It was observed that the addition of control surfaces had two possible effects on the structure. Either, the flapping mode of the control surface became the unstable mode, or it decreased the flutter speed of other modes. In average around 7 % of flutter speed decrement was observed for the control surface installed. Therefore, it is essential to analyze any change of the structural configuration since it might lead to changes on the dynamic aeroelastic behavior. Static aeroelastic behavior was not affected since it was assumed that the overall stiffness and other structural parameters were constant after the employment of the control surface.

The predicted values of the flutter and the divergence speeds for the four different wing configurations are compared to the maximum achievable speeds within the flight regime in Table 25.

Table 25: Comparison of the Flutter and Divergence Speeds Obtained from Three-Degrees-of-Freedom Reduced Order Model with Maximum Speed of the UAV

Mission Configuration	Maximum Speed	Predicted Divergence Speed	Predicted Flutter Speed
Take-off	211.95 (ft/s)	70.62 (ft/s)	113.10 (ft/s)
Climb	290.42 (ft/s)	257.50 (ft/s)	197.20 (ft/s)
Cruise	299.37 (ft/s)	286.10 (ft/s)	286.10 (ft/s)
Loiter	271.52 (ft/s)	108.20 (ft/s)	136.60 (ft/s)

CHAPTER 9

CONCLUSION

Many different morphing concepts are present in the literature. These concepts have their advantages and disadvantages; however, all need formal multi-disciplinary optimization. Some were formally optimized in terms of aerodynamics or structural mechanics point of view; few were optimized in both disciplines. Even so, the optimization procedures applied was considered to be limited. The aeroelastic behavior of the wing structure was not taken into account properly during the conceptual and detailed design phases of the morphing wings.

This thesis study was devoted to the identification of the linear aeroelastic behavior of morphing structures at different flight regimes. The main purpose of the analyses conducted was to introduce the literature, how essential aeroelastic considerations are in the procedure of designing the morphing structures.

In the survey through literature, it was clearly observed that fully morphing designs were developed through aerodynamic and weight optimization; however, the results of this study showed that, aeroelastic tailoring of the structure to find an optimum design was inevitable. The results of the analyses showed that the flutter speed decreases with a percentage of 58 between the highest flutter speed achieved at the smallest wing planform area configuration of the cruise mission and the lowest flutter speed achieved at the largest planform area configuration of the take-off mission. Similarly, the divergence speed decreases 75 percent between the highest case and the lowest case referred to.

The effects of morphing control surfaces were also investigated within the scope of the thesis. A control surface was located at the 90 percent of the chord and the weight of the control surface was assumed as 5 percent of the overall weight of the wing structure. The results showed that the possible effects of the control surfaces installed were decrement in the flutter speed if the instable mode is other than the control surface rotation mode, or an instable mode shifting occurs from an instability in bending or torsion into an instability in control surface rotation degree of freedom. When the shifting is not present, a 7 percent decrement in the flutter speed was obtained. The change in flutter speed is more drastic if a mode shift is present such observed at the climb and loiter configurations. These two different effects showed that the aeroelastic tailoring of the morphing systems should have more than one constraint. Another outcome was about the static aeroelastic behavior of the structure. An installation of a control surface, if the overall weight of the structure remains the same, has no effect on the divergence speed of the aircraft. This outcome was an expected one; however, it shows the consistency of the developed program.

Although it was not the scope of the thesis, the manuscript involves to a great extent, a generic conceptual design of a fully morphing wing in terms of high performance at take-off, climb, cruise and loiter phases of the flight. The concept was not, by any means an optimized concept and the mission planform shapes were not optimized either. The introduced morphing concept was developed based on a couple of ideas present in the literature; however, it is unique in terms of the combination of systems involved in the structure. A skin folding concept with a hybrid skin structure was used to be able to increase the chord length without having a permanent deformation on the skin material. A combination of a polyamide and a high-strain shape-memory polymer was forming the skin structure. A paddling spar structure was introduced in order to change the sweep angle of the wings among the mission configurations. A telescopic rib mechanism increases the chord length with an ability of gradual motion. By the gradual motion, the taper of the wing was also changed. These ribs were located at the first half-span from the root of the wing. At the second half-span a telescopic span expansion mechanism was installed. These ribs are passive in terms of chordwise motion. They govern the spanwise change of the ribs in order to increase the span. By these fundamental mechanisms the planform area of the wings increase up to 100 percent among the missions. Through the analyses conducted within this thesis, it was assumed that the mechanism designed was capable of sustaining the necessary motion between mission configurations. In addition to these, it was believed that the suggested morphing wing design was producible with a prototyping system, such as selective laser sintering.

To summarize, this thesis work was intended to be a guide for the structural problems to be encountered during morphing design and to emphasize that, at any phase of the morphing aircraft design, aeroelastic behavior of the structure should be considered with great attention. Otherwise, the design should have a variation of flutter speeds, such as the model given in this thesis.

REFERENCES

[1] Seber, G., et. al (2009). Evaluation of a camber morphing concept based on controlled flexibility. *International Forum on Aeroelasticity and Structural Dynamics*, Seattle, USA

[2] Seber, G. et. al. (2009). Structural Modeling and Flutter Analysis of Adaptive Camber Wings. *5. Ankara International Aerospace Conference*, Ankara, Turkey

[3] Seber, G., & Sakarya, E. (2010). Nonlinear Modeling and Aeroelastic Analysis of an Adaptive camber Wing. *Journal of Aircraft*, 47(6), 2067-74.

[4] Gamboa, P., Vale, P., Lau, F. J. P., & Suleman, A. (2009). Optimization of a Morphing Wing Based on Coupled Aerodynamic and Structural Constraints. *AIAA Journal*, 47(9), 2087-104

[5] Amiryants. G., et. al. (2010). Selectively Deformable Structures for Design of Adaptive Wing Smart Elements as Part of Active Aeroelastic Wing Concept. *EASN Association Workshop*, Paris, France

[6] Dowell, E. H., et. al. (2004). *A Modern Course in Aeroelasticity.* Netherlands: Kluwer Academic Publishers

[7] Bisplinghoff, R. L., & Ashley, H. (2002). *Principles of Aeroelasticity.* USA: Dover Publications, Inc.

[8] Bisplinghoff, R. L., Ashley, H., & Halfman, R. L. (1996). *Aeroelasticity*. USA, Dover Publications, Inc.

[9] Hodges, D. H., & Pierce, G. A. (2002). *Introduction to Structural Dynamics and Aeroelasticity.* UK: Cambridge University Press

[10] Bryson, A. E. (1994). *Control of Spacecraft and Aircraft.* USA: Princeton University Press

[11] Seber, G., Ünlüsoy, L., & Sakarya, E. (2009). Flutter Characteristics of a Typical Section Model with a Trailing Edge Control Surface, *5. Ankara International Aerospace Conference*. Ankara, Turkey

[12] Rodden, W. P., Harder, R. L. & Bellinger, E.D. (1979). *Aeroelastic Addition to NASTRAN*. VA, USA: NASA Critical Report 3094

[13] Skillen, M. D. & Crossley, W. A. (2007). *Modeling and Optimization for Morphing Wing Concept Generation*. VA, USA: NASA/CR-2007-214860

[14] Wall, R. (2002, April 8). Darpa Eyes Materials for 'Morphing' Aircraft. *Aviation Week and Space Technology*. p.36.

[15] Anderson, J. D., Jr. (1999) .*Aircraft Performance and Design*. Singapore: McGraw-Hill Book Co.

[16] Lee, C. S., et. al. (2004). Classification of Airfoils by Abnormal Behavior of Lift Curves at Low Reynolds Number. *24th International Congress of the aeronautical Sciences*. Yokohama, Japan

[17] Pinkerton, R. M. (1937). *Calculated and Measured Pressure Distributions over the Midspan Section of the N. A. C. A. 4412 Airfoil*. VA, USA: NACA Report No. 563

[18] Raymer, D. P. (2004). *Aircraft Design: A Conceptual Approach.* Washington, D.C.: American Institute of Aeronautics and Astronautics, Inc.

[19] Plantenberg, K. (2009). *Introduction to CATIA V5*. Mission, KS, USA: SDC Publications

[20] Phillips, W. F. (2004). *Mechanics of Flight.* USA: Wiley & Sons Inc.

[21] Filippone, A. (2000). Data and Performances of Selected Aircraft and Rotorcraft, *Progress in Aerospace Sciences,* 36, 629-54

[22] Palmer, R. J. (2001). Polyamides, Plastics. *Encyclopedia of Polymer Science and Technology*

[23] EOS – e-Manufacturing Solutions. (2012, November 20). Retrieved from Material Data Center: http://eos.materialdatacenter.com/eo/material/pdf/datasheet/?mdc5=0djtrviqh7gdlja7o5pb1ejvs7

[24] EOS – e-Manufacturing Solutions. (2013, November 7). Retrieved from Material Data Center: http://eos.materialdatacenter.com/eo/material/pdf/datasheet/?mdc5=0djtrviqh7gdlja7o5pb1ejvs7

[25] Voit, W., et. al. (2010). High-strain Shape-memory Polymers. *Advanced Functional Materials Journal*, 20, 162-71

[26] Niu, C. Y. M. (1989). *Airframe Structural Design.* Hong Kong: Conmilit Press Ltd.

[27] eFunda (2013, December 15). Retrieved from The Ultimate Online Reference for Engineers: http://www.efunda.com/designstandards/beams/SquareIBeam .cfm

[28] Wikipedia (2009, February 22). Retrieved from Wikipedia Free Encyclopedia: http://upload.wikimedia.org/wikipedia/commons/a/a0/Inchworm_Motor.jpg

[29] Blevins, R. D. (1995). *Formulas for Natural Frequencies and Mode Shapes.* Malabar, FL: Krieger Publishing Company

[30] Theodorsen, T. (1935). *General Theory of Aerodynamic Instability and the Mechanism of Flutter.* NACA Report No.496

[31] Schrenk, O. (1940). *A Simple Approximation Method for Obtaining the Spanwise Lift Distribution*. NACA Report No. 948

[32] Anderson, J. D., Jr. (2001). *Fundamentals of Aerodynamics.* Singapore: McGraw-Hill Book Co.

[33] Ünlüsoy, L. (2010) *Structural Design and Analysis of the Mission Adaptive Wings of an Unmanned Aerial Vehicle* (Master's Thesis). Middle East Technical University, Ankara, Turkey

[34] Liu, Y. (2000). *Efficient Methods for Structural Analysis of Built-up Wings*. (Doctoral dissertation). Retrieved from http://scholar.lib.vt.edu/theses/available/etd-05152000-19270054/unrestricted/finaldissertation_yhliu.pdf

[35] Giles, G. L. (1995). Equivalent Plate Modeling for Conceptual Design of Aircraft Wing Structures. *1st AIAA Aircraft Engineering, Technology and Operations Congress*, Los Angeles, CA

[36] Yang, Y., Wu, Z., & Yang, C. (2012). Equivalent Plate Modeling for Complex Wing Configurations. *Procedia Engineering*, 31, 409-15

[37] Roth, S. (2009). Influence of Mesh Density on a Finite Element Model under Dynamic Loading. *3rd European Hyper-works Technology Conference*, Ludwigsburg, Germany

[38] van Zyl, L. H. & Maserumule, M. S. (2001). Unrestrained Aeroelastic Divergence and the p-k Flutter Equation. *Journal of Aircraft,* 38(3), 588-90

VITA

PERSONAL INFORMATION

Surname, Name	: Ünlüsoy, Levent
Nationality	: Turkish (T.C.)
Date and Place of Birth	: September 1983, Ankara
Phone	: +90 (532) 2086006
E-mail	: lunlusoy@ae.metu.edu.tr

EDUCATION

Degree	Institution	Year of Graduation
M.S.	METU Aerospace Engineering	2010
B.S.	METU Aerospace Engineering	2006
High School	Ankara Atatürk Anatolian High School	2001

ACADEMIC EXPERIENCE

Year	Place	Enrollment
2012-Present	UTAA Aeronautical Engineering Dept.	Lecturer
2008-2012	METU Aerospace Engineering Dept.	Grad. Res. Assist.

RESEARCH INTERESTS

Aeroelasticity, Structural Dynamics, Structural Design, Finite Element Analyses, Morphing Aerial Vehicles

FOREIGN LANGUAGES

Advanced English

INTERNATIONAL CONFERENCE

1. Unlusoy, L. & Yaman, Y. (2013). Flutter Characteristics of an Adaptive Wing Having Camber Change and Free Play Nonlinearity. *7th Ankara International Aerospace Conference*, Ankara, Turkey
2. Unlusoy, L. & Inci, H. (2013). Flutter Optimization of Biaxial Composite Plate in Terms of Fiber Orientation via Genetic Algorithm. *International Forum on Aeroelasticity and Structural Dynamics*. Bristol, UK
3. Unlusoy, L., Sahin, M. & Yaman, Y. (2012). Verification of a Finite Element Model of an Unmanned Aerial Vehicle Wing Torque Box via Experimental Modal Testing. *11th Biennial Conference On Engineering Systems Design And Analysis*, Nantes, France
4. Sahin, M., Sakarya, E., Unlusoy, L., Insuyu, E. T., Seber, G., Ozgen, S. & Yaman, Y. (2010). Design, Analysis and Experimental Modal Testing of a Mission Adaptive Wing of an Unmanned Aerial Vehicle. *International Unmanned Vehicle Workshop*. Istanbul, Turkey
5. Ozgen, S., Yaman, Y., Sahin, M., Seber, G., Korpe, S., Sakarya, E., Unlusoy, L., Insuyu, T., Bayram, G., Uludag, Y. & Yilmaz, A. (2010) Morphing Air Vehicle Concepts. *International Unmanned Vehicle Workshop*. Istanbul, Turkey
6. Seber, G., Unlusoy, L. & Sakarya, E. (2009). Flutter Characteristics of Typical Section Models with Control Surfaces. *5th Ankara International Aerospace Conference*. Ankara, Turkey

NATIONAL CONFERENCE

1. Ünlüsoy, L. & Yaman, Y. (2013). Boşta Hareket Doğrusalsızlığı Bulunan, Göreve Uyumlu Kontrol Yüzeylerinin Çırpma Yönünden İncelenmesi. *16. Ulusal Makina Teorisi Sempozyumu*. Erzurum, Türkiye
2. Körpe, D. S., Ünlüsoy, L., Şahin, M., Özgen, S. & Yaman, Y. (2012). Büyük Oranda Şekil Değiştirebilen Kanatların Ön Tasarım Sürecinde Aerodinamik ve Yapısal Analizlerinin Eşlenmesi. *IV. Ulusal Havacılık ve Uzay Konferansı*. İstanbul, Türkiye

3. Ünlüsoy, L., Körpe, D. S., Şahin, M., Özgen, S. & Yaman, Y. (2012). Büyük Oranda Şekil Değiştirebilen Kanatların Aerodinamik ve Yapısal Tasarımı. *6. Savunma Teknolojileri Kongresi*. Ankara, Türkiye
4. Ünlüsoy, L., Yaman Y., Şahin, M., Özgen, S., Seber, G., İnsuyu, E.T. & Sakarya, E. (2011). Göreve Uyumlu Kanatlara Sahip Bir İnsansız Hava Aracının Uçuş Testleri ve Yapısal Geliştirilmesi. *15. Ulusal Makina Teorisi Sempozyumu*. Niğde, Türkiye
5. Yaman, Y., Özgen, S., Şahin, M., Seber, G., Sakarya, E., İnsuyu, E. T. & Ünlüsoy, L. (2011). ODTÜ'de Yapılan İnsansız Hava Aracı Çalışmaları. *VI. Ulusal Uçak, Havacılık ve Uzay Mühendisliği Kurultayı*. Eskişehir, Türkiye
6. Şahin, M., İnsuyu, E. T., Sakarya, E., Ünlüsoy, L., Özgen, S., Seber, G. & Yaman, Y. (2010). Göreve Uyumlu Kanatları Olan Bir İnsansız Hava Aracı Gövdesinin Yapısal Tasarımı ve Analizi. *5. Savunma Teknolojileri Kongresi*, Ankara, Türkiye
7. Şahin, M., Ünlüsoy, L., İnsuyu, E. T., Sakarya, E., Seber, G., Özgen, S. & Yaman, Y. (2010). Göreve Uyumlu Bir İnsansız Hava Aracı Kanadının Yapısal Modellenmesi ve Deneysel Doğrulanması. *5. Savunma Teknolojileri Kongresi*, Ankara, Türkiye
8. Yaman, Y., Özgen, S., Şahin, M., Seber, G., Nalbantoğlu, V., Sakarya, E., İnsuyu, E. T. & Ünlüsoy, L. (2009). Göreve Uyumlu Kanatlara Sahip Bir İnsansız Hava Aracının Tasarımı. *14. Ulusal Makina Teorisi Sempozyumu*. Güzelyurt, KKTC
9. Yaman, Y., Özgen, S., Şahin, M., Seber, G., Nalbantoğlu, V., Sakarya, E., İnsuyu, E. T., Ünlüsoy, L., Bayram, G., Uludağ, Y. & Yılmaz, A. (2009). ODTÜ'de Sürdürülen İnsansız Hava Aracı Çalışmaları. *V. Ulusal Uçak, Havacılık ve Uzay Mühendisliği Kurultayı*. Eskişehir, Türkiye
10. Çevik, M., Ezertaş, A., Gürsoy, E., Koçer, G., Selvi, S., İnsuyu, T., Yalçın, E., Ünlüsoy, L., Uzol, O. & Akmandor, S. (2006) İki Kişilik Türbin Motorlu Bir Eğitim Helikopterinin Konsept Tasarımı 2. Kısım: Verticool 111 Motoru ve Transmisyon Sistemi. Ankara, Türkiye